

# Control of Spacecraft in Proximity Orbits

by

Louis Scott Breger

Bachelor of Science Aeronautics and Astronautics  
Massachusetts Institute of Technology, 2002

Master of Science Aeronautics and Astronautics  
Massachusetts Institute of Technology, 2004

Submitted to the Department of Aeronautics and Astronautics  
in partial fulfillment of the requirements for the degree of

Doctor of Philosophy

at the

MASSACHUSETTS INSTITUTE OF TECHNOLOGY

June 2007

© Louis Scott Breger, MMVII. All rights reserved.

The author hereby grants to MIT permission to reproduce and  
distribute publicly paper and electronic copies of this thesis document  
in whole or in part.

Author .....

Department of Aeronautics and Astronautics

June 8, 2007

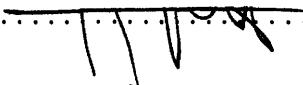
Certified by .....

Jonathan P. How

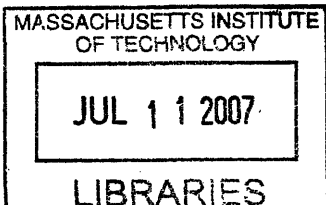
Associate Professor of Aeronautics and Astronautics

Thesis Supervisor

Accepted by .....

  
Jaime Peraire

Professor of Aeronautics and Astronautics  
Chair, Committee on Graduate Students



**ARCHIVES**



# Control of Spacecraft in Proximity Orbits

by

Louis Scott Breger

Author .....

Department of Aeronautics and Astronautics

June 8, 2007

Accepted by .....

Jonathan How

Associate Professor of Aeronautics and Astronautics

Thesis Supervisor

Accepted by .....

Kyle T. Alfriend

Professor of Aerospace Engineering, Texas A&M

Accepted by .....

John Deyst

Associate Professor of Aeronautics and Astronautics

Accepted by .....

Raymond Sedwick

Principal Research Scientist, Aeronautics and Astronautics



# Control of Spacecraft in Proximity Orbits

by

Louis Scott Breger

Submitted to the Department of Aeronautics and Astronautics  
on June 8, 2007, in partial fulfillment of the  
requirements for the degree of  
Doctor of Philosophy

## Abstract

Formation flying of spacecraft and autonomous rendezvous and docking of spacecraft are two missions in which satellites operate in close proximity and their relative trajectories are critically important. Both classes of missions rely on accurate dynamics models for fuel minimization and observance of strict constraints for preventing collisions and achieving mission objectives. This thesis presents improvements to spacecraft dynamics modeling, orbit initialization procedures, and failsafe trajectory design that improve the feasibility and chances of success for future proximity operations. This includes the derivation of a new set of relative linearized orbital dynamics incorporating the effects of Earth's oblateness. These dynamics are embedded in a model predictive controller, enabling LP-based MPC formulations for large baseline formations in highly elliptic orbits. An initialization algorithm is developed that uses the new dynamics to optimize multiple objectives (drift and fuel usage minimization, geometry) over science-relevant time frames, improving previous  $J_2$ -invariant initialization techniques which only considered infinite-horizon secular drift. The trajectory planning algorithm is used to design spacecraft rendezvous paths that observe realistic constraints on thruster usage and approach path. The paths are fuel-optimized and further constrained to be safe (i.e., avoid collisions) in the presence of many possible system failures, an enhancement over previous guaranteed-safe rendezvous methods, which did not minimize fuel use. The fuel costs of imposing safety as a constraint on trajectory design are determined to be low compared to standard approaches and a stochastic analysis demonstrates that both active and passive forms of the safe rendezvous algorithm substantially decrease the likelihood of system failures resulting in collisions. The effectiveness of the new controller/dynamics combination is demonstrated in high fidelity multi-week simulations. An optimized safe rendezvous trajectory was demonstrated on a hardware testbed aboard the International Space Station.

Thesis Supervisor: Jonathan P. How

Title: Associate Professor of Aeronautics and Astronautics



## Acknowledgments

I would like to thank everyone who has assisted me in my academic career. My parents and sister have supported me in every way and taught me the most important principles of graduate work long before my arrival at MIT. A complete list of everyone who's had a hand in this thesis would include my teachers through MIT, high school, and even earlier. I've been fortunate to have had access to an exceptional education and many good people to steer me along the way. In particular, I'd like to thank my first control systems instructors: Winston Markey, John Deyst, and Emilio Frazzoli. The semester-long introductory class they taught in automatic control in the Fall of 2000 changed the course of my life and I am grateful for having had the opportunity to study under them. Likewise, Lorraine Fesq helped me immeasurably in my quest to enter graduate school and find work afterward by providing me with many of my most treasured job experiences. Terry Alfriend's generous donations of time, expertise, and renowned intuition have enabled much of this research. The SPHERES team (in particular, Simon Nolet, Nick Hoff, and Chris Mandy) deserve many thanks for the time and effort they put into helping me get experiments working on their hardware and on ISS. My fellow labmates (notably Yoshiaki Kuwata, Arthur Richards, and Luca Bertuccelli) have always been around to bounce ideas off, study with, and even fly airplanes alongside; their companionship will be greatly missed. Kathryn Fischer's help navigating the administrative side of MIT has been indispensable. Finally, Jonathan How, who has been my graduate and research advisor for the past five years, has taught me far *far* more than I ever thought I had to learn. Jon's patience, wisdom, funding, and humor were necessary conditions for producing the contributions that follow.

*This thesis is dedicated to my parents, for whom the term acknowledgement seems inadequate. Their encouragement and example are my principal inspirations.*





# Contents

<b>Abstract</b>	<b>5</b>
<b>Acknowledgements</b>	<b>7</b>
<b>Table of Contents</b>	<b>8</b>
<b>List of Figures</b>	<b>12</b>
<b>List of Tables</b>	<b>19</b>
<b>1 Introduction</b>	<b>21</b>
1.1 Background . . . . .	23
1.1.1 Formation Flying Control Systems . . . . .	23
1.1.2 Linearized Relative Orbital Dynamics . . . . .	24
1.1.3 Formation Flying Initial Conditions . . . . .	25
1.1.4 Safety in Autonomous Rendezvous and Docking . . . . .	26
1.2 Thesis Overview . . . . .	27
<b>2 GVE-based Dynamics and Control for MPC</b>	<b>31</b>
2.1 Background . . . . .	32
2.2 Relative Orbital Elements and Linearization Validity . . . . .	34
2.3 $J_2$ -Modified GVEs and Linearization Validity . . . . .	41
2.3.1 Extension to Discrete Time . . . . .	45
2.3.2 Validity of the Linearization Approximations . . . . .	46
2.3.3 Calculating the $\Gamma$ matrix . . . . .	46

2.4	Model Predictive Control Using GVEs . . . . .	50
2.4.1	Error-Box Constraints Using Relative Orbital Elements . . . . .	53
2.4.2	Formation Flying: Coordination Using GVEs . . . . .	55
2.5	Comparison to Other GVE-based Impulsive Control Schemes . . . . .	58
2.6	Formation Maintenance on MMS-like Mission . . . . .	60
2.7	Summary . . . . .	62
<b>3</b>	<b>Fuel-optimized Semi-<math>J_2</math>-invariant Initial Conditions</b>	<b>65</b>
3.1	Formulation . . . . .	66
3.2	Results . . . . .	69
3.3	Summary . . . . .	75
<b>4</b>	<b>Formation Flying Simulations</b>	<b>77</b>
4.1	Introduction . . . . .	77
4.2	Mission Description . . . . .	77
4.3	Simulation Controller Configuration . . . . .	79
4.3.1	Parameters Examined . . . . .	80
4.4	Simulation Results . . . . .	82
4.5	Summary . . . . .	86
<b>5</b>	<b>Safe Trajectories for Autonomous Rendezvous of Spacecraft</b>	<b>105</b>
5.1	Introduction . . . . .	105
5.2	Online Trajectory Optimization for Autonomous Rendezvous and Docking . . . . .	107
5.3	Safety Formulation . . . . .	110
5.4	Scenarios . . . . .	112
5.4.1	Case 1: Stationary Target Satellite . . . . .	114
5.4.2	Case 2: Docking Port Perpendicular to Spin Axis . . . . .	118
5.5	Probability of Collision . . . . .	119
5.6	Invariant Formulation . . . . .	123

5.7	Convex Safety Formulation . . . . .	127
5.8	Active Safety . . . . .	131
5.8.1	Examples . . . . .	134
5.8.2	Active Safety for Thruster Failures . . . . .	137
5.8.3	Mitigating Impact of Process Noise and Navigation Error . . . . .	141
5.9	Summary . . . . .	143
<b>6</b>	<b>Safe Docking Demonstrations on SPHERES</b>	<b>145</b>
6.1	SPHERES Background . . . . .	145
6.2	Safe Autonomous Rendezvous and Docking on the SPHERES Testbed	146
6.3	Flight Experiment Results . . . . .	151
6.4	Flat Table Experiment Results . . . . .	157
6.5	Summary . . . . .	157
<b>7</b>	<b>Conclusions and Future Work</b>	<b>161</b>
7.1	Conclusions . . . . .	161
7.1.1	Linearized Relative Dynamics . . . . .	161
7.1.2	Optimized Initialization of Semi-Invariant Orbits . . . . .	162
7.1.3	Control of Spacecraft Formations Using MPC . . . . .	162
7.1.4	Safety in Autonomous Rendezvous and Docking . . . . .	163
7.1.5	Safe Autonomous Rendezvous Demonstration on Orbit . . . . .	164
7.2	Future Extensions . . . . .	164
	<b>Bibliography</b>	<b>175</b>



# List of Figures

2-1	Effect of Orbital Element Perturbations on the $\Delta B_{\text{true}}$ Matrix for a LEO Orbit . . . . .	40
2-2	Effect of Orbital Element Perturbations on the $\Delta B_{\text{true}}$ Matrix for a HEO Orbit . . . . .	40
2-3	Difference between integrated and approximated $\Gamma$ for different discretization times using the LEO orbit in Eq. (2.14) . . . . .	49
2-4	Difference between integrated and approximated $\Gamma$ for different discretization times using the HEO orbit in Eq. (2.16). . . . .	50
2-5	Example of a plan generated to MPC with $J_2$ -modified GVEs (lines indicate relative state error) . . . . .	52
2-6	Error in open-loop trajectory following using the HEO orbit example. Lines indicate the difference between planned and implemented trajectories in a fully nonlinear simulation. . . . .	54
2-7	Forming and maintaining a 1000 km (at apogee) tetrahedron formation in a highly eccentric orbit ( $e \approx 0.8$ ) in the presence of $J_2$ . . . . .	62
2-8	Forming and maintaining a 1000 km (at apogee) tetrahedron formation in a highly eccentric orbit ( $e \approx 0.8$ ) in the presence of $J_2$ . . . . .	63
3-1	Illustration of Initialization Approach . . . . .	68
3-2	Expected drift and fuel cost of a range of optimized initial conditions in a LEO orbit . . . . .	69
3-3	Expected drift and geometry cost of a range of optimized initial conditions in a LEO orbit. . . . .	70

3-4	Expected drift due to differential $J_2$ effects and fuel cost of a range of optimized initial conditions in a HEO orbit. . . . .	73
3-5	Expected drift due to differential $J_2$ effects and geometry cost of a range of optimized initial conditions in a HEO orbit. . . . .	73
3-6	Relative satellite separations for a vehicle initialized using analytic invariance and a vehicle using optimized invariance. Trajectories generated using realistic nonlinear simulation including the effects $J_2$ . . . . .	74
3-7	Relative satellite separations for a vehicle initialized using analytic invariance and a vehicle using optimized invariance. Trajectories generated using a nonlinear simulation that did <b>not</b> incorporate the effects $J_2$ . . . . .	74
4-1	Concept for MELCO formation flying mission [113] . . . . .	78
4-2	Summary of Station-keeping Results from Table 4.1 . . . . .	84
4-3	Simulation #1: Stationkeeping in a passive aperture formation (50 m)	87
4-4	Simulation #1: Stationkeeping in a passive aperture formation (500 m) . . . . .	88
4-5	Simulation #1: Stationkeeping in a passive aperture formation (5000 m) . . . . .	89
4-6	Simulation #2: Stationkeeping in a passive aperture formation (50 m)	90
4-7	Simulation #2: Stationkeeping in a passive aperture formation (500 m) . . . . .	91
4-8	Simulation #2: Stationkeeping in a passive aperture formation (5000 m) . . . . .	92
4-9	Simulation #3: Stationkeeping in a passive aperture formation (50 m)	93
4-10	Simulation #3: Stationkeeping in a passive aperture formation (500 m) . . . . .	94
4-11	Simulation #3: Stationkeeping in a passive aperture formation (5000 m) . . . . .	95
4-12	Simulation #4: Stationkeeping in a passive aperture formation (50 m)	96

4-13	Simulation #4: Stationkeeping in a passive aperture formation (500 m) . . . . .	97
4-14	Simulation #4: Stationkeeping in a passive aperture formation (5000 m) . . . . .	98
4-15	Simulation #5: Stationkeeping in a passive aperture formation (50 m)	99
4-16	Simulation #5: Stationkeeping in a passive aperture formation (500 m) . . . . .	100
4-17	Simulation #5: Stationkeeping in a passive aperture formation (5000 m) . . . . .	101
4-18	Simulation #6: Stationkeeping in a passive aperture formation (50 m)	102
4-19	Simulation #6: Stationkeeping in a passive aperture formation (500 m) . . . . .	103
4-20	Simulation #6: Stationkeeping in a passive aperture formation (5000 m) . . . . .	104
5-1	Target spacecraft and docking configuration . . . . .	115
5-2	Radial/in-track view of rotating target spacecraft and docking configuration . . . . .	115
5-3	Nominal trajectory planning with no safety: constraint violations occur for trajectory failures. . . . .	116
5-4	Trajectory planning with safety: failed trajectories deviate around the target spacecraft, preventing collision. . . . .	116
5-5	Nominal trajectory planning with no safety in the rotating case: constraint violations occur for trajectory failures. . . . .	120
5-6	Trajectory planning with safety in the rotating case: failed trajectories deviate around the target spacecraft, preventing collision . . . . .	120
5-7	Trajectory planning with safety in the fast rotating (3/2 orbital speed) case. . . . .	121
5-8	Probability of a collision occurring for a range of initial conditions with $\mathcal{F} = \emptyset$ (No safety guarantees). . . . .	124

5-9	Probability of a collision occurring for a range of initial conditions with $\mathcal{F} = \{9, \dots, 19\}$ (latter half of trajectory guaranteed safe) . . .	124
5-10	Probability of collision occurring for various values of $\mathcal{F}$ . . . . .	125
5-11	Fuel required for rendezvous maneuvers for various values of $\mathcal{F}$ . . .	126
5-12	Amount of time required to optimize rendezvous trajectories for various values of $\mathcal{F}$ . . . . .	127
5-13	Case where end of safety horizon is followed by a collision. . . . .	128
5-14	Use of invariance constraints guarantees infinite horizon passive collision avoidance and prevents failure trajectories from drifting away from the target. . . . .	128
5-15	Collision avoidance for failure trajectories using convex constraints indicated by arrows. . . . .	130
5-16	Active safety demonstrated for a range of initial conditions with $\mathcal{F} = \{4, \dots, 19\}$ (latter 3/4 of trajectory guaranteed safe) . . . . .	135
5-17	Rendezvous trajectories using active safety. . . . .	139
5-18	Rendezvous trajectories using active safety with invariance constraints. 140	
5-19	Rendezvous trajectories using optimized active safety. . . . .	140
5-20	Rendezvous trajectories using optimized active safety with invariance constraints. . . . .	142
5-21	Rendezvous trajectories for using active safety optimized for two possible thruster failure directions. . . . .	142
5-22	Safe rendezvous trajectory with robustness to initial condition velocity uncertainty . . . . .	143
6-1	SPHERES Microsatellite in air carriage on flat table testbed . . . . .	146
6-2	Planned safe trajectory for stationary rendezvous: $x$ - $y$ view. Note that trajectory $z$ offset is zero at all times . . . . .	149
6-3	SPHERES Microsatellite in air carriage on flat table testbed: Perspective view . . . . .	149



6-4	Planned safe trajectory for rotating rendezvous: $x$ - $y$ view. Note that trajectory $z$ offset is zero at all times . . . . .	150
6-5	Planned safe trajectory for rotating rendezvous: testbed: Perspective view . . . . .	150
6-6	SPHERES satellites docked together aboard the International Space Station using a safe optimized rendezvous trajectory. . . . .	152
6-7	Position trajectory followed during nominal docking ISS experiment: $x$ - $y$ view . . . . .	153
6-8	Position time-series for $z$ axis during nominal docking ISS experiment	153
6-9	Velocity time-series view during nominal docking ISS experiment . .	154
6-10	Velocity trajectory followed during nominal docking ISS experiment: $x$ - $y$ view . . . . .	154
6-11	Position trajectory followed during failed docking ISS experiment: $x$ - $y$ view . . . . .	155
6-12	Position time-series for $z$ axis during failed docking ISS experiment	155
6-13	Velocity time-series view during failed docking ISS experiment . . .	156
6-14	Velocity trajectory followed during failed docking ISS experiment: $x$ - $y$ view . . . . .	156
6-15	Position trajectory followed during failed docking flat table experiment: $x$ - $y$ view . . . . .	158
6-16	Position time-series for $z$ axis during failed docking flat table experiment . . . . .	158
6-17	Velocity time-series view during failed docking flat table experiment	159
6-18	Velocity trajectory followed during failed docking flat table experiment: $x$ - $y$ view . . . . .	159
7-1	Fuel Required to Maintain an In-track Formation . . . . .	169
7-2	Fuel Required to Maintain a Passive Aperture Formation . . . . .	169
7-3	Maneuver costs: plans created accounting for eccentricity and $J_2$ effects . . . . .	171

7-4	Maneuver costs: plans created accounting for eccentricity with no $J_2$ effects modeled . . . . .	172
7-5	Maneuver costs: plans created accounting for eccentricity with no $J_2$ effects modeled . . . . .	173
7-6	Maneuver costs: plans created not accounting for eccentricity with no $J_2$ effects modeled . . . . .	174

# List of Tables

1.1	Relative orbital dynamics indexed by regime of validity [115] . . . .	25
2.1	Average durations (in seconds) required to compute $\Gamma$ matrices using various methods . . . . .	51
4.1	Fuel use results for formation flying simulations . . . . .	83
5.1	Comparison of various types of safe rendezvous trajectories. . . . .	136
7.1	Table of maneuvers planned using combinations of $J_2$ and eccentricity	170



# Chapter 1

## Introduction

Many future space missions will require autonomous proximity operations in which the knowledge and control of the relative state between space vehicles is critically important [1, 54]. For example, formation flying satellites operating in close proximity to accomplish coupled goals will require high levels of on-orbit autonomy and coordinated control [65]. Rendezvous and docking missions are also inherently concerned with controlling the reduction of the distance between spacecraft. Both types of spacecraft proximity missions share common characteristics and control requirements that include: similar proposed sensing technologies [1] (CDGPS, inter-satellite ranging), critical dependence on fuel minimization to ensure mission feasibility [84], the need to prevent relative drift between vehicles [73], use of relative orbital dynamics for the control design [65], concerns of collision avoidance between vehicles [61], and complicated multi-vehicle safe mode considerations [69, 79]. This thesis develops several new control technologies, analyzes their performance, and demonstrates their potential for improving the feasibility and safety of future spacecraft proximity operations.

Satellite formation flying missions will use coordinated observations between space vehicles to increase the resolution of the science data or achieve faster ground-track repeats [1]. For example, formation flying will be critical for creating large sparse-aperture optical and X-ray telescopes for space science and synthetic aperture radars for earth mapping. As discussed in [26], formation flying combines many component

technologies, such as distributed relative navigation, autonomous control, and distributed fault-protection. This thesis contributes to formation flying control systems in two significant ways: 1) a new linear dynamics model is introduced that extends the range of missions that can be controlled using linear control formulations; and 2) an optimization-based method for finding initial conditions that balances the need to reduce relative drift between satellites against the goals of minimizing fuel use and maintaining desired geometries. The new dynamics are embedded in a model predictive controller and demonstrated in realistic simulation environments.

Autonomous spacecraft rendezvous is an enabling technology for many future space missions [54]. Autonomous rendezvous has been used for docking with Mir [55], and more recently on the ETS-VII [56] and DART [57, 60] missions. However, anomalies occurred during both of these last two missions. In the case of ETS-VII, multiple anomalies caused entries into safe mode over the course of the mission, at least one of which resulted in a preprogrammed maneuver to move the spacecraft 2.5 km from its target. The anomaly in the DART mission is thought to have resulted in excess fuel expenditures and appears to have caused an on-orbit collision [58–60]. These recent experiences suggest that autonomous rendezvous and docking would greatly benefit from the inclusion of additional safeguards to protect the vehicles in the event of failures. Designing approach trajectories that guarantee collision avoidance for some common failures could simultaneously decrease the likelihood of catastrophic failures in which one, or both, of the spacecraft are damaged and increase the likelihood that future attempts at docking succeed. This thesis introduces a method for generating fuel-optimized rendezvous trajectories online that are safe with respect to a large class of possible spacecraft anomalies and demonstrates such a trajectory on a hardware testbed aboard the International Space Station.

## 1.1 Background

### 1.1.1 Formation Flying Control Systems

Formation flying spacecraft pose several control challenges beyond the problem of controlling a monolithic spacecraft or a constellation [5–7, 64]. In a typical single-spacecraft mission, the term *control* would refer to maintaining and altering the attitude of the spacecraft, whereas *guidance* would encompass the maintenance and manipulation of the trajectory on the scale of an orbit. After launch and initial correcting maneuvers, adjusting a spacecraft’s orbit would be an occasional activity planned from the ground. A constellation of spacecraft is operated much the same way [22, 23], because the constituent spacecraft operate in widely spaced orbits, with short-term decoupled performance objectives. A formation of spacecraft is defined by the need for inter-satellite control cooperation [65]. The satellites in a formation are typically represented as sharing a common *reference orbit*, that is, being close enough in terms of their position and velocity in a central body frame that their long-term, large-scale motion can be modeled using the dynamics of a single orbit. This proximity, while typical for rendezvous missions, is uncommon for satellite missions where there is an expectation for long-term collision-free operation. Formation flying is expected to require a level of autonomous onboard guidance that in most applications would be classified as automatic control [3, 8, 9, 65].

Many formation control approaches have been presented in the literature [6, 19, 20, 49, 65, 84, 91, 92, 94, 100, 104]. These papers cover a variety of approaches, including PD, LQR, LMI, nonlinear, Lyapunov, impulsive, RRT, and model predictive. Typically, it is assumed that a formation is initialized to a stable orbit and deviations caused by disturbances such as differential drag and/or differential  $J_2$  must be corrected. Some approaches, such as Lyapunov controllers and PD controllers [92], require that control be applied continuously, a strategy both prone to high fuel use and difficult to implement when thrusting requires attitude adjustment. Other approaches, such as the impulsive thrusting scheme introduced in Ref. [93], require spacecraft to thrust at previously specified times and directions in the orbit, ensuring

many potential maneuvers will not be fuel-optimal.

Model Predictive Control (MPC) can be used to generate optimized plans that satisfy performance constraints [24–26, 49, 73, 84, 101]. MPC using linear programming (LP) has a number of other advantages for spacecraft formation flying: it easily incorporates realistic constraints on thrusting and control performance; it generates plans that closely approximate fuel-optimal “bang-off-bang” solutions rather than the continuous thrusting plans that inevitably arise from LQR,  $H_\infty$ , and Lyapunov controllers; and it allows for piecewise-linear cost functions, such as the 1-norm of fuel use.

### 1.1.2 Linearized Relative Orbital Dynamics

Optimization-based controllers make explicit use of the system dynamics. Because of the advantages of linear optimization (*i.e.*, fast solution times, global optimality), it is preferable to use linear relative dynamics in the model predictive controller. Linear models have the advantage that they can easily exploit the superposition principle to predict the effects of future inputs.

A variety of sets of linear dynamics for relative orbit propagation have been examined in the literature and are summarized in Table 1.1. When spacecraft are in very close proximity (meters) their relative motion is often modeled as a double integrator. More widely separated formations in circular orbits (usually less than 1 km in LEO [115]) can use the Hill-Clohessy-Wiltshire (HCW) equations [75, 76]. For very large formations in circular orbits, there are a number of modifications in the literature that can be used to improve the accuracy of Hill’s equations [45, 117, 118]. For propagation of relative elliptical orbits, Lawden’s equations are valid for any eccentricity [16–18]. However, like Hill’s equations, they degrade quickly with separation distance. Note that both Hill’s and Lawden’s equations have been modified in the literature [88, 116] to include the relative effects of Earth’s oblateness, however, these approaches are still only valid for formations with short baselines.

An alternative to planning in Cartesian frames is using orbital elements, which have been shown to not degrade as rapidly with separation distance [74]. In orbital



**Table 1.1:** Relative orbital dynamics indexed by regime of validity [115]

	$e = 0$ no $J_2$	$0 < e < 1$ no $J_2$	$e = 0$ with $J_2$	$0 < e < 1$ with $J_2$
Linearized Dynamics	Hill's [75]	Lawden [16] Inalhan [109]	Schweighart [116]	Chrétien [88]
Long Baseline Capable	Karlgrad [117] Mitchell [118] Alfriend [45]	Breger [96] Alfriend [119]	Gim [98]	Gim [98]

elements, the relative dynamics can be propagated using Gauss' Variation Equations (GVEs). A state transition matrix capable of propagating spacecraft with large separations in elliptical orbits and incorporate the effects of  $J_2$  is presented in [119]. This thesis builds on the work in [119] to create a discrete input effect matrix that incorporates the effects of the same range of disturbances and use the combined linear time-varying dynamics in a model predictive controller.

### 1.1.3 Formation Flying Initial Conditions

One of the principal requirements of a spacecraft formation is that the component spacecraft do not drift apart from one another [14, 65]. In a fully Keplerian orbit, the only source of drift over multiple orbits is a difference between spacecraft periods, which is equivalent to a difference in spacecraft semimajor axes [15]. The presence of the relative disturbances between spacecraft (*e.g.*, relative drag,  $J_2$ ) can also lead to drift in a formation. An alternative to expending regular control energy to counteract drift is to choose formation initial conditions that reduce relative drift between spacecraft.

Several approaches for creating  $J_2$  invariant relative orbits have recently been proposed in the literature [20, 66, 110]. Different classes of "invariant" orbits have been introduced: those that are truly invariant over time, orbits that retain the same mean period over time, orbits that are invariant except for argument of perigee drift, and orbits that are invariant except for right ascension drift. In the case of

full invariance conditions, where the formation returns to an identical relative state every orbit, the set of relative orbits that satisfy the conditions is very small and the geometry of those orbits is highly restricted [20]. Hence, it is more common for a  $J_2$ -invariant orbit to only be invariant in a reduced set of dimensions for which it is possible to analytically cancel the relative effects of  $J_2$ . In all of the aforementioned invariance cases, the drift being minimized is secular variation in the mean orbital elements.

#### 1.1.4 Safety in Autonomous Rendezvous and Docking

Numerous methods for generating rendezvous trajectories exist in the literature and encompass a wide range of rendezvous scenarios [61–63, 67, 79]. Those papers consider rendezvous from many perspectives, often taking into account complicated collision avoidance constraints, nonlinear rotational dynamics, and fuel efficiency. Another perspective to be considered when designing trajectories is safe behavior [67–70]. Safety in the context of spacecraft rendezvous and docking is typically with respect to collision avoidance following some type of failure. The approach in Ref. [70] creates trajectories which naturally tend to drift away from the target spacecraft in the absence of thrusting. This method can guarantee safety for thruster failures, but is not fuel-optimized and does not apply to more complicated docking situations in which those trajectories cannot be used for nominal rendezvous.

Alternately, Refs. [67] and [68] develop the *safety circle* method, in which a nearby orbit with a relative invariant trajectory is established that allows safe long-term observation before docking, however this approach is not fuel optimized and does not propose a specific docking path. A method proposed in Ref. [69] optimizes both safety and fuel using genetic algorithms. This approach treats safety as a goal rather than a constraint and thus, cannot assure that the resulting trajectory would be safe. Ref. [79] plans safe trajectories using potential functions, but the approach is computationally intensive and limited to static obstacles. Various types of safety have been considered in the design of UAV trajectories, but these focused on creating trajectories that are safe under nominal operating conditions (*e.g.*, safety from adversaries,

uncertain terrain)[71, 72].

## 1.2 Thesis Overview

This thesis develops and validates technologies that improve the state of the art in control for formation flying spacecraft and for the autonomous rendezvous of spacecraft. The chapters and their contributions are:

Chapter 2 develops, validates, and analyzes a set of time-varying linearized relative spacecraft dynamics that advances the state of the art by incorporating three dominant orbital effects not previously accommodated together: 1) Orbit eccentricity; 2) nonlinearity due to large separation distances between spacecraft; and 3) Earth oblateness. All three are expected to be present in the planned MMS mission [86]. Continuous- and discrete-time versions of the new dynamics are presented and linearization assumptions for each are evaluated. The dynamics are embedded in an LP-based model-predictive control system and demonstrated controlling a four spacecraft formation in a highly elliptic orbit in the presence of realistic disturbances and navigation uncertainty.

Chapter 3 discusses the use of the dynamics presented in Chapter 2 in a linear optimization-based initialization algorithm that produces fuel-minimizing invariant orbits. This approach improves existing techniques for producing invariant orbits by explicitly considering multiple objectives in its cost function. The costs minimized are: 1) Cartesian, mean, and/or osculating drift over arbitrary time frames; 2) fuel costs associated with maneuvering to the desired initial conditions; and 3) the distance of the initial conditions from a desired formation geometry (*e.g.*, a shape appropriate for observation or science data collection). Existing techniques rely either on analytic conditions to prevent mean drift over an infinite horizon with no notion of fuel or geometry cost; or on large nonlinear optimization techniques that are ill-suited to onboard deployment. This chapter investigates the ranges of solutions available for large ranges of objective weights and compares those solutions to semi-invariant conditions available through analytic techniques.

Chapter 4 uses the controller/dynamics combination developed in Chapter 2 to examine a realistic formation flying mission scenario and evaluate the effectiveness of control parameter settings. The mission examined has three satellites and maneuvers between multiple formation configurations (1 km in-track, 50 m passive aperture, 500 m passive aperture, 5 km passive aperture) in which station-keeping is performed using 10% baselines for hard error box constraints. Each simulation covers a multi-week period to demonstrate formation stability and to determine steady-state fuel use. The effects of constraints on passive operation during science data collection on fuel use and performance constraint satisfaction in the presence of navigation error are investigated. Variations of optimization terminal conditions and error box relaxations are also examined.

Chapter 5 introduces a new approach to guaranteeing safety against failures in autonomous rendezvous and docking maneuver generation for spacecraft. The maneuver generation algorithm uses the same LP-based optimization as the model predictive controller in Chapter 2 to minimize fuel, but uses additional linear constraints to ensure safety. No other guaranteed-safe rendezvous methods in the literature also minimize fuel use. The approach in this chapter has the added advantage of being valid for safe docking with general polygonal target shapes experiencing arbitrary, but known, attitude motion under any relative linear dynamics. The fuel cost associated with imposing safety as a constraint is investigated and the value of adding safety is established through stochastic analysis. In addition, a modification to the safe trajectory formulation is examined that, through use of the invariance concept in Chapter 3, enables infinite horizon passive safe collision-avoidance guarantees. A convex formulation of the safety constraint is developed and analyzed in terms of fuel cost and computation trades. Also, an active form of safety is developed and evaluated that greatly expands the space of safe rendezvous maneuvers by allowing powered abort trajectories.

Chapter 6 applies the safe rendezvous generation techniques developed in Chapter 5 to use on a hardware testbed aboard the International Space Station. Both nominal and stochastic passive-abort cases are examined. Additional testing is con-

ducted using a similar terrestrial testbed.

Chapter 7 summarizes the main contributions of the thesis to the state of the art in formation flying control and autonomous rendezvous and docking of spacecraft. These contributions are to linearized relative dynamics, initialization techniques, and safety in autonomous rendezvous and docking.



## Chapter 2

# GVE-based Dynamics and Control for MPC

This chapter presents several modeling and control extensions that would enhance the efficiency of many formation flying missions. In particular, a new linear time-varying form of the equations of relative motion is developed from Gauss' Variational Equations. These new equations of motion are further extended to account for the effects of  $J_2$ , and the linearizing assumptions are shown to be consistent with typical formation flying scenarios. It is then shown how these models can be used to control general formation configurations in an embedded on-line, optimization-based, model predictive controller (MPC). A convex, linear approach for initializing fuel-optimized, partially  $J_2$  invariant orbits is developed and compared to analytic approaches. All control methods are validated using a commercial numerical propagator. The simulation results illustrate that formation flying using this MPC with  $J_2$ -modified GVEs requires fuel use that is comparable to using unmodified GVEs in simulations that do not include the  $J_2$  effects.

## Nomenclature

$a$  = semimajor axis

$e$  = eccentricity

$i$  = inclination

$\Omega$  = right ascension of the ascending node

$\omega$  = argument of perigee

$M$  = mean motion

$p$  = semilatus rectum

$b$  = semiminor axis

$h$  = angular momentum

$\theta$  = argument of latitude

$r$  = magnitude of radius vector

$n$  = mean motion

## 2.1 Background

Formation control objectives typically focus on controlling the relative states of the spacecraft, the dynamics of which can be captured using variants of Hill's and Lawden's equations for LEO missions [84]. However, both of these approaches linearize the nonlinear relative spacecraft motions about a reference orbit, which is only valid for small separation distances of the satellites in the formation relative to the reference orbit radius. For larger separations, these equations of motion can no longer be used to cancel relative drift rates (initialization) or to accurately predict the effect of inputs (control) [85]. For example, the four spacecraft of the planned MMS mission [86] will be placed in a tetrahedron-shaped relative configuration with sides ranging between 10–1000 km at apogee, which far exceeds the separations for which Hill's and Lawden's models are valid for a full HEO orbit, even with the correction terms introduced in Ref. [87]. Furthermore, these models do not accurately capture the effects of Earth's oblateness, which Ref. [20] showed can lead to very inefficient control designs. This chapter develops a new linearized modeling approach that is valid for widely-spaced formations in highly elliptic orbits, accurately captures the effects of the Earth's gravity, and can be embedded in an optimization-based controller



that is suitable for real-time calculations.

The relative dynamics used in this chapter are based on a form of Gauss' Variational Equations (GVEs) that have been modified to include the effects of  $J_2$ . GVEs are convenient for specifying and controlling widely separated formations because they are linearized about orbital elements, which are expressed in a curvilinear frame in which large rectilinear distances can be captured by small element perturbations [89]. This bypasses the linearization error created by representing the entire formation in a single rectilinear frame, which was the approach used in Ref. [84]. The use of GVE dynamics as opposed to Hill's dynamics incurs the cost of computation associated with the use of multiple sets of time-varying equations of motion. Specifying a formation's relative geometry in terms of differential orbital elements is an exact approach that does not degrade for large spacecraft separations. However, the advantage of using GVEs for control could be reproduced by using Lawden's equations of motion in a different LVLH frame for each spacecraft in the formation while still using orbital element differences to represent the formation relative geometry. Given that a nonlinear transformation and rotation is required to switch between an LVLH frame and orbital element differences, and that GVEs are already linearized in an orbital element frame, it is both simpler and computationally more efficient to use orbital element differences to specify the formation configuration and GVEs for control.

Many formation control approaches have used GVEs for nonlinear, continuous control [90–92] and also for impulsive control [93, 94]. This chapter introduces a control law that generally does not fire continuously and, more importantly, makes explicit its objective to minimize fuel use, which is measured in  $\Delta V$  in this chapter. The control approach optimizes the effects of arbitrarily many inputs over a chosen planning horizon. Plans are regularly re-optimized, forming a closed-loop system [95]. By extending previous planning approaches [84, 96] to use GVEs, we can optimize the plans for spacecraft in widely-separated, highly elliptic orbits. Results are presented to show that the GVE-based planning system is more fuel-efficient than the four-impulse method in Ref. [93]. In addition, control optimized online has the advantage of being capable of handling many types of constraints, such as limited thrust capability,

sensor noise robustness, and error box maintenance [84]. We also extend the *virtual center* approach to formation flying in Ref. [97] to GVEs and present a decentralized implementation of that algorithm.

A limitation of the orbital element approach in Ref. [96] is that it does not account for the effects of the  $J_2$  disturbance, which impacted the closed-loop performance in full nonlinear simulations. This chapter extends the use of the relative orbital elements in Ref. [96] to the  $J_2$ -modified relative state transition matrix in Ref. [98] and develops and evaluates several approaches for including the effects of thruster inputs. The resulting  $J_2$ -modified GVEs are used to form a set of linear parameter-varying dynamics that can be embedded in an optimization-based control system. The combination creates a controller that retains the advantages of the GVE-based controller in Ref. [96], but uses a more accurate dynamics model, thereby improving plan tracking and fuel efficiency. In particular, simulations are presented to show that the new controller in the presence of  $J_2$  disturbances requires comparable levels of fuel to the approach in Ref. [96] when no  $J_2$  disturbances are simulated in the model.

## 2.2 Relative Orbital Elements and Linearization Validity

Gauss' Variational Equations (GVEs) are derived in Ref. [99] and are reproduced here for reference

$$\frac{d}{dt} \begin{pmatrix} a \\ e \\ i \\ \Omega \\ \omega \\ M \end{pmatrix} = \begin{pmatrix} 0 \\ 0 \\ 0 \\ 0 \\ 0 \\ n \end{pmatrix} + \begin{pmatrix} \frac{2a^2 e \sin f}{h} & \frac{2a^2 p}{rh} & 0 \\ \frac{p \sin f}{h} & \frac{(p+r) \cos f + re}{h} & 0 \\ 0 & 0 & \frac{r \cos \theta}{h} \\ 0 & 0 & \frac{r \sin \theta}{h \sin i} \\ -\frac{p \cos f}{he} & \frac{(p+r) \sin f}{he} & -\frac{r \sin \theta \cos i}{h \sin i} \\ \frac{b(p \cos f - 2re)}{ahe} & -\frac{b(p+r) \sin f}{ahe} & 0 \end{pmatrix} \begin{pmatrix} \mathbf{u}_r \\ \mathbf{u}_\theta \\ \mathbf{u}_h \end{pmatrix} \quad (2.1)$$

where the state vector elements are  $a$  (semimajor axis),  $e$  (eccentricity),  $i$  (inclination),  $\Omega$  (right ascension of the ascending node),  $\omega$  (argument of periapse), and  $M$  (mean motion). The other terms in the variational expression are  $p$  (semi-latus rectum),  $b$  (semiminor axis),  $h$  (angular momentum),  $\theta$  (argument of latitude),  $r$  (magnitude of radius vector), and  $n$  (mean motion). All units are in radians, except for semi-major axis and radius (meters), angular momentum (kilogram  $\cdot$  meters<sup>2</sup> per second), mean motion (1/seconds), and eccentricity (dimensionless). The input acceleration components  $\mathbf{u}_r$ ,  $\mathbf{u}_\theta$ , and  $\mathbf{u}_h$  are in the radial, in-track, and cross-track directions, respectively, of an LVLH frame centered on the satellite and have units of meters per second<sup>2</sup>. Although the traditional Keplerian form of the orbital elements is used in this chapter for conceptual clarity, later uses of transformations from Refs. [98] and [100] require a conversion to the nonsingular form described in those references. The form of the GVEs can be more compactly expressed as

$$\dot{\mathbf{e}} = A(\mathbf{e}) + B(\mathbf{e})\mathbf{u} \quad (2.2)$$

where  $\mathbf{e}$  is the state vector in Eq. (2.1),  $B(\mathbf{e})$  is the input effect matrix,  $\mathbf{u}$  is the vector of thrust inputs in the radial, in-track, and cross-track directions, and  $A(\mathbf{e}) = (0 \ 0 \ 0 \ 0 \ 0 \ \sqrt{\mu/a^3})^T$ , where  $\mu$  is the gravitational parameter.

In a formation, the orbital element state of the  $i$ th satellite is denoted  $\mathbf{e}_i$ . The states of the vehicles in the formation can be specified by relative orbital elements by subtracting the state of an arbitrarily chosen spacecraft in the formation, which is designated as  $\mathbf{e}_1$

$$\delta\mathbf{e}_i = \mathbf{e}_i - \mathbf{e}_1 \quad (2.3)$$

For a desired orbit geometry, a set of desired relative elements,  $\delta\mathbf{e}_{di}$  will specify the desired state  $\mathbf{e}_{di}$  of each spacecraft in the formation<sup>1</sup>.

$$\mathbf{e}_{di} = \mathbf{e}_1 + \delta\mathbf{e}_{di} \quad (2.4)$$

---

<sup>1</sup>Approaches for choosing and coordinating the desired spacecraft states will be addressed in Sections 2.4 and Chapter 3.

The state error for the  $i$ th spacecraft in the formation,  $\zeta_i$ , is then defined as

$$\zeta_i = \mathbf{e}_i - \mathbf{e}_{di} = \delta \mathbf{e}_i - \delta \mathbf{e}_{di} \quad (2.5)$$

Note that the definition of state error given in Eq. (2.5) is independent of the choice of which spacecraft state is represented by  $\mathbf{e}_1$ . The form of Gauss' Variational Equations in Eq. (2.1) is for perturbations of orbital elements. To reformulate these equations for perturbations of relative orbital elements [100], the GVEs for  $\mathbf{e}_i$  and  $\mathbf{e}_{di}$  are combined

$$\dot{\zeta}_i = \dot{\mathbf{e}}_i - \dot{\mathbf{e}}_{di} = A(\mathbf{e}_i) - A(\mathbf{e}_{di}) + B(\mathbf{e}_i)\mathbf{u}_i \quad (2.6)$$

where the term  $B(\mathbf{e}_{di})\mathbf{u}_{di}$  has been excluded, since thrusting does affect the desired state of the spacecraft. The unforced dynamics can be linearized by introducing the first-order approximation [100]<sup>2</sup>

$$A(\mathbf{e}) - A(\mathbf{e}_d) \simeq \left. \frac{\partial A}{\partial \mathbf{e}} \right|_{\mathbf{e}_d} (\mathbf{e} - \mathbf{e}_d) = \left. \frac{\partial A}{\partial \mathbf{e}} \right|_{\mathbf{e}_d} \zeta \equiv A^*(\mathbf{e}_d)\zeta \quad (2.7)$$

where the matrix  $A^*(\mathbf{e}_d)$  is all zeros except for the lower-leftmost element, which is  $-3n/2a$ , where the sparsity of  $A^*$  arises from the sparsity of the  $A$  function in Eq. (2.2). With this approximation, the differential GVE expression in Eq. (2.6) can be rewritten as

$$\dot{\zeta} = A^*(\mathbf{e}_d)\zeta + B(\mathbf{e})\mathbf{u} = A^*(\mathbf{e}_d)\zeta + B(\mathbf{e}_d + \zeta)\mathbf{u} \quad (2.8)$$

In this case the control of the relative error state,  $\zeta$ , is nonlinear, because the control effect matrix  $B$  is a function of the state. Ref. [100] accounts for this nonlinearity in a continuous nonlinear control law that was shown to be asymptotically stable. The control approach developed in this section uses linearized dynamics to predict the

---

<sup>2</sup>The subscript  $i$  is henceforth omitted for notational simplicity.

effect of future control inputs. Linearizing the matrix  $B$  in Eq. (2.8) yields

$$\dot{\zeta} \simeq A^*(\mathbf{e}_d)\zeta + \left( B(\mathbf{e}_d) + \left. \frac{\partial B}{\partial \mathbf{e}} \right|_{\mathbf{e}_d} \zeta \right) \mathbf{u} = A^*(\mathbf{e}_d)\zeta + B(\mathbf{e}_d)\mathbf{u} + [B^*(\mathbf{e}_d)]\zeta\mathbf{u} \quad (2.9)$$

where the term  $B^*(\mathbf{e}_d)$  is a third rank tensor and the quantity  $B^*(\mathbf{e}_d)\zeta$  is a matrix with the same dimensions as  $B(\mathbf{e}_d)$ . For convenience, define

$$\Delta B(\mathbf{e}_d, \zeta) \equiv B^*(\mathbf{e}_d)\zeta \quad (2.10)$$

resulting in the new state equation

$$\dot{\zeta} = A^*(\mathbf{e}_d)\zeta + (B(\mathbf{e}_d) + \Delta B(\mathbf{e}_d, \zeta)) \mathbf{u} \quad (2.11)$$

Note that if  $\Delta B$  is much smaller than  $B(\mathbf{e}_d)$ , then the first-order term can safely be ignored, yielding the approximate linearized dynamics

$$\dot{\zeta} = A^*(\mathbf{e}_d)\zeta + B(\mathbf{e}_d)\mathbf{u} \quad (2.12)$$

which can be controlled by any one of a variety of linear control techniques, including the model predictive controller discussed in Section 2.4.

The critical requirement for linear control and planning is that the term  $\Delta B$  has a much smaller influence on the state dynamics than the term  $B(\mathbf{e}_d)$ . However,  $\Delta B$  is a linear function of the state error  $\zeta$ , which can be arbitrarily large. The amount of acceptable error due to linearization will be a function of the mission scenario, but the linearization assumption will typically only be valid for small values of the state error. It is reasonable to expect that the values of state error will be small, because the linearization is only in separation between a spacecraft and its desired orbit. For a given desired orbit, a bound can be established numerically that indicates the state separation from an orbit where the dynamics linearization is valid. This section examines several example orbits that are representative of space missions that might occur in Low Earth Orbits and Highly Elliptical orbits. In each case, this range

of acceptable error is found to be large enough to accommodate expected mission performance requirements.

The magnitude of the acceptable error can be computed by comparing the induced norm of the difference between the control influence matrix at its desired state,  $B(\mathbf{e}_d)$  and at the actual position of the spacecraft,  $B(\mathbf{e})$ . In Eq. (2.10), the first order approximation of this term was defined as  $\Delta B$ . In the following examples,  $\Delta B_{\text{true}}$ , which is defined as

$$\Delta B(\mathbf{e}_d, \zeta)_{\text{true}} \equiv B(\mathbf{e}) - B(\mathbf{e}_d) = B(\mathbf{e}_d + \zeta) - B(\mathbf{e}_d) \quad (2.13)$$

and will be calculated numerically. The cut-off point of acceptable linearization error is when the norm of  $\Delta B$  exceeds some (possibly mission dependent) fraction of the norm of  $B(\mathbf{e}_d)$ . To investigate this cut-off point, the following examples consider many random values of  $\zeta$  in the set  $\|\zeta\|_2 = r$  and calculate  $\Delta B_{\text{true}}$ . The  $\Delta B_{\text{true}}$  with the largest 2-norm will be used to test the validity of the linearization for a given  $r$ . This procedure is repeated for multiple  $r$  to find the largest  $\|\zeta\|_2$  for which the linearization is considered valid. Other methods of examining the linearization error of  $B$  are possible, but the approach used in this chapter was chosen because of its ease of implementation and consistent results for particular mission types.

**Example: Low Earth Orbit** – An example low Earth orbit is

$$\mathbf{e}_d = \left( 1.08182072 \quad 0.005000000 \quad 0.610865238 \quad 2\pi \quad \pi \quad 3.82376588 \right)^T \quad (2.14)$$

where the first element, semimajor axis, is normalized by the Earth's radius, making

the orbital element vector dimensionless. The matrix corresponding  $B(\mathbf{e}_d)$  is

$$B(\mathbf{e}_d) = \begin{pmatrix} -5.6794478 & 1808.6011 & 0 \\ -0.000082308780 & -0.00020502572 & 0 \\ 0 & 0 & 0.00010304404 \\ 0 & 0 & 0.00014406293 \\ 0.020528419 & -0.032987976 & -0.00011800944 \\ -0.020792326 & 0.032987564 & 0 \end{pmatrix} \quad (2.15)$$

where  $\|B(\mathbf{e}_d)\|_2 = 1808.61$ . The effect of perturbing  $\mathbf{e}_d$  for a given norm bound on  $\zeta$  is shown in Figure 2-1. The plots show that an arbitrary linearization validity cutoff of 0.01, i.e.,  $\|\Delta B(\mathbf{e}_d, \zeta)_{\text{true}}\|_2 \leq 0.01\|B(\mathbf{e}_d)_{\text{true}}\|_2$ , can be achieved by ensuring that  $\|\zeta\|_2 \leq 8.16 \times 10^{-3}$ . This bound on  $\zeta$  allows for orbital element perturbations that equate to rectilinear distances on the order of 25 kilometers and velocities on the order of 40 m/s. Typical error box sizes for LEO formation flying missions are 10-100 meters in size [4], decidedly inside the linearization range of the LEO orbit examined.

**Example: Highly Elliptical Earth Orbit** – One motivation for using GVEs as the linearized dynamics in a planner is recent interest in widely spaced, highly elliptical orbits [86]. An orbit of this type is

$$\mathbf{e}_d = \begin{pmatrix} 6.59989032 & 0.818181000 & 0.174532925 & 2\pi & 0 & \pi \end{pmatrix}^T \quad (2.16)$$

with

$$B(\mathbf{e}_d) = \begin{pmatrix} 4.767920 \times 10^{-12} & 8651.830 & 0 \\ 2.288208 \times 10^{-20} & -0.0003736926 & 0 \\ 0 & 0 & -0.001027650 \\ 0 & 0 & 7.247461 \times 10^{-19} \\ 0.0002283680 & 1.817849 \times 10^{-19} & -7.137356 \times 10^{-19} \\ -0.001313020 & -1.45192 \times 10^{-19} & 0 \end{pmatrix} \quad (2.17)$$

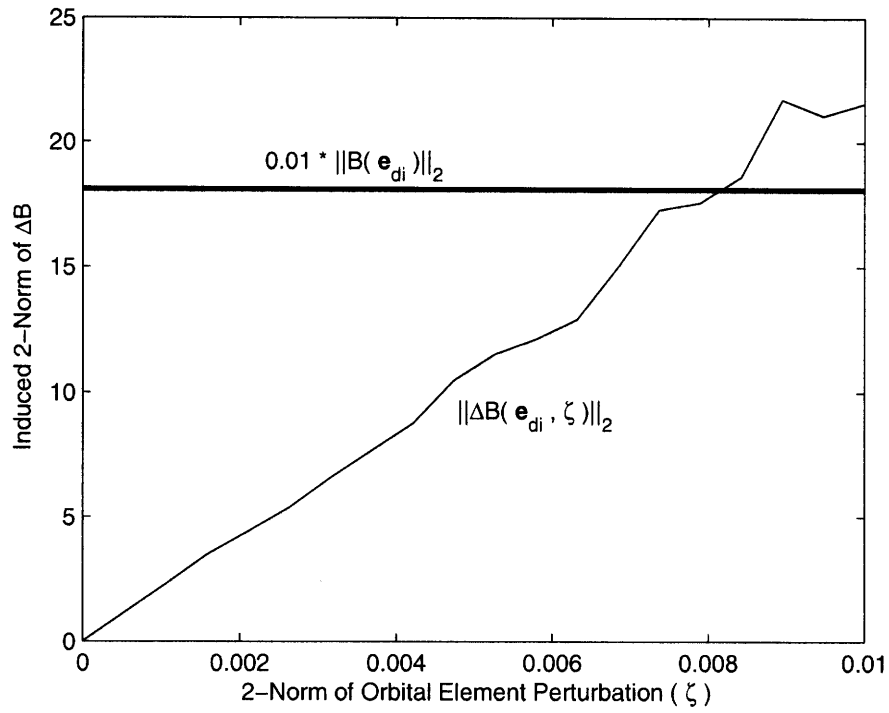


**Fig. 2-1:** Effect of Orbital Element Perturbations on the  $\Delta B_{\text{true}}$  Matrix for a LEO Orbit

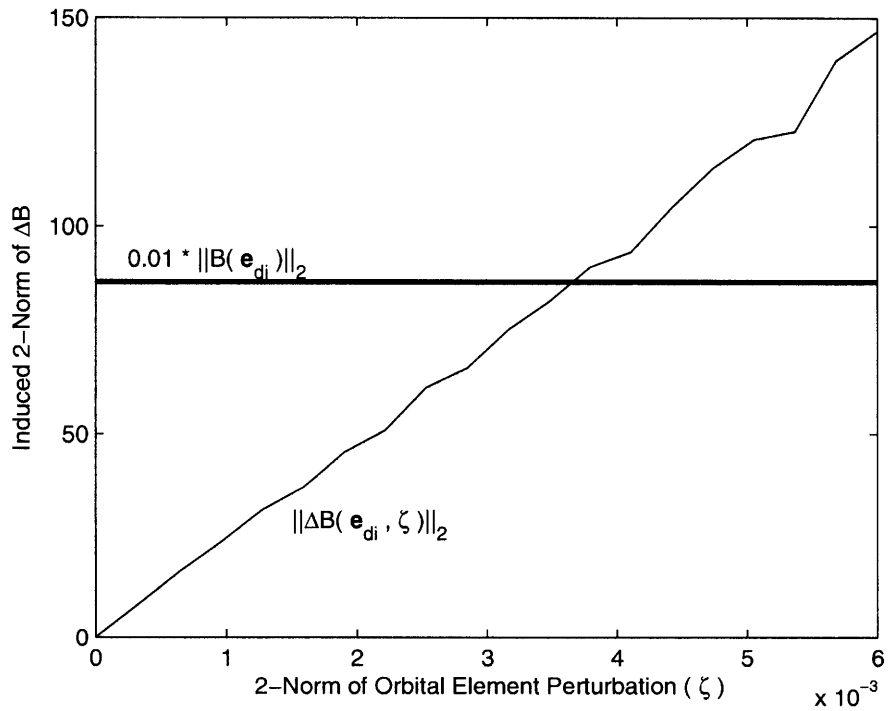


**Fig. 2-2:** Effect of Orbital Element Perturbations on the  $\Delta B_{\text{true}}$  Matrix for a HEO Orbit



Repeating the same procedure used for the LEO case, it is determined from Figure 2-2 that an arbitrary 1% linearization validity cutoff can be achieved provided that  $\|\zeta\|_2 \leq 3.66 \times 10^{-3}$ . In this case, the bound on  $\|\zeta\|_2$  corresponds to rectilinear distances of approximately 50 kilometers and velocities of 2 meters per second. As in the LEO case, these distances are far larger than expected error box sizes. Since any planned trajectory would be expected to remain inside an error box at all times, the range of state errors in which the linearization is valid will not be exceeded. Unlike the LEO case, error boxes for widely-separated missions, such as MMS, may be much larger than 10 meters to a side, even approaching kilometers. The 1% cutoff ensures that error boxes of up to 5% of the distance between MMS satellites (1000 km during the most widely spaced phase of the mission) are acceptable [86].

Validating the linearization for additional reference orbits is a straightforward computational exercise. For example, repeating the validation process for the LEO orbits used in Chapter 3 and the HEO orbits used in the simulations in Section 2.6 yielded valid ranges of separation that were far larger than the expected error box sizes.

## 2.3 $J_2$ -Modified GVEs and Linearization Validity

Just as the GVEs in Eq. (2.2) express the motion of a Keplerian orbit, the equations of motion of the mean orbital element state vector  $\mathbf{e}_m$  describes the average motion of an orbit influenced by Earth oblateness effects and are given by

$$\dot{\mathbf{e}}_m = \bar{A}(\mathbf{e}_m) + \frac{\partial \dot{\mathbf{e}}_m}{\partial \mathbf{u}} \mathbf{u} \quad (2.18)$$

where  $\bar{A}$  is explicitly a function of the mean state and implicitly a function of  $J_2$ , see Ref. [100]. Although Eqs. (2.2) and (2.18) appear similar, there are some important differences. In particular, Eq. (2.2) describes the motion of a spacecraft's osculating orbit and is the form of the classical GVEs. Section 2.2 established that it is valid and effective to linearize the GVEs and use them for model predictive control. However,

the GVEs incorporate neither the absolute nor the relative effects of  $J_2$  on a satellite's orbit. Conversely, Eq. (2.18) describes the motion of an orbit in a set of mean orbital elements, where the secular effects of  $J_2$  are incorporated and harmonics are removed. This form of the dynamics is useful for controlling the secular drift between satellites in a formation, but does not describe the physical motion and has limited applicability for missions with high precision relative state constraints. Furthermore, Eq. (2.18) is nonlinear in terms of the relative state, which accurately captures the system dynamics, but complicates the optimization of the control inputs. The following shows that, by utilizing the linearized propagation and rotation matrices developed in Ref. [98], a linearized form of the equations of relative motion in Eq. (2.18) can be derived that incorporates the osculating effects of  $J_2$ , is linear parameter varying, and is valid for large spacecraft separations and reference orbit eccentricities.

The control influence matrix for mean element motion is derived using the transformation matrices between the mean and osculating motion. The following identity is used to define these transformations,

$$\frac{\partial \dot{\mathbf{e}}_m}{\partial \mathbf{u}} = \left( \frac{\partial \dot{\mathbf{e}}_m}{\partial \dot{\mathbf{e}}} \right) \left( \frac{\partial \dot{\mathbf{e}}}{\partial \mathbf{u}} \right) \quad (2.19)$$

From the appendix of Ref. [20], the relation between the mean orbital element state vector and the osculating orbital element state vector can be written as  $\mathbf{e}_m = f(\mathbf{e})$ , so that

$$\dot{\mathbf{e}}_m = \frac{\partial f(\mathbf{e})}{\partial \mathbf{e}} \dot{\mathbf{e}} \quad \Rightarrow \quad \frac{\partial \dot{\mathbf{e}}_m}{\partial \dot{\mathbf{e}}} = \frac{\partial f(\mathbf{e})}{\partial \mathbf{e}} \quad (2.20)$$

Substituting Eq. (2.20) and the  $B$  matrix from Eq. (2.2) into Eq. (2.19) gives

$$\frac{\partial \dot{\mathbf{e}}_m}{\partial \mathbf{u}} = \frac{\partial f(\mathbf{e})}{\partial \mathbf{e}} B(\mathbf{e}) \quad (2.21)$$

which yields the equations of motion of the mean orbit in terms of the osculating orbital state vector  $\mathbf{e}$  (the mean elements may be considered a function of the osculating

elements) and an input vector  $\mathbf{u}$  as

$$\dot{\mathbf{e}}_m = \bar{A}(\mathbf{e}_m) + \frac{\partial f(\mathbf{e})}{\partial \mathbf{e}} B(\mathbf{e}) \mathbf{u} \quad (2.22)$$

The actual mean orbit  $\mathbf{e}_m$  is now defined in terms of a desired mean orbit  $\mathbf{e}_{md}$  and a vector offset  $\zeta_m$

$$\mathbf{e}_m = \mathbf{e}_{md} + \zeta_m \quad (2.23)$$

Rearranging this expression and applying Eq. (2.18) gives

$$\dot{\mathbf{e}}_m - \dot{\mathbf{e}}_{md} = \dot{\zeta}_m = \bar{A}(\mathbf{e}_m) - \bar{A}(\mathbf{e}_{md}) + \frac{\partial \dot{\mathbf{e}}_m}{\partial \mathbf{u}} \mathbf{u} \quad (2.24)$$

where the term  $\frac{\partial \dot{\mathbf{e}}_{md}}{\partial \mathbf{u}} \mathbf{u}$  is omitted because the desired orbit is fixed and not subject to thrusting. Similar to the previous section, the following linearization approximation can be made [100]

$$\bar{A}(\mathbf{e}_m) - \bar{A}(\mathbf{e}_{md}) \approx \left. \frac{\partial \bar{A}}{\partial \mathbf{e}_m} \right|_{\mathbf{e}_{md}} \zeta_m \equiv \bar{A}^*(\mathbf{e}_{md}) \zeta_m \quad (2.25)$$

which is then used to find the equations of motion of the mean element offset  $\zeta_m$

$$\dot{\zeta}_m = \bar{A}^*(\mathbf{e}_{md}) \zeta_m + \frac{\partial \dot{\mathbf{e}}_m}{\partial \mathbf{u}} \mathbf{u} \quad (2.26)$$

where the terms of the matrix function  $\bar{A}^*$  are given in Ref. [100]. Equation (2.26) provides a linear description of the motion of the relative mean orbital elements. However, the mean orbit describes where the spacecraft is in an average sense, whereas the osculating orbits specifies the actual position of spacecraft. Thus, to maximize the ability of the planner to exploit natural dynamics and operate with tight performance constraints, it is preferable to plan in terms of the osculating orbit. The approach in this chapter uses a hybrid of the osculating and mean to capture both the effects of  $J_2$  and plan in a way that accounts for the actual motion of the spacecraft. Having developed the relative dynamics in terms of the mean elements, we now convert to an osculating state.

Using the notation in Eq. (2.5), formation relative dynamics can be specified in terms of the osculating orbit  $\mathbf{e}$ , an osculating desired orbit  $\mathbf{e}_d$ , and an osculating orbital offset  $\zeta$  between them. The mean elements are expressed as functions of the osculating elements by rearranging the state error form in Eq. (2.23). This is used to create a relative state and a linearized rotation matrix for transitioning between the mean and osculating equations of relative motion.

Given that  $\mathbf{e}_m = f(\mathbf{e})$  and  $\mathbf{e}_{md} = f(\mathbf{e}_d)$ , then using Eq. (2.5), Eq. (2.23) can be rewritten as

$$\zeta_m = f(\mathbf{e}) - f(\mathbf{e}_d) \approx \left. \frac{\partial f(\mathbf{e})}{\partial \mathbf{e}} \right|_{\mathbf{e}_d} \zeta \quad (2.27)$$

by utilizing the same linearization approach in Ref. [100]. Defining the matrix function  $D$  (available in Ref. [98]),

$$D(\mathbf{e}_d) \equiv \left. \frac{\partial f(\mathbf{e})}{\partial \mathbf{e}} \right|_{\mathbf{e}_d} \quad (2.28)$$

and substituting into Eq. (2.21) and then into Eq. (2.26) yields

$$\dot{\zeta}_m = \bar{A}^*(f(\mathbf{e}_d))\zeta_m + D(\mathbf{e})B(\mathbf{e})\mathbf{u} \quad (2.29)$$

This form of the relative equations of motion is nonlinear in terms of the osculating absolute state  $\mathbf{e}$ . Making the linearizing assumption (accuracy of the linear approximations is discussed later in this section)

$$D(\mathbf{e})B(\mathbf{e}) = D(\mathbf{e}_d + \zeta)B(\mathbf{e}_d + \zeta) \approx D(\mathbf{e}_d)B(\mathbf{e}_d) \quad (2.30)$$

allows the relative equations of motion to be rewritten as

$$\dot{\zeta}_m = \bar{A}^*(f(\mathbf{e}_d))\zeta_m + D(\mathbf{e}_d)B(\mathbf{e}_d)\mathbf{u} \quad (2.31)$$

which has a desired osculating orbit  $\mathbf{e}_d$  and is linear in terms of the relative mean state  $\zeta_m$ . The equations of motion in Eq. (2.31) are still not suited to control of the osculating relative orbit in the presence of  $J_2$ , because they describe the derivative of the mean state. The following section derives a form of discrete dynamics that use a

relative osculating orbit as their state.

### 2.3.1 Extension to Discrete Time

To use Eq. (2.31) in an optimization-based controller of the type used in Ref. [96], it must first be discretized. Reference [98] introduces the state transition matrix  $\bar{\Phi}$ , which is the discrete form of the continuous matrix  $\bar{A}^*(f(\mathbf{e}_d))$ , and is defined such that

$$\zeta_m(t_1) = \bar{\Phi}^*(\mathbf{e}_{md}(t_0), t_1, t_0)\zeta_m(t_0) \quad (2.32)$$

where  $t_0$  and  $t_1$  are the times of the initial and final states, respectively, and are provided as arguments to the state vectors. The analytic definition of the matrix  $\bar{\Phi}^*$  (an implicit function of  $J_2$  and a highly nonlinear function of the mean absolute elements) is included in the appendices of Ref. [98].

The dynamics in Eq. (2.31) can be formulated exclusively in terms of the osculating state. Using Eq. (2.27), define  $D^{-1}$  as

$$D^{-1}(\mathbf{e}_d) \equiv \left. \frac{\partial \mathbf{e}}{\partial f(\mathbf{e})} \right|_{\mathbf{e}_d} \quad (2.33)$$

Substituting Eqs. (2.28) and (2.33) into Eq. (2.32) yields

$$\zeta(t_1) \approx D^{-1}(\mathbf{e}_d(t_1))\bar{\Phi}^*(\mathbf{e}_{md}(t_0), t_1, t_0)D(\mathbf{e}_d(t_0))\zeta(t_0) \quad (2.34)$$

The analogous discrete form of the control influence matrix  $B$  on the osculating state is then given by

$$\Gamma(\mathbf{e}_d(t_0), t_1, t_0) = \int_{t_0}^{t_1} D^{-1}(\mathbf{e}_d(t_1))\bar{\Phi}^*(\mathbf{e}_{md}(\tau), t_1, \tau)D(\mathbf{e}_d(\tau))B(\mathbf{e}_d(\tau))d\tau \quad (2.35)$$

Thus, combining Eqs. (2.32) and (2.35) yields the discrete time equations of motion

$$\zeta(t_1) \approx D^{-1}(\mathbf{e}_d(t_1))\bar{\Phi}^*(\mathbf{e}_{md}(t_0), t_1, t_0)D(\mathbf{e}_d(t_0))\zeta(t_0) + \Gamma(\mathbf{e}_d(t_0), t_1, t_0)\mathbf{u} \quad (2.36)$$

which are the linear parameter-varying discrete equations of motion for a relative osculating orbit in the presence of  $J_2$ .

### 2.3.2 Validity of the Linearization Approximations

Reference [87] showed that the approximation  $B(\mathbf{e}_d) \approx B(\mathbf{e}_d + \zeta)$ , which is used to derive Eq. (2.36), is a sufficiently close approximation for levels of state error,  $\zeta$ , that would normally be expected in spacecraft formation flying missions. In order to use Eq. (2.36) for linear control, it must also be shown that the linearized rotation and transition combination  $D^{-1}(\mathbf{e}_d(t_1))\bar{\Phi}^*(\mathbf{e}_{md}(t_0), t_1, t_0)D(\mathbf{e}_d(t_0))$  remains a close approximation for expected values of  $\zeta$ . Ref. [98] showed this matrix has low linearization error for a wide range of reference orbit eccentricities and spacecraft formation baselines in excess of 10 km. By specifying the chief orbit in Ref. [98] as the desired spacecraft state, the transition matrices then allow a maximum state error of 10 km, which is much larger than the error that would be tolerated in most proposed spacecraft formation flying missions.

### 2.3.3 Calculating the $\Gamma$ matrix

The discrete control effect matrix is defined as a matrix integral in Eq. (2.35). One way to calculate this matrix is by computing its derivative and numerically integrating. However, in practice this is a computationally intensive approach that may not be consistent with real-time controller implementation. A number of alternate approaches exist. This subsection discusses several of those techniques and compares their accuracy and computation times.

**Continuous Integration** The continuous integration method for getting the discrete input matrix  $\Gamma$  from time  $t_0$  to time  $t_1$  is

$$\Gamma_{\text{true}} = \int_{t_0}^{t_1} \left\{ D^{-1}(\mathbf{e}_d(t_1))\bar{\Phi}^*(\mathbf{e}_{md}(\tau), t_1, \tau)D(\mathbf{e}_d(\tau))M(\mathbf{e}_d(\tau)) \begin{bmatrix} 0_3 \\ I_3 \end{bmatrix} \right\} d\tau \quad (2.37)$$

where

$$M\mathbf{x} = \delta e_{\text{osc}} \quad (2.38)$$

and the analytic form of  $M$  can be found in Ref. [100]. The vector  $\mathbf{x}$  is in the LVLH coordinate system and has the form

$$\mathbf{x} = [x \ y \ z \ \dot{x} \ \dot{y} \ \dot{z}]^T \quad (2.39)$$

where the positions  $x$ ,  $y$ , and  $z$  are in meters and the velocities  $\dot{x}$ ,  $\dot{y}$ , and  $\dot{z}$  are in meters per second. This approach should use no additional linearization assumptions beyond those in Ref. [98], since the inputs and their coupling effects are incorporated continuously. While the outputs of the integration in Eq. (2.37) are very accurate, the approach itself requires significant computational effort (see Section 2.3.3).

**Discretized Integration** An approach to integrating  $\Gamma$  that is not as computationally intensive as the numerical integration is to approximate the integral in Eq. (2.37) discretely. This discrete approach introduces an additional timestep  $\Delta t$  which is the duration of each discrete term in the new approximate  $\Gamma$ . Conceptually, this approach is treating  $\Gamma$  as a series of smaller input effects, each based on a small time-invariant assumption. The discretized integration is

$$\Gamma_{\text{disc}} = \sum_{i=1}^n D^{-1}(\mathbf{e}_d(t_1)) \bar{\Phi}^*(\mathbf{e}_{md}(t_0+i\Delta t), t_1, t_0+i\Delta t) D(\mathbf{e}_d(t_0+i\Delta t)) M(\mathbf{e}_d(t_0+i\Delta t)) \begin{bmatrix} \frac{(\Delta t)^2}{2} I_3 \\ \Delta t I_3 \end{bmatrix} \quad (2.40)$$

where  $(n+1)\Delta t = t_1 - t_0$ . Here, a number of small double integrator assumptions are made, each one assuming that inputs of  $\Delta t$  seconds can safely ignore coupling effects.

**Rectilinear Dynamics Discretization** Another approach to finding  $\Gamma$  is to use the discrete input matrix from a set of rectilinear equations of motion and rotate it into relative orbital elements

$$\Gamma_{\text{rect}} = M(\mathbf{e}_d(t_0)) \Gamma_{\text{LVLH}} \quad (2.41)$$

where  $\Gamma_{\text{LVLH}}$  is the discrete input matrix for a set of rectilinear equations of motion (*e.g.*, inputs to a double integrator system, Hill’s equations, or Lawden’s equations). In Section 2.3.3, an LVLH-based version of the approximated  $\Gamma$  matrix for Lawden’s equations [101] is evaluated.

**GVE-based Discretization** An alternate approach to computing  $\Gamma$  is to use the continuous GVEs by taking the matrix exponential of the continuous matrix  $A^*$  from Eq. (2.7)

$$\Gamma_{\text{GVE}} = e^{A^*(t_1-t_0)}B(\mathbf{e}_d(t_0)) \quad (2.42)$$

where  $B$  is the GVE matrix. This approach assumes the effects of  $J_2$  on the input matrix are negligible.

**Validating  $\Gamma$**  The continuous integration computation of  $\Gamma$  in Eq. (2.37) should not require any additional validation beyond the verification that the linearization assumptions in the component matrices  $D$ ,  $\bar{\Phi}^*$ , and  $M$  are valid. To compare the matrices calculated using Eqs. (2.42), (2.40), and (2.41) their norm can be divided by that of the matrix generated using Eq. (2.37) ( $\Gamma_{\text{true}}$ ) to find the normalized error

$$\epsilon_{\text{disc}} = \frac{\|\Gamma_{\text{true}} - \Gamma_{\text{approx}}\|_2}{\|\Gamma_{\text{true}}\|_2} \quad (2.43)$$

where  $\Gamma_{\text{approx}}$  is the  $\Gamma$  matrix computed using one of the approximate methods. If the error  $\epsilon$  is kept sufficiently low (typical cutoff might be 0.01), then the approximate method would be considered valid. Figure 2-3 shows the values of  $\epsilon$  computed for the three approximate methods (the continuous integration method is taken as the true  $\Gamma$ ). Timestep increments are used in Figure 2-3, but an alternate validation method using true anomaly would be appropriate if steps of true anomaly are being used for plan implementation [25].

In Figure 2-3, “GVEs w/o  $J_2$ ” refers to the  $\epsilon$  for  $\Gamma_{\text{GVE}}$ , “Discrete Approximation (n=50)” refers to the  $\epsilon$  for  $\Gamma_{\text{disc}}$ , and “Lawden LTV Method” refers to the  $\epsilon$  for  $\Gamma_{\text{rect}}$ . The methods using Eqs. (2.41) and (2.42) are significantly more accurate than the



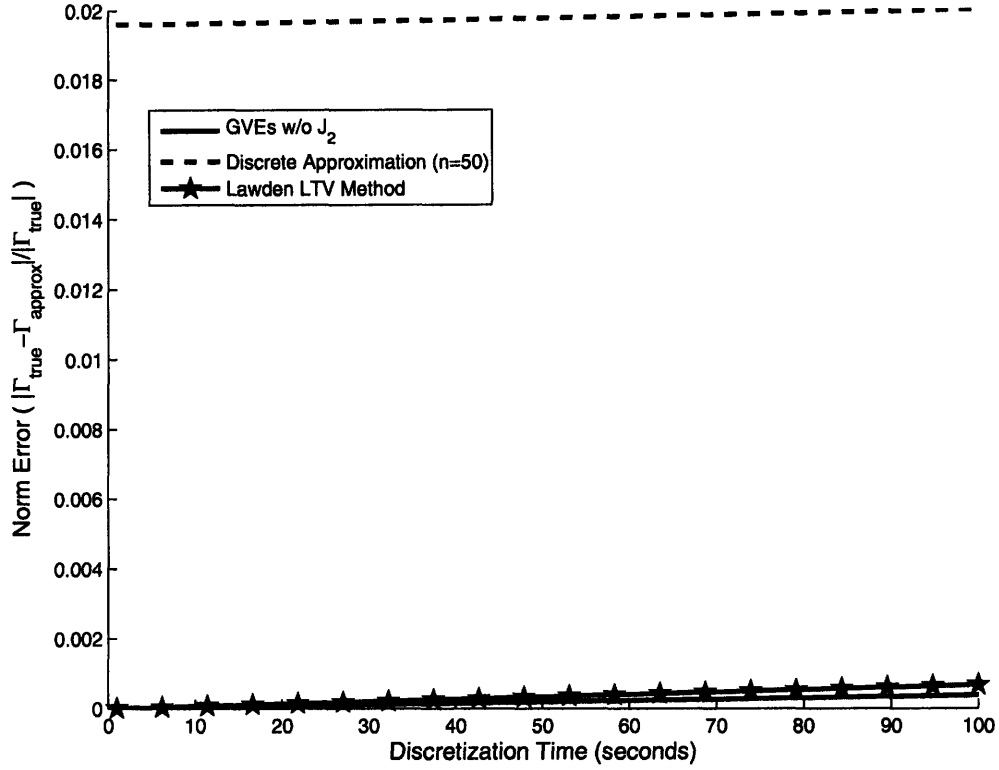


**Fig. 2-3:** Difference between integrated and approximated  $\Gamma$  for different discretization times using the LEO orbit in Eq. (2.14)

discrete approximation. This difference can be corrected by refining the discretization timestep, however, Table 2.1 shows that the discrete method using  $n = 50$  already requires more computation time to evaluate. Hence, in the LEO orbit examined, the GVE- and Lawden-based approximations are both faster to compute and more accurate than the discrete approximation method for all discretization times. Although the methods in Eqs. (2.41) and (2.42) are marginally less accurate than the continuous integration, they are, respectively, approximately 25 and 625 times as fast to compute.

Figure 2-4 shows how the evaluation of  $\Gamma$  using Eq. (2.42) degrades as the discretization time step is increased for the highly eccentric orbit ( $e \approx 0.8$ ) case examined in Section 2.2. In the figure,  $\Delta\Gamma$  refers to the difference between the  $\Gamma$ 's calculated using Eqs. (2.40), (2.41), and (2.42), respectively. For each time step, a series of  $\Delta\Gamma$  matrices are evaluated and the matrix with the largest induced 2-norm is used to rep-

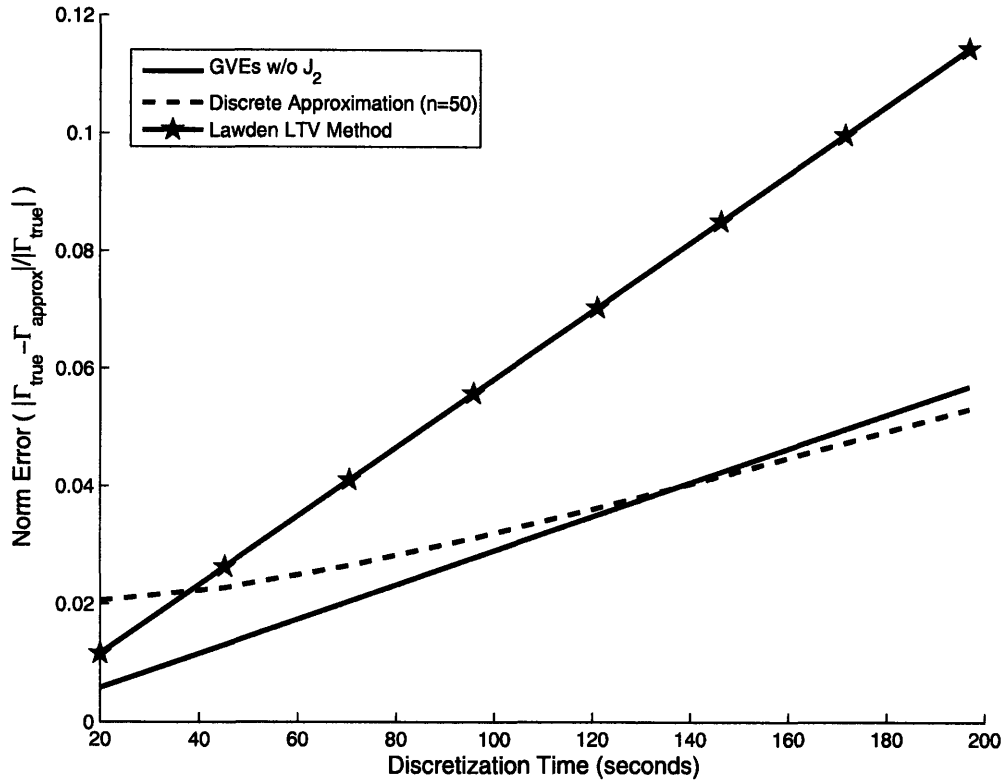


**Fig. 2-4:** Difference between integrated and approximated  $\Gamma$  for different discretization times using the HEO orbit in Eq. (2.16).

represent the discretization error. Figure 2-4 indicates that the 86 second time step used in the simulations in Section 2.6 is associated with just over 2% error between the  $\Gamma$  matrices for the GVE-based calculation method. As the timestep grows larger, the discrete approach to computing  $\Gamma$  becomes marginally better than the other methods, however it is still undesirable given that it is more than 250 times slower to compute than the method in Eq. (2.42).

## 2.4 Model Predictive Control Using GVEs

Reference [84] showed that given a valid set of linearized dynamics and a desired trajectory, a model predictive controller for a spacecraft formation can be designed that allows for arbitrarily many convex terminal and intermediate state conditions, as well as sensor noise robustness requirements. This controller is implemented on

**Table 2.1:** Average durations (in seconds) required to compute  $\Gamma$  matrices using various methods

Calculation Method	Average Computation Time
$\Gamma_{\text{true}}$	1.02 sec
$\Gamma_{\text{disc}} (n=50)$	0.42 sec
$\Gamma_{\text{rect}}$	0.041 sec
$\Gamma_{\text{GVE}}$	0.0016 sec

each spacecraft in the formation and it is using a linear programming formulation. The general form of the optimization performed by the controller is

$$\min \|U\|_1 \quad \text{subject to} \quad \mathbf{A}U \leq \mathbf{b} \quad (2.44)$$

where the matrix  $\mathbf{A}$  and the vector  $\mathbf{b}$  are formed based on the input dynamics and problem constraints and  $U$  is a vector of potential control inputs vectors

$$U = \left[ \mathbf{u}_i(1)^T \quad \mathbf{u}_i(2)^T \quad \dots \quad \mathbf{u}_i(n-1)^T \quad \mathbf{u}_i(n)^T \right]^T \quad (2.45)$$

where each vector  $\mathbf{u}_i(k)^T$  is the input for spacecraft  $i$  at step  $k$  for an  $n$  step plan.

In order to use the linearized GVE-based dynamics developed in Eq. (2.12) in the MPC formulation, the dynamics can be discretized using a zero order hold assumption according to the procedure described in Ref. [102]. To use the linearized  $J_2$ -modified GVE-based dynamics developed in Eq. (2.31) in the MPC formulation, the discrete dynamics in Eq. (2.36) are used. Solutions to the optimization posed in Eq. (2.44) usually take the form of classical “bang-off-bang” optimal control laws. Figure 2-5 shows a typical plan to correct a small orbital element error. Note that although only two elements begin with errors, the optimized solution requires some elements to deviate from their desired states in order to minimize overall fuel use.

Solving the optimization in Eq. (2.44) with 1000 discretization steps and a terminal constraint has always required less than 0.05 seconds on a 3 GHz computer. Formulating the matrices used in the optimization has always taken under 10 seconds,

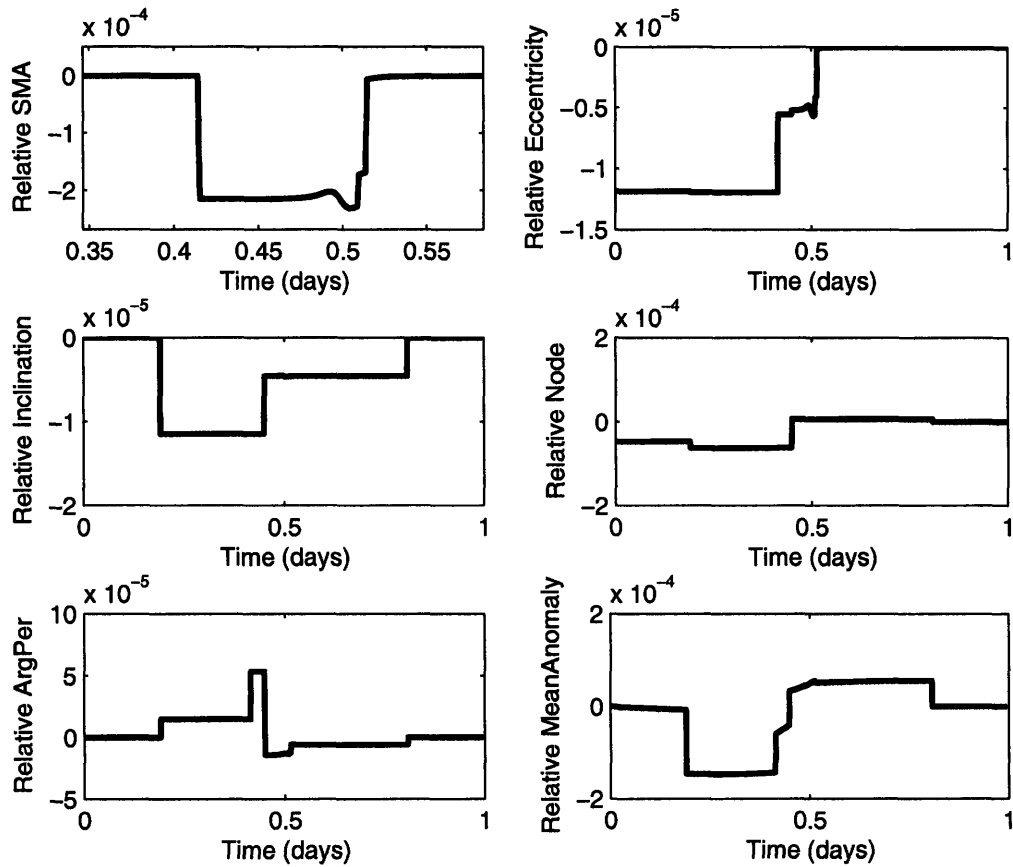


**Fig. 2-5:** Example of a plan generated to MPC with  $J_2$ -modified GVEs (lines indicate relative state error)

far less than the 86 second discretization time step. The time required to formulate the problem will increase as the discretization step is made smaller and additional constraints are added. Although the computation numbers are very small, a more complicated formulation could still be implemented in a real-time system by specifying that thrusting not begin for several time steps into the plan. This will result in a plan that does not require action until some specified time in the future when it is certain that the formulation and optimization will have been completed.

Figure 2-6 shows the error between a planned trajectory using the HEO orbit and the actual implemented trajectory when a trajectory is implemented without replanning (*i.e.*, open-loop). The norm of the final error vector is  $\|\zeta\|_2 \approx 1.236 \times 10^{-5}$ , which is significantly below  $3.66 \times 10^{-3}$ , the maximum norm of acceptable linearization error for this orbit, which was determined in Section 2.2. Thus, it is valid to use the

same linearized dynamics and controller to create a new plan from this terminal position. Repeatedly implementing new plans from a given initial error within the valid linearization range has always yielded terminal errors that were smaller and, hence, valid as initial conditions for replanning.

### **2.4.1 Error-Box Constraints Using Relative Orbital Elements**

Several approaches have been developed to specify formation-flying mission performance constraints. Generally, the goal of formation-flying control is to keep the formation from “drifting apart” and to maintain some relative geometry. This requirement has been translated into maintaining orbits that have the same period and specifying desired relative states for spacecraft to follow. Both goals can be accomplished simultaneously by specifying relative desired points that have identical periodicity. Then to ensure that the spacecraft do not drift and that the formation geometry is maintained adequately, the control objective is to keep the spacecraft within some region around its desired point. This region is defined as a dead-band in Ref. [103] and similarly as an error box in Ref. [84].

Maintaining a spacecraft within an error box has several advantages over tracking a desired point: it does not require fuel be used to correct minor deviations from the desired orbit, it better captures mission constraints which typically only require satellites to be in desired positions within some acceptable error, and it allows “breathing room” for the controller to account for modeling errors. In addition, the method of planning based on GVEs proposed in Section 2.4 relies on the validity of the linearization analyzed in Section 2.3, which degrades as the difference between the actual orbital element state and the orbital element state that has been linearized increases. If the error box used for a particular mission is smaller than the linearity range, which it typically would be (see Section 2.2), the constraint that the spacecraft remain in the box provides an additional means of verifying that the linearity assumptions will be satisfied.

Several approaches can be taken to create an error box. Position error boxes are demonstrated in Ref. [84], which is a convenient bounding mechanism for a formation

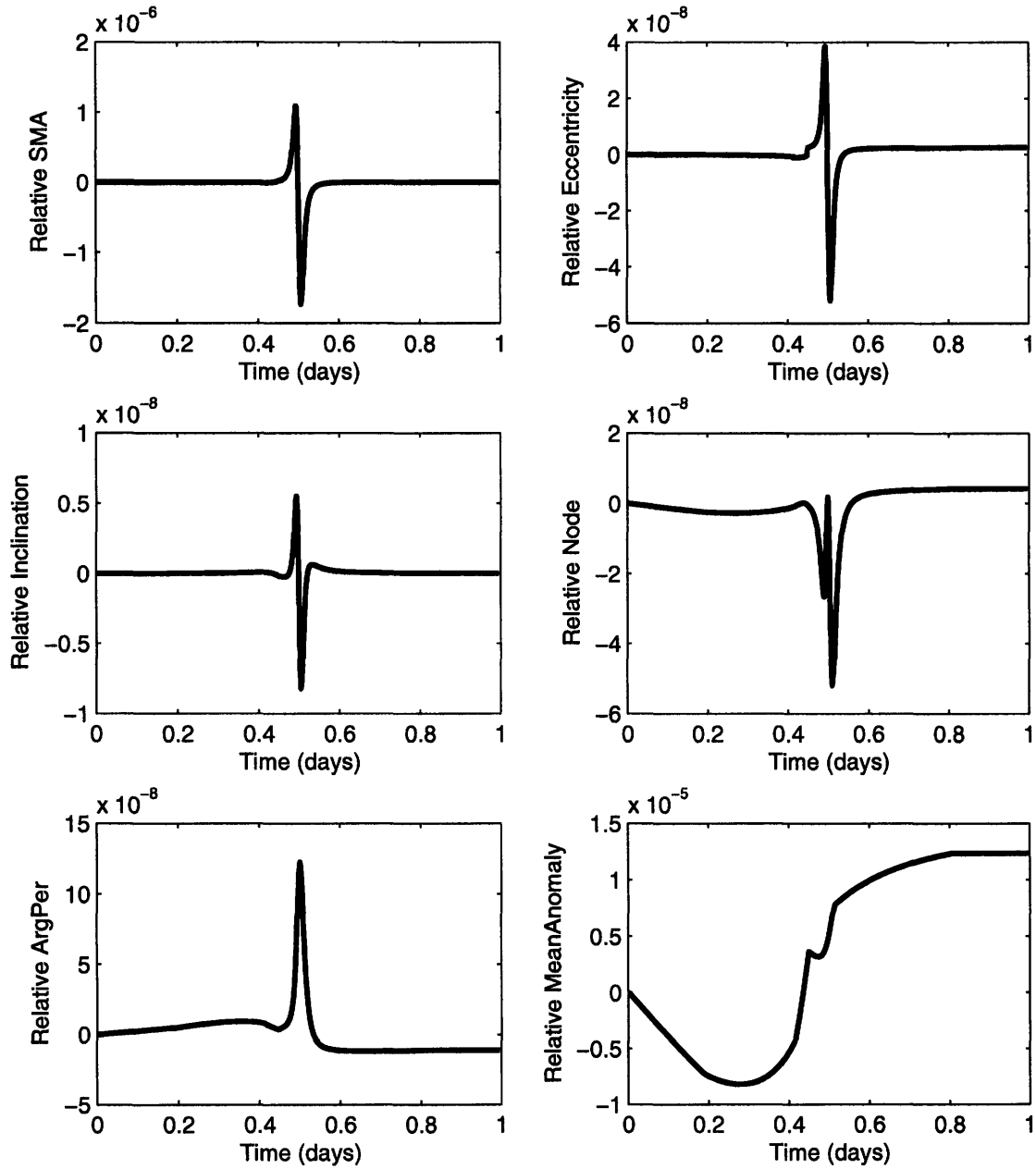


**Fig. 2-6:** Error in open-loop trajectory following using the HEO orbit example. Lines indicate the difference between planned and implemented trajectories in a fully nonlinear simulation.

flying mission because it coincides well with science requirements on the accuracy of the formation geometry shape. When the formation geometry is specified in orbital elements, it is most convenient to use a six dimensional error box with bounds on each of the state elements. This approach, while simple and convenient for enforcing acceptable relative drift levels, does not map well into the position error box constraints typical of previous performance specifications. To transition between LVLH error states,  $\mathbf{x}$ , and relative orbital element error states,  $\zeta$ , a first order rotation matrix  $M(\mathbf{e}_d)$  is used (see Eq. (2.38)). It is possible to enforce relative position and relative velocity error box constraints using the  $M(\mathbf{e}_d)$  matrix by formulating the optimization problem in Eq. (2.44) with constraints at every step  $k$  where it is desired that the spacecraft remain inside an error box

$$\mathbf{x}_{\min} \leq M^{-1}(\mathbf{e}_d)\zeta \leq \mathbf{x}_{\max} \quad (2.46)$$

where  $\mathbf{x}_{\max}$  and  $\mathbf{x}_{\min}$  denote opposing corners of the error box. To exclusively enforce a partial state error box (*e.g.*, a position box),  $M(\mathbf{e}_d)$  can be premultiplied by an additional matrix  $H$  in Eq. (2.46) to only retain the desired components of the state.

## 2.4.2 Formation Flying: Coordination Using GVEs

The model predictive controller described in Section 2.4 is designed to be decentralized, with a fully independent controller being run on each spacecraft. The controller designs trajectories that will keep a spacecraft  $i$  inside an error box centered about the spacecraft's desired orbit,  $\mathbf{e}_{di}$ . In Section 2.2, the desired orbits are defined with respect to the actual orbit of an arbitrary satellite in the formation,  $\mathbf{e}_1$ , using differential orbital element vectors,  $\delta\mathbf{e}_{di}$ , in the same manner used in Ref. [100]. In a system where initial conditions are chosen infrequently, it may be desirable to introduce additional coordination into the formation. When spacecraft each track desired states with no coordination, the control task is referred to as *formation-keeping* [84]. Alternately, *formation flying* occurs when the spacecraft controllers collaborate to achieve formation-wide fuel minimization. This coordination can be achieved by calculating

a central point that minimizes the overall weighted state error of each spacecraft in the formation. Approaches to implementing closed-loop coordination of this type are presented in Refs. [97] and [104]. The *virtual center* approach in Ref. [97] is a centralized calculation of the error-minimizing center based on fuel-weighting and derived from measurements available through carrier-phase differential GPS (CDGPS) relative navigation of the type described in Ref. [105]. An equivalent approach can be used to find an error-minimizing reference orbit for a formation described in differential orbital elements.

Measurements from a CDGPS relative navigation system are assumed to be in the form of relative LVLH states [105],  $\mathbf{x}_i$  (see Eq. (2.39)), for each satellite in the formation. The measurements will be relative to an arbitrary absolute satellite state,  $\mathbf{e}_1$ , in the formation, which is assumed to be at the origin of the LVLH frame. In addition to relative states, the GPS sensors on each satellite can be expected to compute a less accurate estimate of the spacecraft's absolute state. Given an estimate of the absolute state in Earth Centered Inertial (ECI) coordinates,  $\mathbf{X}_{\text{ECI}_1}$  and the relative states  $\mathbf{x}_i$ , the differential states  $\delta\mathbf{e}_i$  in Eq. (2.3) can be computed in several ways. The matrix  $M(\mathbf{e}_1)$  in Eq. (2.38) could be computed and used to create a first order approximation of the relative differential element states. However, an exact conversion can be calculated by forming estimates of the absolute states of each of the satellites based on their relative measurements

$$\mathbf{X}_{\text{ECI}_i} = \mathbf{X}_{\text{ECI}_1} + \mathbf{x}_i \quad (2.47)$$

The absolute states  $\mathbf{X}_{\text{ECI}_i}$  can be converted to Keplerian orbital elements,  $\mathbf{e}_i$ , of each satellite using a well-known procedure described in Ref. [106]. The relative measurements are then recovered in terms of differential orbital elements,  $\delta\mathbf{e}_i$ , using Eq. (2.3). Desired differential elements,  $\delta\mathbf{e}_{dci}$ , are then specified with respect to an unknown virtual center state,  $\delta\mathbf{e}_c$ , which is specified with respect to the absolute state



$\mathbf{e}_1$ . The error of spacecraft  $i$  with respect to the virtual center,  $\zeta_{ci}$ , is given by [97]

$$\mathbf{e}_i - \delta\mathbf{e}_{dci} - \delta\mathbf{e}_c = \zeta_{ci} \quad (2.48)$$

which can be placed in the standard least squares form  $b_i - C_i\delta\mathbf{e}_c = \zeta_{ci}$ , where  $b_i = \mathbf{e}_i - \delta\mathbf{e}_{dci}$ ,  $C_i$  is a  $6 \times 6$  identity matrix, and  $\delta\mathbf{e}_c$  denotes the location of the virtual center with respect to  $\mathbf{e}_1$  in differential orbital elements. By concatenating the  $b_i$ ,  $C_i$ , and  $\zeta_{ci}$  vectors for each spacecraft, the statement of error for the entire formation is written  $b - C\delta\mathbf{e}_c = \zeta$ , where  $b = [b_1 \dots b_n]^T$ ,  $C = [C_1 \dots C_n]^T$ , and  $\zeta = [\zeta_{c1} \dots \zeta_{cn}]^T$ . The solution that minimizes the error vectors globally in a weighted least squares sense is

$$\delta\mathbf{e}_c = (C^T W C)^{-1} C^T W b \quad (2.49)$$

where  $W$  is a weighting matrix that can be used to bias the center location according to the fuel-use rates of different satellites in the formation, as well as to weight orbital elements individually based upon the amount of control required to alter them (obtainable from the GVEs for  $\mathbf{e}_1$ ). This calculation can be decentralized and reduces the following iterative form[96]

$$\delta\mathbf{e}_{c1} = b_1, \quad \delta\mathbf{e}_{ci} = \delta\mathbf{e}_{c_{i-1}} + \frac{w_i}{\bar{w}_{i-1} + w_i} (b_i - \delta\mathbf{e}_{c_{i-1}}) \quad (2.50)$$

where  $w_i$  is the weight of the  $i^{th}$  estimate, and  $\bar{w}_i = w_1 + w_2 + \dots + w_i$ . In this formulation, a spacecraft  $i$  must pass its current state estimate,  $\delta\mathbf{e}_{c_i}$ , and the scalar  $\bar{w}_i$  to the next spacecraft for a new estimate of the optimal center position to be formed. Using this method, the error-minimizing fuel-weighted virtual center can be known in one full cycle around a formation.

## 2.5 Comparison to Other GVE-based Impulsive Control Schemes

The optimized controller developed in Section 2.4 can be applied to a range of spacecraft control problems. This section uses that controller for the specific problem of correcting state error over a finite horizon in order to compare its performance and capabilities with other methods. Gauss' Variational Equations (GVEs) have been used to design many Lyapunov and fixed impulse control systems [90, 91, 93, 94, 99]. Several research groups have proposed control laws for formation-flying spacecraft that use GVEs to design impulsive thrusting maneuvers for orbit correction. A method of producing optimized impulsive plans for very-low eccentricity orbits is presented in Ref. [107], but this approach does not extend to the higher eccentricities required for MMS missions. Another method based on GVEs [94] allows optimized planning for low Earth orbits, but only permits optimization over a single impulsive thrust, guaranteeing that the solution will be sub-optimal in many cases. In addition, this approach is only derived for correcting errors in semimajor axis, eccentricity, and inclination. Another approach to using GVEs for formation control is to derive a continuous proportional-derivative controller satisfying a Lyapunov equation [90–92, 100]. Control algorithms of this type have been shown to be asymptotically stable in most cases [92], but belong to a class of control systems that fire continuously. Continuous firing is generally not desirable for space missions because it is often disruptive to the science mission, it typically must be coupled with attitude maneuvers, and it expends fuel (nonreplenishable aboard a spacecraft) continuously.

The method of formation control in Ref. [94] is based on GVEs and uses a single corrective thrust computed using a nonlinear optimization. Although this method is guaranteed to find the optimal single-thrust correction for an arbitrary time period, it is not guaranteed (or likely) to find the optimal multiple-thrust correction. In addition, this approach is restricted to use in low Earth orbits and is only designed to correct errors in semimajor axis, eccentricity, and inclination. An approach presented in Ref. [108] uses a pseudo-inverse to the GVE control effect matrix to calculate a

single corrective impulse. This approach is not guaranteed to be fuel-optimal for any cases and is not accurate for correcting position errors

Ref. [93] describes a controller which uses four impulses over the course of an orbit to correct arbitrary orbital element perturbations. Because of its more general applicability, this section will compare that approach to the MPC controller presented in Section 2.4. Both methods are designed to drive the elements of a state error  $\zeta$  to zero over a fixed time interval. The four-impulse approach has not been presented in the context of performance criteria (*e.g.*, trajectory or terminal error boxes, robustness to disturbances) or constraints (*e.g.*, maximum thrust level), so the comparisons in this section will use an MPC controller formulation that minimizes fuel use while driving the error state to zero in a fixed time and has no other constraints. In addition, for the purposes of comparison, no  $J_2$  effects are used in either planning approach.

The algorithm in Ref. [93] can be summarized in four steps to be taken over the course of an orbit. When the argument of latitude,  $\theta$ , is 0 or  $\pi$  radians, implement a velocity change (impulsive thrust),  $\Delta v_{h_i} = [h/(r \cos \theta)]\Delta i$ , in the cross-track direction of an LVLH frame centered on the spacecraft to cancel the inclination error component of  $\zeta$ . When the argument of latitude,  $\theta$ , is  $\pi/2$  radians, implement a velocity change,  $\Delta v_{h_\Omega} = [h \sin i/(r \sin \theta)]\Delta \Omega$  in the cross-track direction to cancel the ascending node error. At perigee and apogee, implement  $\Delta v_{r_p}$  and  $\Delta v_{r_a}$ , respectively, in the radial direction to cancel the argument of perigee and mean anomaly errors

$$\Delta v_{r_p} = -\frac{na}{4} \left( \frac{(1+e)^2}{\eta} (\Delta\omega + \Delta\Omega \cos i) + \Delta M \right) \quad (2.51)$$

$$\Delta v_{r_a} = \frac{na}{4} \left( \frac{(1-e)^2}{\eta} (\Delta\omega + \Delta\Omega \cos i) + \Delta M \right) \quad (2.52)$$

Also at perigee implement  $\Delta v_{\theta_p}$  and at apogee implement  $\Delta v_{\theta_a}$  in the in-track direction, to cancel the semimajor axis and eccentricity errors

$$\Delta v_{\theta_p} = \frac{na\eta}{4} \left( \frac{\Delta a}{a} + \frac{\Delta e}{1+e} \right) \quad (2.53)$$

$$\Delta v_{\theta_a} = \frac{na\eta}{4} \left( \frac{\Delta a}{a} - \frac{\Delta e}{1-e} \right) \quad (2.54)$$

Using the notation and the HEO reference orbit from Section 2.2, the following example compares the MPC method with the control approach reviewed in this section. Note that in comparison to the MPC approach, the four impulse method is very simple to implement. However, the two approaches have different rates of fuel use for identical tasks. For the state error

$$\zeta = \left( 10^{-9} \quad 10^{-7} \quad 10^{-7} \quad 10^{-7} \quad 10^{-7} \quad 10^{-7} \right)^T \quad (2.55)$$

the 4-impulse method requires 1.42 mm/s of fuel to correct the state error over the course of an orbit and the MPC method requires 0.549 mm/s of fuel. In this example, the model predictive controller was given a full orbit time horizon. However, the same control objective could have been achieved in less time, but using more fuel.

A series of 1000 orbital element state error vectors,  $\zeta$ , were generated in which each perturbed element was a random number between  $\pm 10^{-6}$ . For each of the error vectors, both control methods were used to generate plans for eliminating the error. On average, the MPC maneuvers only required 51% of the fuel required by the 4-impulse maneuver. Further controller comparisons are presented in Section 2.6.

## 2.6 Formation Maintenance on MMS-like Mission

The control system described in Section 2.4 was demonstrated on a segment of a mission similar to MMS, which is comprised of four spacecraft that create a regular tetrahedron geometry once per orbit near apogee to perform science observations. The orbits of the four spacecraft are widely separated and highly elliptical, presenting a challenge for many optimal formation specification and control approaches in the literature [25, 109]. Using the tetrahedron initial-condition optimization approach in Ref. [96] and the model predictive approach in Section 2.4, the four spacecraft were controlled in a fully nonlinear simulation with Earth oblateness effects, atmospheric drag effects, and other realistic disturbances using a commercial orbit propagator [112]. The control objective in this simulation is to achieve a set of tetrahedron

initial conditions once per day near the formation orbit apogee. The reference orbit for formation is the highly eccentric orbit used in Example 2 of Section 2.2.

In order to implement the MPC scheme in Section 2.4 using the dynamics developed in Section 2.3, the approximate rectilinear method of calculating  $\Gamma$  is used. The dynamics matrices  $\Gamma$ ,  $\bar{\Phi}$ , and  $D$  are all functions of the desired orbital elements, which are parameter-varying. To obtain accurate trajectories for the absolute desired orbital elements for the formation, they are integrated numerically with  $J_2$  disturbance effects included and then used to generate the linear propagation matrices used in the optimization. The time step used in the simulation is 86 seconds, providing approximately 1000 discretization points in each daylong orbit. Constant time step duration was chosen to approximate typical flight computer operation, but plans with varying time steps can also be designed by planning in increments of true anomaly, and Ref. [25] discusses how these can be implemented. The planning horizon length for this simulation is one full day.

Figure 2-7 shows the rate at which fuel was used over the course of one week of formation flying. The formation fuel use rate converges to approximately 12.1 mm/s per day ( $\approx 1$  orbit) for each satellite. Note that all previous simulations had to be limited to the case where the  $J_2$  effects were disabled in order to ensure that the formation remained stable. In that case, for the same configuration, but without the effects of  $J_2$  included in the controller dynamics or the simulation dynamics, the results showed an average  $\Delta V$  of 11.5 mm/s per satellite per orbit. These nearly equivalent fuel use rates for simulations with and without  $J_2$  indicate that linearized modeling of  $J_2$  effects in a controller of the type presented in Section 2.4 is sufficient to prevent the disturbances from dominating fuel usage. The state error for one of the spacecraft in the formation is seen being driven to the origin in Figure 2.6. Trajectories followed during this simulation fall within the range of acceptable state error determined for the linearizing assumptions used in Section 2.3.

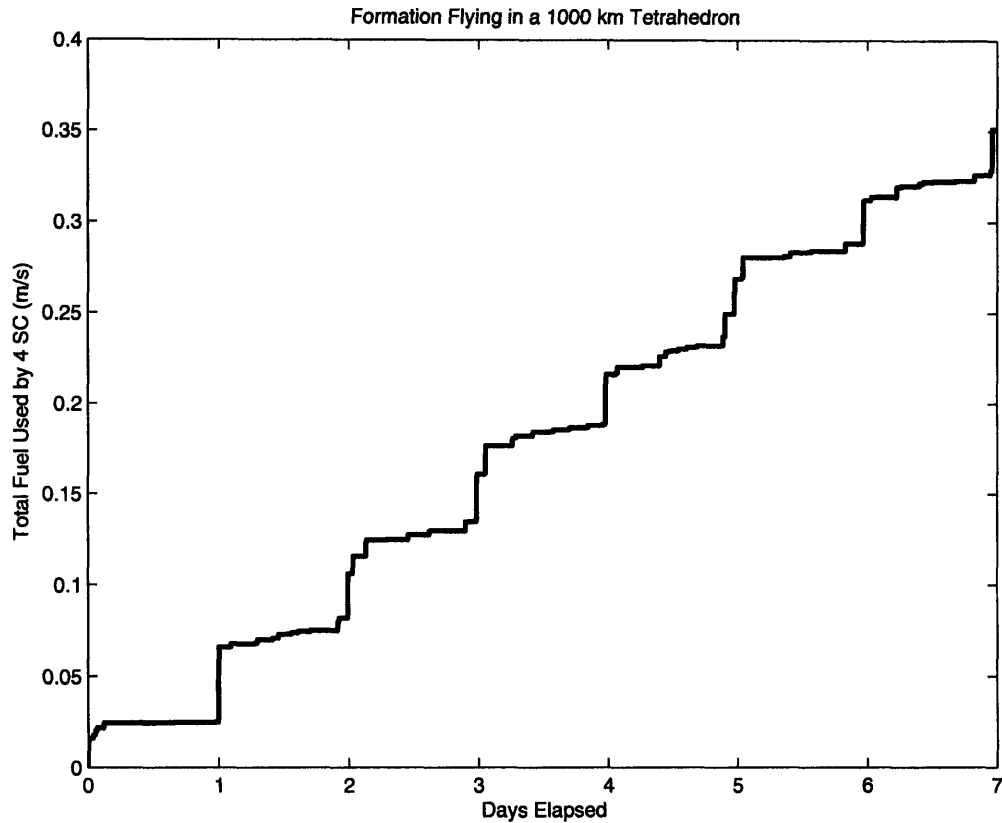
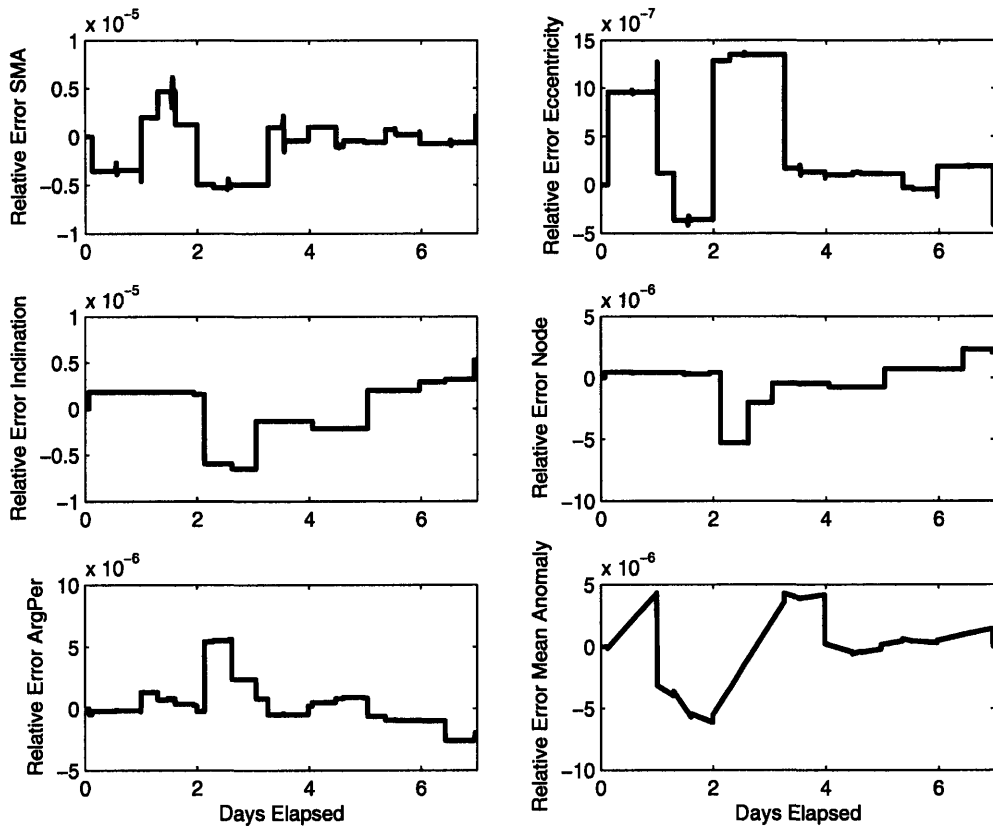


Fig. 2-7: Forming and maintaining a 1000 km (at apogee) tetrahedron formation in a highly eccentric orbit ( $e \approx 0.8$ ) in the presence of  $J_2$

## 2.7 Summary

A variant of Gauss' Variational Equations that incorporates the effects of  $J_2$  was used to derive a set of linearized relative dynamics of orbital motion and extend previous work on planning-based controllers. This choice of a linear parameter varying (LPV) dynamics model to design the controller allows a compromise between simple, but inaccurate, linear models (e.g., Hill's equations) and high fidelity, but often difficult to control, nonlinear models. In particular, by accounting for  $J_2$  disturbances in the dynamics, the planning controller can exploit these dynamics for improved fuel efficiency. The linearization assumptions used in the approach were shown to be valid for typical spacecraft error box sizes. The LPV model was used in a model predictive controller (MPC) and the combination was shown to be more fuel-efficient than a previously published technique. The overall controller ( $J_2$ -modified GVE-based



**Fig. 2-8:** Forming and maintaining a 1000 km (at apogee) tetrahedron formation in a highly eccentric orbit ( $e \approx 0.8$ ) in the presence of  $J_2$

dynamics embedded in the MPC controller) was also used to specify and control a large (1000 km sides at apogee) tetrahedron-shaped formation in an MMS-like orbit for a period of twenty days using a commercial propagator with realistic disturbances. The results showed that the controller is reliable and that formation flying using this MPC with  $J_2$ -modified GVEs requires fuel use that is comparable to using unmodified GVEs in simulations that do not include the  $J_2$  effects.





## Chapter 3

# Fuel-optimized Semi- $J_2$ -invariant Initial Conditions

Section 2.4 presented a model predictive controller that can be used to create optimized plans for relative orbit control in the presence of  $J_2$  disturbances. In a spacecraft formation, it is critically important both to conserve fuel when maneuvering and to maneuver to a state that will, over time, conserve fuel. The latter is an initial condition (IC) problem, the specifications of which will depend on the unique requirements of a particular mission. However, in any spacecraft formation, a primary goal will be to prevent the vehicles from drifting apart, since that will typically end the mission. If the spacecraft in a formation tend to drift apart, then periodic maintenance maneuvers will be required to restore the formation. Initial conditions are called *invariant* if they eliminate drift, thereby allowing spacecraft to maintain their relative orbits without expending fuel. In the context of this thesis, invariance does not necessarily imply any form of relative boundedness at other points along the reference orbit, but this could be addressed by including additional error box constraints to the optimization developed in this section.

For purely Keplerian orbits, invariance translates into a requirement that all spacecraft in a formation have the same semimajor axis. For example, this requirement was solved for analytically using Lawden's equations of motion in Ref. [109]. However, Earth oblateness effects ( $J_2$ ) make orbits based on the Keplerian invariance solution

drift apart. In fact, when the effects of  $J_2$  are considered, very few perfectly invariant orbits exist. Hence, it is more common for a  $J_2$  “invariant” orbit to instead be truly invariant only in several dimensions where it is possible to cancel the relative effects of  $J_2$ . Analytic conditions based on this partial invariance have been introduced [20, 110]. The following presents an alternate approach that uses the dynamics in Section 2.2 and Ref. [98] in a convex linear optimization to find initial conditions that balance the objective of not drifting in the presence of relative  $J_2$  effects against the objectives of minimizing the fuel use required to achieve these initial conditions and retaining a specified geometry for the formation.

### 3.1 Formulation

To begin, specify that orbits are invariant if their relative orbital offset,  $\delta\mathbf{e}$ , in Eq. (2.5) remains unchanged over a period of time, so that  $\delta\mathbf{e}(t_1) \equiv \delta\mathbf{e}(t_2)$ , where  $t_2 - t_1$  is the duration of interest (typically an integer number of orbits). Then, using the state transition matrix from Eq. (2.34) gives the constraint

$$\delta\mathbf{e}(t_1) = \delta\mathbf{e}(t_2) = D^{-1}(\mathbf{e}(t_2))\bar{\Phi}^*(\mathbf{e}(t_1), t_2, t_1)D(\mathbf{e}(t_1))\delta\mathbf{e}(t_1) \quad (3.1)$$

Defining the matrix function  $\bar{\Phi}_{Dk}^* \equiv D^{-1}(\mathbf{e}(t_{k+1}))\bar{\Phi}^*(\mathbf{e}(t_k), t_{k+1}, t_k)D(\mathbf{e}(t_k))$  gives the invariance condition

$$\delta\mathbf{e}(t_1) = \bar{\Phi}_{D1}^*\delta\mathbf{e}(t_1) \rightarrow (\bar{\Phi}_{D1}^* - I)\delta\mathbf{e}(t_1) = 0 \quad (3.2)$$

where  $I$  is a  $6 \times 6$  identity matrix. As mentioned above, the resulting geometry of the no-drift (complete invariance) condition is too restrictive for many missions, but partially invariant conditions can be obtained by minimizing the weighted norm of the invariance condition

$$\min_{\delta\mathbf{e}(t_1)} \|W_d(\bar{\Phi}_{D1}^* - I)\delta\mathbf{e}(t_1)\| \quad (3.3)$$

where the weighting matrix  $W_d$  is introduced to extract states of interest to penalize particular types of drift. Note that if  $W_d$  is the matrix  $M(\mathbf{e}(t))$  (see Eq. (2.37)), which rotates the differential osculating elements  $\delta\mathbf{e}$  into an LVLH frame, then the elements of the LVLH state can be directly penalized (*e.g.*, extracting only position states could penalize meters of drift). This enables the drift formulation to penalize the distance from the desired geometry in a Cartesian frame, as opposed to just using orbital elements. Penalizing true separation distance finds initial conditions that will maintain the formation shape, an important consideration for missions that require specific geometric configurations [86].

The overall problem statement then is, given a spacecraft at offset  $\delta\mathbf{e}(t_0)$ , design a control input sequence  $U(\tau)$ ,  $\tau \in [t_0, t_1]$  that generates a set of initial conditions at  $t_1$  that balances the trade-off between the ensuing drift by time  $t_2$ , the fuel cost of achieving these initial conditions, and the extent to which the formation geometry is maintained. The proposed approach is illustrated in Figure 3-1. The two diagrams in Figure 3-1 show local frame views of relative orbital motion. One satellite is fixed at the origin and the other (represented as a circle) is shown at several different times. On the left, the satellite is pictured at some initial time  $t_0$  and again after some maneuver at time  $t_1$ . The open loop propagation of the satellite from  $t_0$  to  $t_1$  that would occur absent the maneuver is also shown (hatched circle). The right figure shows the drift that would occur starting from each state at  $t_1$ . The case state at  $t_1$  after a maneuver experiences less drift than the open-loop case, but it required more fuel. Also, the dashed lines show the geometry cost of moving the satellite away from the desired initial conditions. Thus, the three times in the problem are  $t_0$ , when the maneuver is initiated and fuel is penalized,  $t_1$  when the geometry cost is penalized, and  $t_2$  when drift is penalized. The semi-invariant initial condition optimization cost function is

$$C^* = \min_U \{Q_d \|W_d(\bar{\Phi}_{D1}^* - I)(\bar{\Phi}_{D0}^* \delta\mathbf{e}(t_0) + \hat{\Gamma}U)\| + Q_x \|W_x \hat{\Gamma}U\| + Q_u \|U\|\} \quad (3.4)$$

where  $C^*$  is the optimal cost,  $W_x$  is a weighting matrix to specify the type of geometry

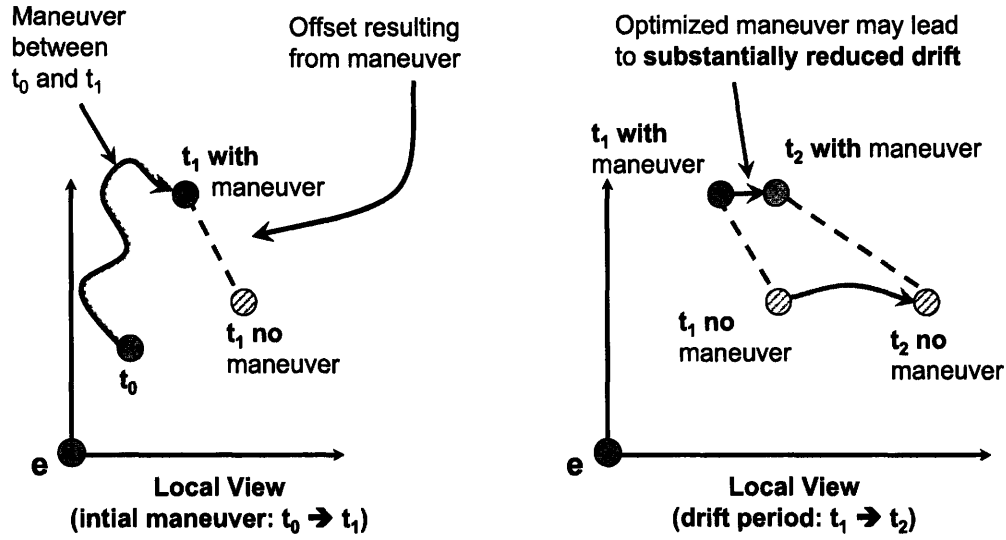
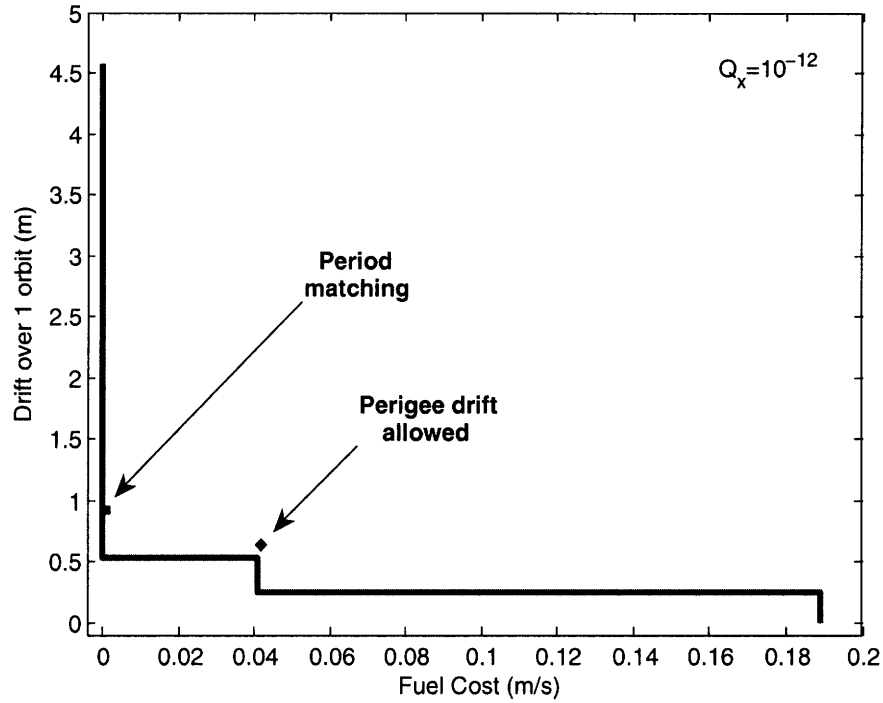


Fig. 3-1: Illustration of Initialization Approach

penalty,  $Q_u$  is a weighting on fuel minimization,  $Q_x$  is a weighting on desired formation geometry, and  $Q_d$  is a weighting on drift. Using Eq. (3.1),  $\delta \mathbf{e}(t_1) = \bar{\Phi}_{D_0}^* \delta \mathbf{e}(t_0) + \hat{\Gamma} U$ , where  $\hat{\Gamma}$  is a row of convolved  $\Gamma$  matrices (see Eq. (2.35)) that propagate the effects of a vector of inputs ( $U$ ) (see Eq. (2.45)) at each time step of the maneuver [84]

$$\hat{\Gamma} = \begin{bmatrix} \tilde{\Phi}(n, 1) \tilde{\Gamma}(0) & \tilde{\Phi}(n, 2) \tilde{\Gamma}(1) & \cdots & \tilde{\Phi}(n, n-1) \tilde{\Gamma}(n-2) & \tilde{\Gamma}(n-1) \end{bmatrix} \quad (3.5)$$

where  $\tilde{\Phi}(k, j) \equiv D^{-1}(\mathbf{e}(kt_s)) \bar{\Phi}^*(\mathbf{e}, kt_s, jt_s) D(\mathbf{e}(jt_s))$ ,  $\tilde{\Gamma}(k) \equiv \Gamma(\mathbf{e}, (k+1)t_s, kt_s)$ , and  $t_s$  is the discretization time step. The cost function uses the initial state of each spacecraft in the formation as the desired geometry, so the geometry weighting penalizes deviations from the open-loop state propagation. Note that a simple modification to the cost function could separate the initial geometry from the desired geometry. The optimization in Eq. (5.6) can be easily implemented as a linear program if 1-norms are used, permitting efficient, fast online solutions [111]. As expected, a sufficiently high weighting on invariance results in a minimizing control input  $U^*$  where  $\hat{\Gamma} U^* = -\bar{\Phi}_{D_0}^* \delta \mathbf{e}(t_0)$ . Alternately, a sufficiently high  $Q_x$  (with an identity matrix for  $W_x$ ) results in  $\hat{\Gamma} U^* = [0 \ 0 \ 0 \ 0 \ 0 \ 0]^T$ , because the inputs will all be zero in order to maintain the original geometry.



**Fig. 3-2:** Expected drift and fuel cost of a range of optimized initial conditions in a LEO orbit. The lines between marked points indicate the least drift that can be attained for the indicated amount of fuel. In this example the fuel weighting is 1, the geometry weighting is  $10^{-18}$ , and the drift weighting is allowed to vary widely. The  $\blacksquare$  represents the solution based on the period-matching condition in Case 1 of Ref. [110]. The  $\blacklozenge$  represents the solution based on the  $J_2$  invariant orbit with perigee drift in Ref. [20].

## 3.2 Results

Figure 3-2 shows drift rates and fuel costs for a series of initial conditions generated by the optimization method with a half orbit planning horizon as  $Q_d$  is changed. For this example, the 1-norm is used to penalize both drift and fuel use and both  $W_d$  and  $W_x$  are set to the position rows of  $M$  in order to only penalize position drift and geometry separation. With a very low  $Q_d$ ,  $Q_u$  will dominate, resulting in no control use. The zero drift point corresponds to high fuel use, because it necessitates driving the spacecraft to nearly the same orbits. A range of possible optimized initial conditions lie in between those extrema. The high-drift, unmodified initial conditions lie very close to the vertical drift axis, but drop to just over 0.5m of drift with a minimum of fuel use. Further drift reductions are possible, but at greater fuel cost. It

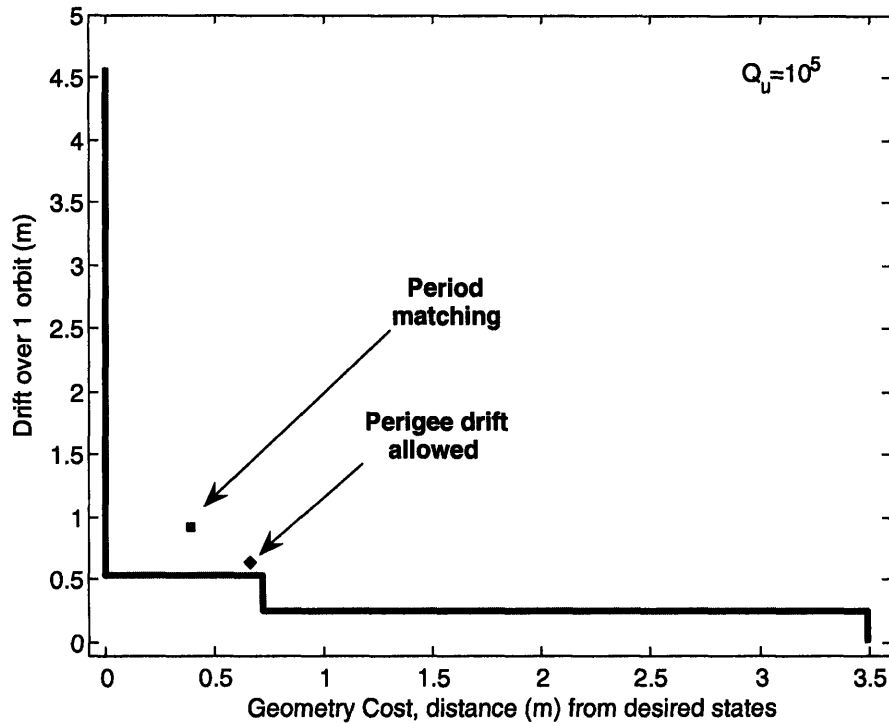


**Fig. 3-3:** Expected drift and geometry cost of a range of optimized initial conditions in a LEO orbit. The lines between marked points indicate the least drift that can be attained for the indicated amount of separation from the desired orbital offset. The ■ represents the solution based on the period-matching condition in Case 1 of Ref. [110]. The ♦ represents the solution based on the  $J_2$  invariant orbit with perigee drift in Ref. [20].

is readily apparent from the graph that using additional  $\Delta V$  will produce diminishing returns in terms of reducing drift.

Initial conditions generated by other  $J_2$ -invariant conditions should lie either on or above the optimized result. The ■ in Fig. 3-2 represents the initial condition based on the  $J_2$  invariance condition in Case 1 of Ref. [110] that requires no mean period drift. The point is nearly optimal for this example, but this is not guaranteed to be the case for other problems. The ♦ indicates the drift that occurs when using semi-invariant initial conditions that allow perigee drift [20]. In both specific cases, the partial invariance conditions allow for a range of possible initial conditions. Both analytic cases occur near the same drift levels as the initial conditions found by the optimizing approach. This indicates the optimized ICs may, in those cases, be meeting the same invariance criteria, while simultaneously finding ICs that minimize

fuel use. The optimization-based approach enables the identification of a range of fuel-optimized initial conditions that can be used to better meet the requirements of a specific mission.

Figure 3-3 shows a number of optimizations of the same orbit and desired offset, however, in this case, both  $Q_x$  and  $Q_u$  are made significant while  $Q_d$  is varied. The figure shows the cost associated with changing the formation geometry ( $\|W_x \hat{\Gamma} U\|_1$ ) versus the fuel cost ( $\|U\|_1$ ). When  $Q_x$  is very high relative to  $Q_d$ , the optimized ICs,  $\delta \mathbf{e}(t_1)$ , are equivalent to the open-loop propagation of  $\delta \mathbf{e}(t_0)$  (*i.e.*, no fuel is used). This corresponds to 12m of drift over an orbit. As  $Q_d$  is increased, the optimized ICs are farther from  $\bar{\Phi}_{D0}^* \delta \mathbf{e}(t_0)$ , but the resulting drift is lower because  $Q_d$  has a greater effect on the solution. The solution that achieves 0.5m of drift with almost no geometry cost represents a compromise between the desired formation geometry and the drift resulting from the effects of relative  $J_2$ . At the cost of slightly repositioning the formation (velocity changes are not penalized in the  $W_d$  used for this example), the drift over an orbit has been reduced by 4m. When invariance dominates (the lower-right corner of the figure), the optimized initial conditions cancel almost all of the orbital offset  $\delta \mathbf{e}$ , indicating that geometry goals have been ignored.

Figures 3-4 and 3-5 show the effect of independently varying the fuel and geometry weights for an MMS-like HEO orbit

$$\mathbf{e}_A(t_0) = \begin{bmatrix} 6.6 & 0.82 & 0.17 & 6.28 & 6.28 & 3.14 \end{bmatrix}^T \quad (3.6)$$

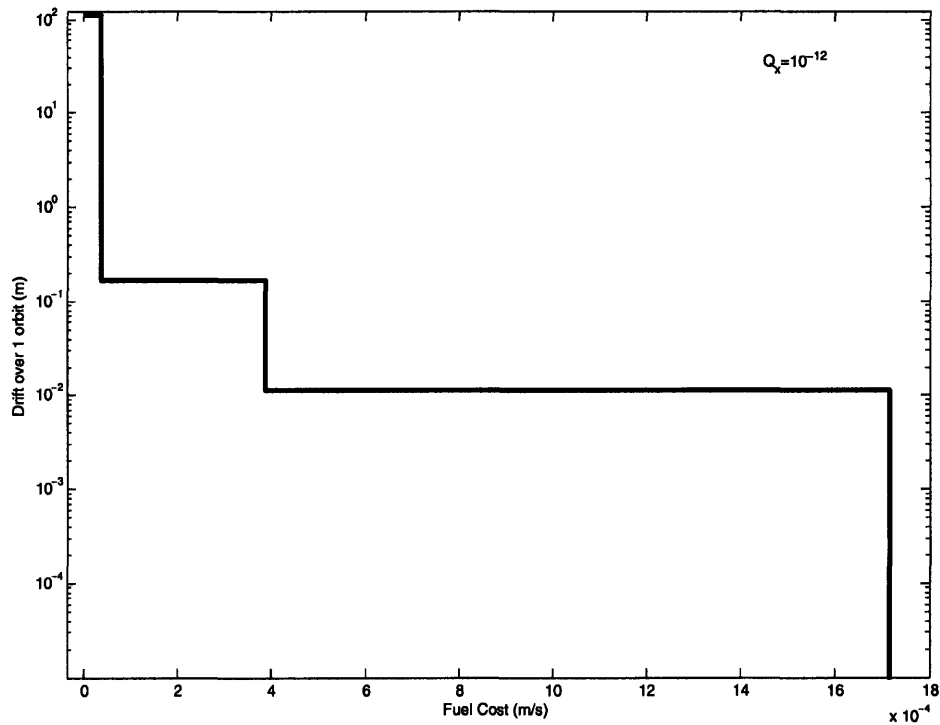
with the desired geometry

$$\zeta(t_0) = \begin{bmatrix} -4.00000 \times 10^{-8} \\ -4.98086 \times 10^{-7} \\ -8.50000 \times 10^{-7} \\ 2.30000 \times 10^{-7} \\ -7.33646 \times 10^{-7} \\ 3.72778 \times 10^{-6} \end{bmatrix} \quad (3.7)$$

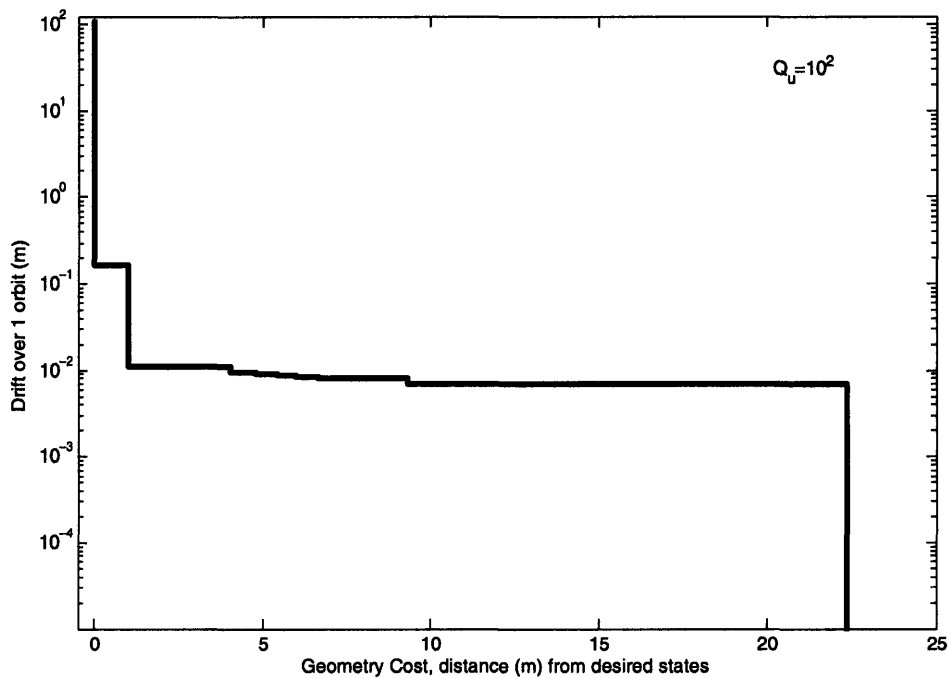
As in the LEO case, the unmodified initial conditions experience a significant amount of drift, which can be greatly reduced using comparatively small fuel expenditures. Likewise, small (centimeter) changes in the formation geometry can also decrease the drift. In this case, more intermediate optimized geometry steps exist, allowing for additional choices between precisely achieving the desired shape and drifting out of that shape over the course of the next orbit.

Figure 3-6 shows an example in which a spacecraft trajectory is simulated using a commercially available fully nonlinear propagator that accounts for the effects of many realistic disturbances, including  $J_2$ , drag, and solar pressure. The reference orbit has a semimajor of 1.08 Earth radii, an eccentricity of 0.03, and an inclination of 45 degrees. The two lines show two possible relative trajectories for a spacecraft initialized in a 2 km in-track formation. The solid line shows initial conditions that are chosen by creating a 2 km separation in-track separation in LVLH coordinates and then adjusting the velocity to eliminate differential semimajor axis. The dashed line shows the trajectory which results from using the initial conditions given as outputs from the optimization method presented in this chapter when the fuel penalty is zero and the geometry and drift penalties are weighted equally. In this case, the optimized initial conditions begin 12 m away from the desired 2 km mark, well within the 100 m error box that would be used for a 1 km (at apogee) baseline formation. The drift reduction for this tradeoff was on the order of 400 m per day. In the simulation shown in Figure 3-7, all realistic disturbances are modeled except  $J_2$  and the same initial conditions produce significantly different results. In this case, SMA-corrected trajectory (solid line) creates a path with almost no drift and the  $J_2$ -corrected optimized trajectory now produces drift. This drift is caused by the  $J_2$  correcting SMA offsets that the optimizer produces, which become a source of drift in a simulation without  $J_2$  perturbations.





**Fig. 3-4:** Expected drift due to differential  $J_2$  effects and fuel cost of a range of optimized initial conditions in a HEO orbit. The lines between marked points indicate the least drift that can be attained for the indicated amount of fuel.



**Fig. 3-5:** Expected drift due to differential  $J_2$  effects and geometry cost of a range of optimized initial conditions in a HEO orbit. The lines between marked points indicate the least drift that can be attained for the indicated amount of separation from the desired orbital offset.

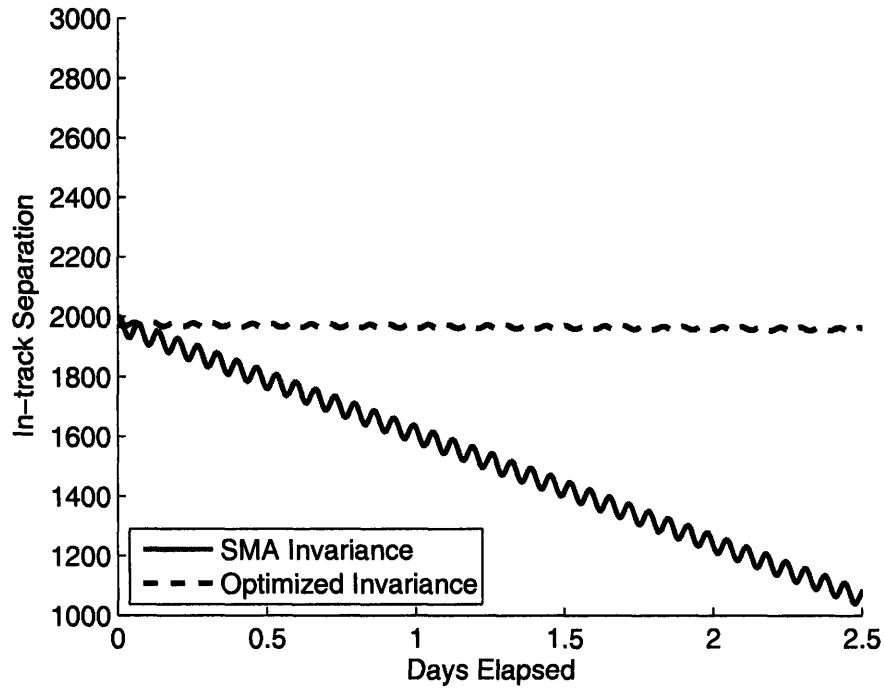


**Fig. 3-6:** Relative satellite separations for a vehicle initialized using analytic invariance and a vehicle using optimized invariance. Trajectories generated using realistic nonlinear simulation including the effects  $J_2$ .

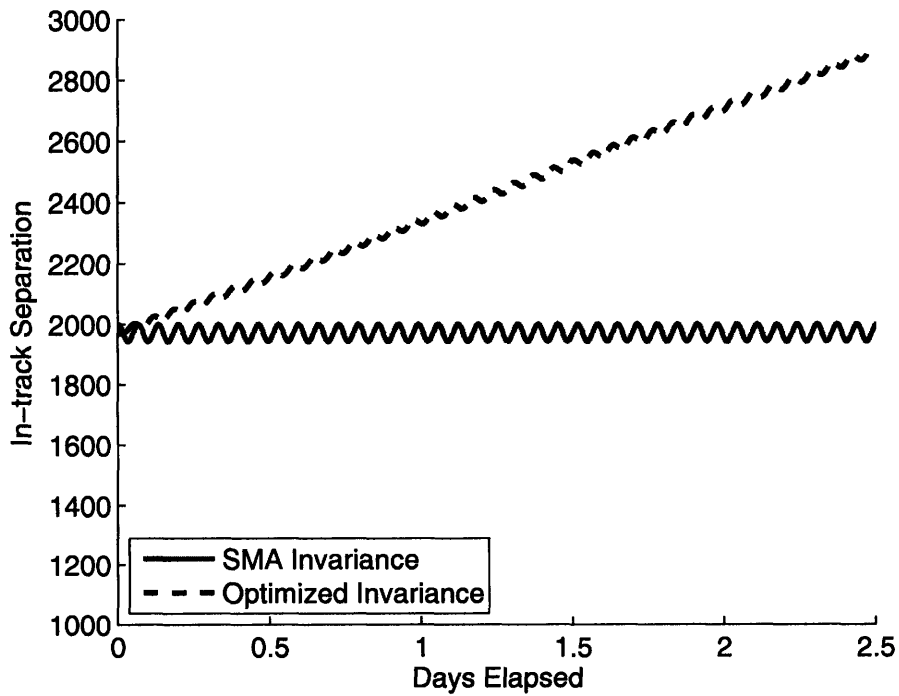


**Fig. 3-7:** Relative satellite separations for a vehicle initialized using analytic invariance and a vehicle using optimized invariance. Trajectories generated using a nonlinear simulation that did **not** incorporate the effects  $J_2$ .

### 3.3 Summary

This chapter introduced a new approach to creating invariant relative orbits. The method uses linear optimization to find initial conditions that minimize drift, but also maintain a desired geometry and minimize the fuel use required to attain the initial conditions. This approach represents a hybrid between trajectory planning and formation design that balances the common approach of finding ideal drift-minimizing initial conditions against the practical need to not waste fuel in an effort to reduce fuel use. Multiple definitions of drift over arbitrary time-frames are considered including mean drift, osculating drift, and Cartesian drift. The range of solutions produced by the new technique was examined for several reference orbits and compared to analytic approaches.



# Chapter 4

## Formation Flying Simulations

### 4.1 Introduction

Using the dynamics introduced in Chapter 2 inside a model predictive controller, it is possible to demonstrate closed-loop control subject to constraints for widely separated missions with coupled control/performance objectives and multiple large formation reconfigurations.

### 4.2 Mission Description

A series of nonlinear simulations of portions of the Mitsubishi Electric Company (MELCO) reference mission [113] (see Figure 4-1) were performed using the FreeFlyer™ orbit simulator [112] in order to demonstrate the effectiveness of the controller/dynamics combinations in Chapter 2 for controlling a realistic satellite formation through all planned stages of operation. A commercial orbit propagator, FreeFlyer™, was used propagate orbits in an absolute frame for both satellites. Propagation included the effects of many realistic disturbances, including drag, lift, solar radiation pressure, and  $J_2$ . The propagator interacts with the controller through a MATLAB™ interface. During each propagation step, the control algorithm is queried. If the controller is currently implementing a thrusting plan, the thrusts corresponding to the current position in the plan are converted into appropriate orbital element offsets and re-

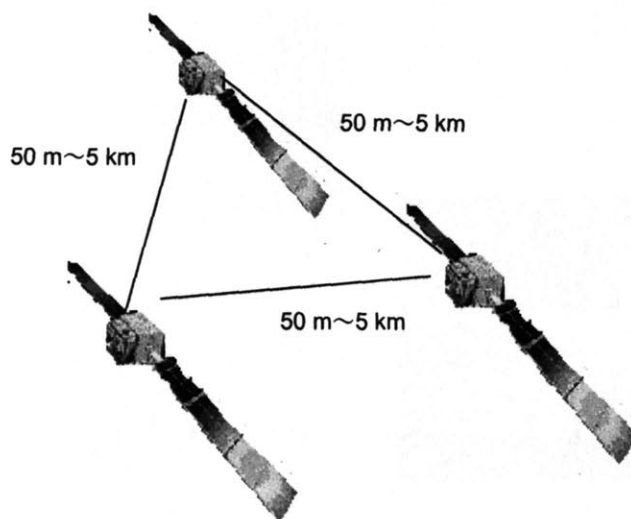


**Fig. 4-1:** Concept for MELCO formation flying mission [113]

turned to the propagator. After each plan is completely implemented, a new plan is created.

The simulation presented in the following sections involves a three satellite formation. The reference orbit, represented by a virtual satellite with properties similar to the average of the fleet, has a semi-major axis of 6900 km, inclination  $45^\circ$ , and eccentricity 0.003. Realistic disturbances (drag,  $J_2$ , solar radiation pressure, Sun/Moon effects) were included in all simulations.

Each satellite is modeled as on the current specifications for the MELCO formation flying mission [113]. Each satellite has a mass of 900 kg and a ballistic coefficient of 0.4. The satellite thrusters are restricted to provide a maximum of 2 Newton of force over a 10.8 second time step. Lawden's time-varying equations are used to determine the desired state for each spacecraft, however Hill's equations are used in LP problem. This is consistent with the observation in Ref. [84] that slightly eccentric orbits ( $0.0005 < e < 0.01$ ) require eccentricity-invariant initial conditions, but not time-varying dynamics. Ten minutes of each orbit are reserved for observations: during this time position constraints are enforced, but no thrusting is permitted.

The MELCO formation flying mission consists of two different formation shapes: 1) in-track separation formations and 2) in-track/cross-track passive aperture forma-

tions (triangular). Over the course of a mission, the formation is designed to achieve four different configurations in the following order:

1. In-track formation with 1 km (at apogee) of separation between spacecraft (represents deployment configuration)
2. Passive aperture formation with 50 m baseline
3. Passive aperture formation with 500 m baseline
4. Passive aperture formation with 5 km baseline

For each type of formation at each baseline, one or more 18 day simulations were conducted to determine the average fuel usage. The mission requirements [113] specify that each formation size must use an error box that is 10% of the baseline.

### 4.3 Simulation Controller Configuration

The planning controllers used in the simulations in this Chapter use a modified form of the basic problem statement in Chapter 2. Each spacecraft designs its control individually and coordination between spacecraft is accomplished through the design of the formation desired states at the time the formation is initialized. Error box constraints of the type in Ref. [84] are added at every 6 time steps to ensure that satellites achieve their performance objectives, while reducing the computational burden of imposing them at every time step. In addition, fuel inputs are permitted every 6 time steps for station-keeping (in which spacecraft are tasked to remain in formation) and every time step for formation maneuvers (those periods during which the formation is being switched from one configuration to another). Mission requirements [113] specify that a ten minute time window at apogee should be reserved during formation-keeping maneuvers in which no thruster inputs are permitted.

An always-feasible formulation was used for the simulation controller, guaranteeing that a plan is always returned, even if no feasible solution exists which satisfies the error box constraints. The always-feasible formulation is based on the constraint

enlarging approach presented in Ref. [84], but with a modification allowing several degrees on constraint violation. If no feasible solution is possible for the desired error box, the approach in Ref. [84] enlarges the error box as little as possible until a feasible solution is found. However, the resulting plan may end with the spacecraft outside the nominal box, which would guarantee that the next plan would use as much fuel as necessary to return the spacecraft to the error box on the first step of the plan or would also require an expansion of the nominal box. The always-feasible formulation used in this section also enlarges the error box until a feasible plan is found, but includes another soft constraint which prefers that the planned trajectory still end inside the nominal error box. This additional constraint is also implemented using with an additional high cost-penalty variable that is used to ensure that it is only relaxed in the event that no feasible solution exists that enlarges the error box and ends inside the nominal error box. The modified always-feasible formulation allows the controller to prefer plans that make future optimizations initially feasible.

### 4.3.1 Parameters Examined

An initial simulation of the mission in Sec. 4.2 using the parameters and specifications in Sec. 4.3 was conducted. The results of that simulation indicated that levels of CDGPS noise expected were excessive for the station-keeping in a 50 m passive aperture formation with  $5 \text{ m} \times 5 \text{ m} \times 5 \text{ m}$  error box, the most tightly constricting phase of the mission. The controller was unable to keep the satellite constrained to its error box under those conditions and experienced errors that grew over time. In order to investigate this phenomenon and find a stable configuration for the controller that met as many mission requirements as possible, a number of variations of the basic controller setup in Sec. 4.3 have been implemented and tested in realistic simulations. Section 4.4 presents the results of those simulations and evaluates the effectiveness of the parameter variations in terms of effectiveness at preventing error box violations and average fuel use. The control parameters considered are:

#### **Thrusting During Observations**



The MELCO mission specifications indicate that passive aperture radar observations cannot occur when any spacecraft in the formation is thrusting. As a result, the basic configuration in Sec. 4.3 prevents thrusting during a 10 minute period at the apogee of every orbit that the formation is in the passive aperture configuration. However, the MELCO mission reference orbit is 95 minutes, so the effect of the observation thrusting prohibition is to reduce the overall control authority of any plan by more than 10%. Although, this requirement is hard constraint for the mission, it is included as a parameter in the simulation study so that its effects formation flying mission performance can be judged.

### **Error Boxes Relaxed When Not Observing**

One of the original concepts for the MELCO formation flying mission [113] specified that the formation should be in a passive aperture during periods when the formation taking observations and transition to a widely separated during periods when observations are not needed. The maneuver generation analysis in Appendix A indicates that there is generally no fuel advantage to formation-keeping in an in-track formation versus a passive aperture formation and that the cost of maneuvering into and out-of holding configurations is unnecessary.

Given that the tight error box requirements are derived from the needs of the distributed observation instrument, a reasonable modification of the mission requirements is to enlarge the error boxes during the 85 minutes of each orbit in which no observations are taking place and only enforce tight performance constraints when they are strictly needed. This constraint is implemented by doubling the error box size during the time steps outside the 10 minute period reserved for observations at apogee.

### **Dynamically Motivated Error Box Shapes**

Because the 50 m passive aperture is the most fuel-intensive of the formation configurations, a  $5 \times 10 \times 5$  meter (radial/in-track/cross-track) error box is examined as an alternative to the 10% requirement for that portion of the mission. The  $5 \times 5 \times 5$  meter error box is sufficiently small that the navigation errors [73]

strongly influence the closed-loop behavior. Enlarging the in-track dimension allows a slightly more natural relative elliptical motion in the radial/cross-track plane (typically a  $1 \times 2$  ellipse). This observation is derived from the form of Hill's equations, in which the coefficients of the harmonic terms for the in-track axis are exactly twice the value of the coefficients of the harmonics terms for the radial axis.

### **Invariance Terminal Condition**

A plan that is optimized to guarantee that a spacecraft remains inside an error box over some future horizon will accomplish that goal, but will not provide any guarantees for the future behavior of the spacecraft. Occasionally, a situation may arise where the spacecraft would approach its constraint boundary in the near future after the end of a plan. This situation is prevented from resulting in a constraint violation by the creation and implementation of a new plan. However, if the new plan is forced to react quickly to a potential constraint violation in the near term, the only feasible solution may require a great deal of fuel. In an effort to reduce the need for vehicles to make short term "emergency" corrections, an invariant set terminal condition was examined. In this case, the condition guarantees that after a plan is ended, the spacecraft will naturally (*i.e.*, with no thrust inputs) remain inside its box for a full orbit and return to its state at the time the plan ended. Within the time span that the dynamics can accurately propagate the states, this terminal constraint guarantees perpetual collision avoidance in the absence of state knowledge uncertainty. This constraint is imposed using the nominal estimate of the spacecraft state, because a implementation is generally infeasible.

## **4.4 Simulation Results**

Multiple simulations were performed to study the MELCO formation flying mission and the effects of the control system parameters introduced in Sec. 4.3. These simulations are described in Table 4.1.

**Table 4.1:** Fuel use results for formation flying simulations. Fuel costs for station keeping (SK) are given in mm/s/orbit/satellite and fuel costs for maneuvers (Mvr) are given in m/s for the entire formation.

	50 m PA: 5 x 5 x 5 m Error Box			50 m PA: 5 x 10 x 5 m Error Box		
	Sim 1	Sim 2	Sim 3	Sim 4	Sim 5	Sim 6
No Thrust Observation	No	Yes	Yes	No	Yes	Yes
No Observe Large EB	No	Yes	No	No	No	No
Mnvr. End Invariance	No	No	Yes	No	No	Yes
SK 50 m	45.96	106.51	53.73	8.39	33.47	12.01
SK 500 m	0.06	0.09	1.54	0.06	0.04	1.51
SK 5 km	5.83	27.47	1.69	6.8	29.47	1.72
Mvr #1	1.06	0.56	0.65	0.71	0.57	0.57
Mvr #2	17.94	36.57	19.97	5.78	13.51	6.8
Mvr #3	51.37	65.73	48.59	39.4	48.15	35.42

In Figs. 4-3-4-20, the vast majority of the trajectories remain inside the error boxes. Several instances of error box constraint violations occurred as a result of the always-feasible formulation, but were quickly corrected. Several general trends are visible: in most cases the 50 m passive aperture requires the most fuel to maintain and the 500 m passive aperture requires the least fuel to maintain. Also, enlarging the in-track dimension of error box tended to reduce fuel use a great deal in comparable simulation configurations (*i.e.*, Sim 1 & Sim 4 and Sim 3 & Sim 6).

Interestingly, the least restrictive error box (5 km) did not result in the lowest fuel use. This phenomenon is likely due to the reduced likelihood of encountering constraints in a single orbit planning horizon for the larger error box. As a result, it is possible for a spacecraft to enter into a large, high speed relative orbit that may end near an error box constraint. In those situations, future trajectory optimizations would need to take immediate corrective action to avoid constraint boundaries. This hypothesis is supported by significant reductions in fuel use for the 5 km passive aperture between Sim 1 & Sim 3 and Sim 4 & Sim 6, even with fewer thrusting times available in Sim 3 and Sim 6 due to constraints against thrusting during observations. In both cases, the only difference between the simulations is the inclusion of the terminal invariance constraint and a restriction against thrusting during observations.

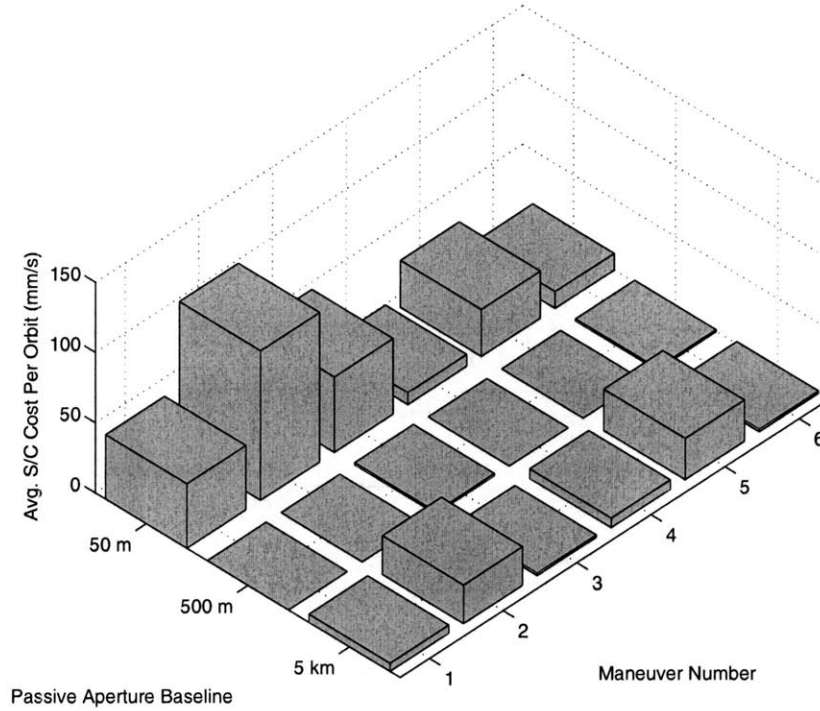


**Fig. 4-2:** Summary of Station-keeping Results from Table 4.1

The restriction against thrusting tends to increase the fuel use, as in the Sim 4 & Sim 5 pair. In Sim 4, thrusting is permitted at all times in the orbit, whereas in Sim 5 10% of the orbit is reserved for observations. In the 50 m and 5 km configurations, the 10 % restriction increased fuel use by more than an order of magnitude for those simulations. It is likely the that difference between the fuel use numbers for the 500 m configuration is insignificant due to random elements in the simulations.

The addition of the terminal invariance constraint in Sim 6 lowers the fuel consumption for the 5 km configuration, but raises it for the 50 m and 500 m baselines compared to Sim 4. At the 5 km level, the reduction is greater than a factor of 3. Figures 4-14 and 4-20 show the error box motion for all three satellites in the formation for station-keeping in the 5 km formation for Sims 4 and 6, respectively. While Figure 4-14 shows a considerable amount of motion throughout the entire error box, Figure 4-20, shows that the spacecraft actively controlled in the center of the error box. These results are counterintuitive for several reasons: 1) the addition of constraints to an optimization would typically be associated with increased fuel cost; and

2) expending fuel to keep a spacecraft in a small box would usually be more expensive than allowing the same spacecraft to stay in a large box. The fact that the fuel costs were reduced is not in conflict with the fact that individual optimizations should have increased cost; the fuel costs measured are the steady state closed-loop levels of consumption, as opposed to expected maneuver costs. Also, note that the fuel use in Sim 4 remained high for a period after the maneuver to the 5 km configuration before settling into a steady state, whereas the Sim 5 fuel use settled almost immediately. This is likely because the terminal invariance condition forces the trajectories to enter closed ellipses. In Sim 4, where no invariance condition was specified, the spacecraft did not start in a closed ellipse, but did eventually enter one and not exit for the duration of the simulation. This is because even without requiring a closed-ellipse, the optimization recognizes that there is no need to expend fuel to change a trajectory which will result in no constraint violations. An almost identical pattern is visible between Sim 1 (which does not impose terminal invariance) and Sim 3 (which uses terminal invariance).

Terminal invariance raises the fuel cost between Sims 1 & 3 and Sims 4 & 6 for the 50 m and 500 m configurations. At the 50 m level, this effect is complicated by the fact that the increase is small and Sims 3 and 6 both also restrict thrusting at apogee. Sims 1 and 4 were found to not be feasible with thrust restrictions. Sim 3 was feasible most of the time, but Figure 4-9 shows that there were a number of instances in which error box violations occurred. It should be noted that Sim 3 was the only one of the simulations that used the original MELCO mission control specifications and succeeded in remaining stable. All of the other simulations used modifications that enlarged the error boxes at some or all times. Sim 6 used a  $5 \times 10 \times 5$  meter error box for the 50 m configuration and did not require any error box violations. At the 500 m level, the addition of the invariance constraint causes an almost 2 order of magnitude fuel consumption increase. It appears that this is because almost no fuel is used without invariance as constraint, but the resulting trajectories are naturally invariant (see Figs. 4-4, 4-7, 4-13, and 4-16) but with slight semimajor axis mismatches which cause the ellipses to travel inside the error box. The trajectories

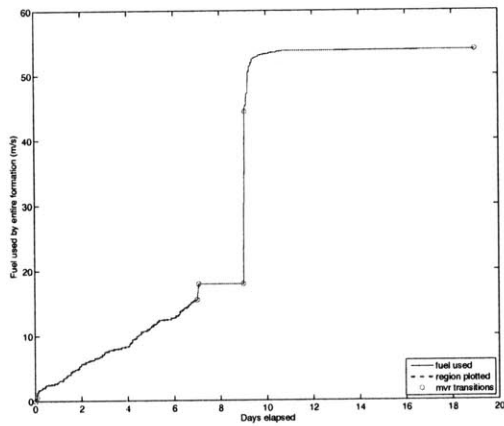
with invariance (see Figs. 4-19 and 4-19) take on similar shapes but expend fuel to cancel any real or perceived drift introduced through navigation error each with each successive optimization.

Overall, it appears that the most consistent combination of successful constraint satisfaction and low fuel came from the simulations using the invariance constraints (Sims 3 and 6). These simulations used the observation thrusting restriction and the specified error box size for Sim 3 and a slightly larger error box for the 50 m configuration in Sim 6. Thus, the 500 m and 5 km configurations were the same in Sims 3 and 6 and, as would be expected, they have nearly identical fuel use. The only difference is at the 50 m level, where a 5 m increase in the in-track error box size decreases the fuel use by more than a factor of 4.

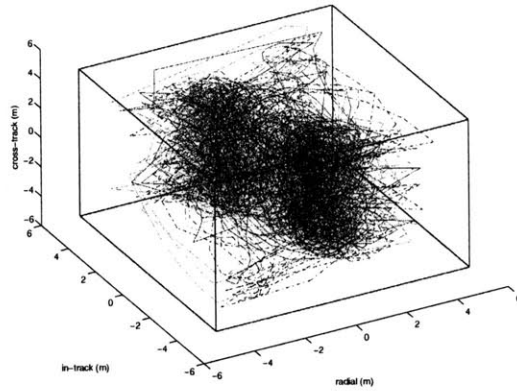
The fuel numbers for the maneuvers between formation types are included for completeness, but cannot be used to draw conclusions because of the stochastic nature of the simulations. Many additional simulations would need to be run and averages examined. This fact does not reduce the validity of the conclusions regarding the fuel use for station-keeping, because in those situations the fuel use tends to reach a steady state, as is evidenced by the linear (fixed slope) rates of fuel use in the  $\Delta V$  plots in this section.

## 4.5 Summary

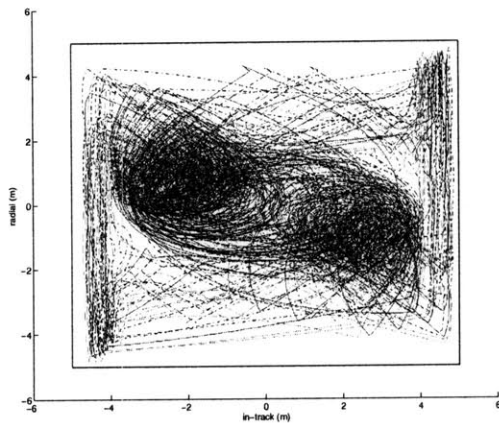
Multiple high fidelity simulations of the MELCO formation flying mission were performed successfully. These simulations demonstrated, with the most rigorous tools available, that the MELCO mission can be feasibly controlled and made to meet all of its performance constraints using the dynamics and model predictive control formulation introduced in Chapter 2. The simulations indicated that the fuel cost of reserving passive observation time can be significant. Also, it appears that the fewest constraint violations and most consistently low fuel usage occur when a terminal invariance constraint is added to the control formulation. It was demonstrated that small increases in error box size can result in large fuel savings.



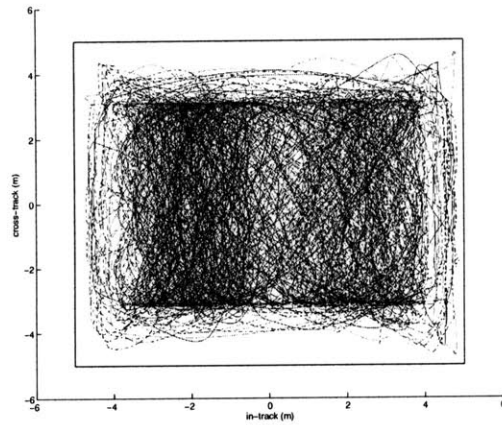
(a) Fuel Use



(b) 3D LVLH Trajectory

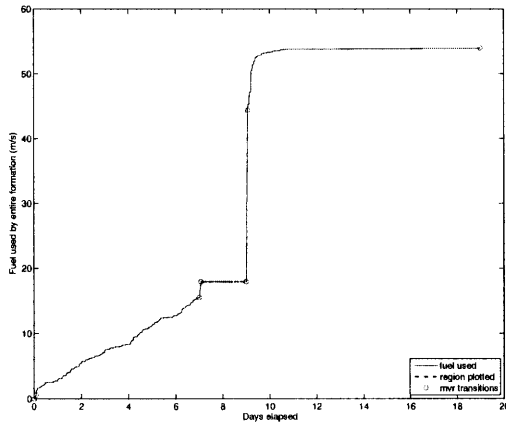


(c) LVLH Trajectory: in-track / radial

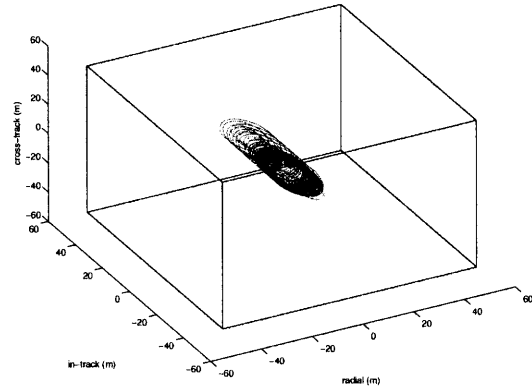


(d) LVLH Trajectory: in-track / cross-track

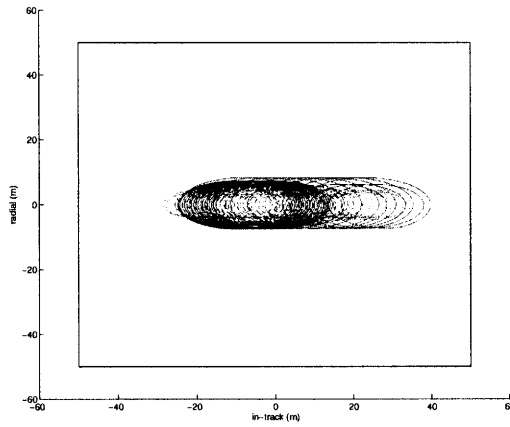
**Fig. 4-3:** Simulation #1: Stationkeeping in a passive aperture formation (50 m)



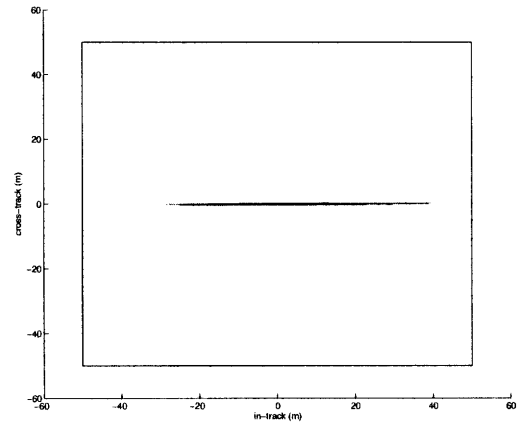
(a) Fuel Use



(b) 3D LVLH Trajectory



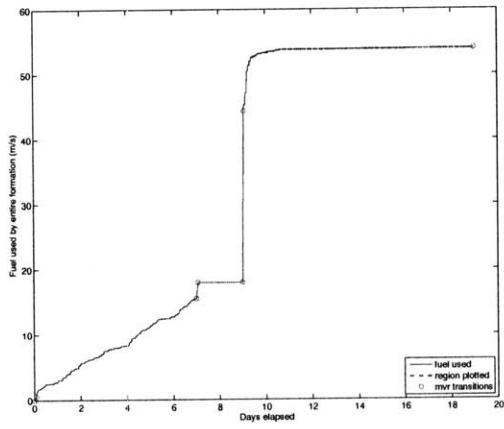
(c) LVLH Trajectory: in-track / radial



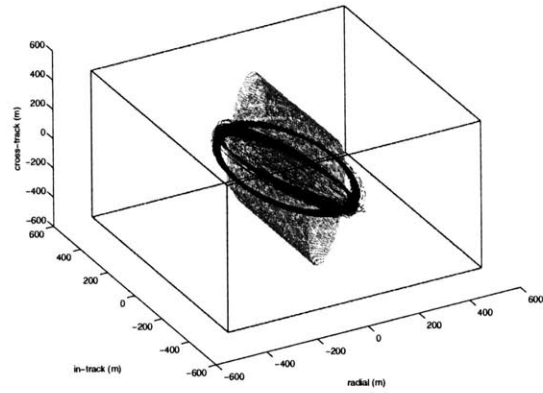
(d) LVLH Trajectory: in-track / cross-track

**Fig. 4-4:** Simulation #1: Stationkeeping in a passive aperture formation (500 m)

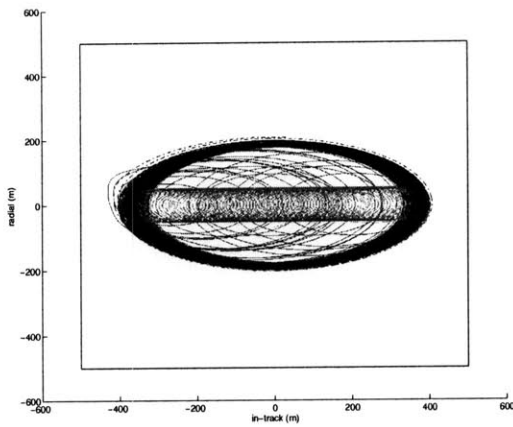




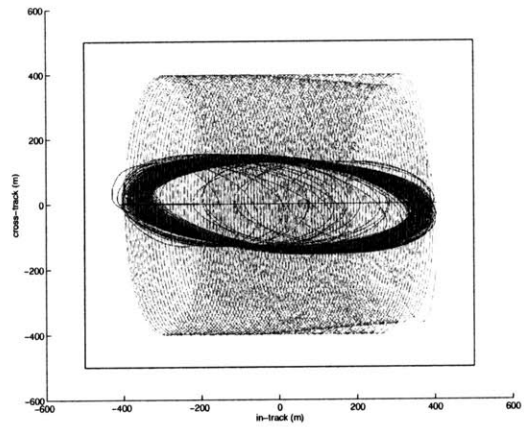
(a) Fuel Use



(b) 3D LVLH Trajectory

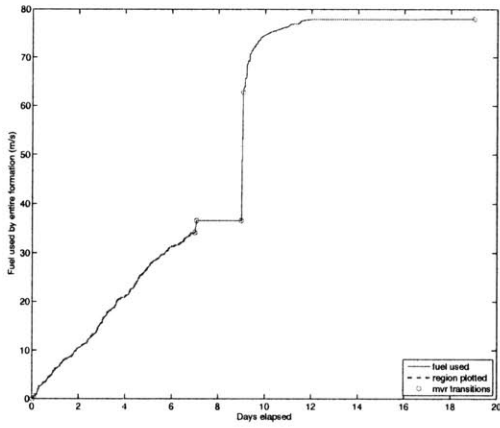


(c) LVLH Trajectory: in-track / radial

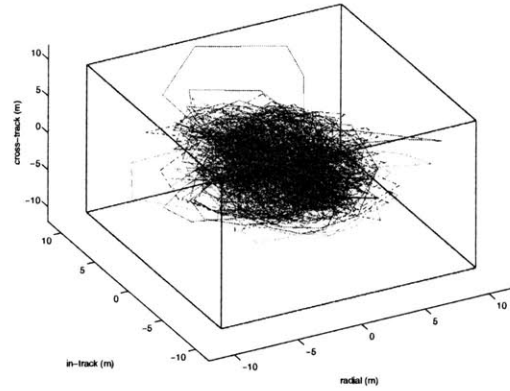


(d) LVLH Trajectory: in-track / cross-track

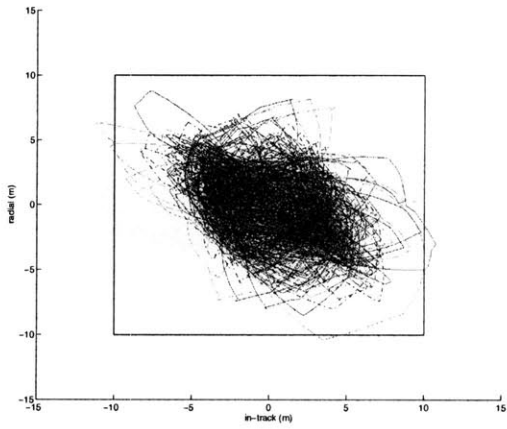
**Fig. 4-5:** Simulation #1: Stationkeeping in a passive aperture formation (5000 m)



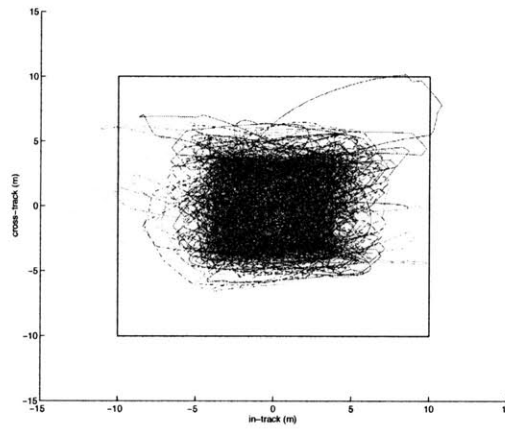
(a) Fuel Use



(b) 3D LVLH Trajectory

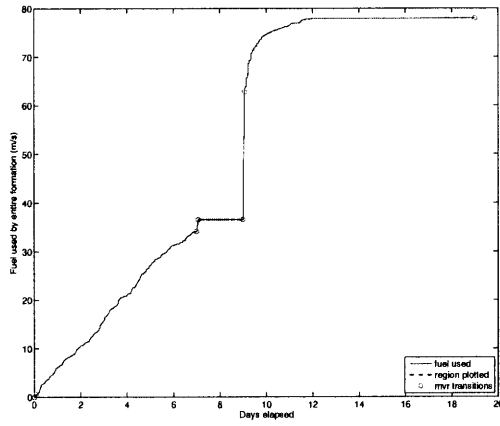


(c) LVLH Trajectory: in-track / radial

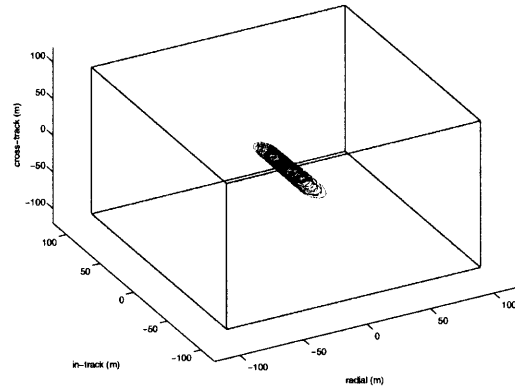


(d) LVLH Trajectory: in-track / cross-track

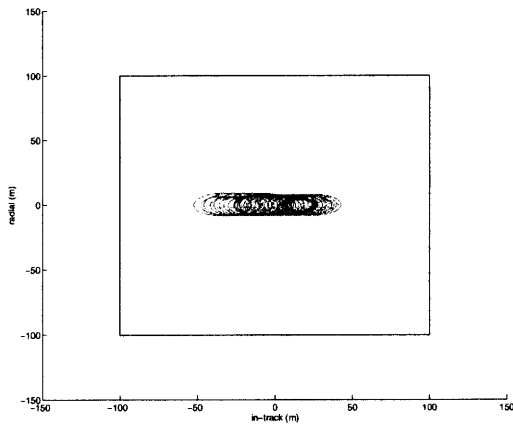
**Fig. 4-6:** Simulation #2: Stationkeeping in a passive aperture formation (50 m)



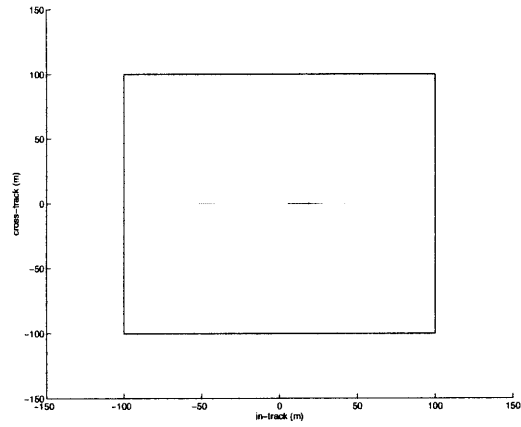
(a) Fuel Use



(b) 3D LVLH Trajectory

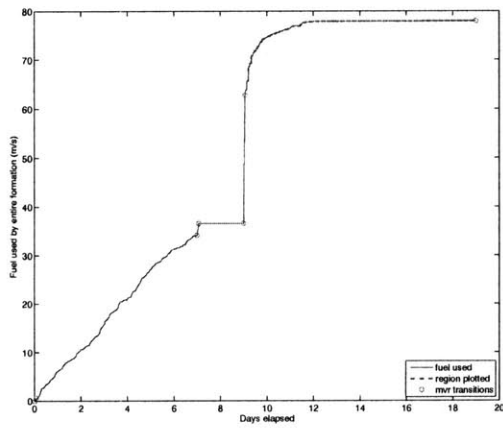


(c) LVLH Trajectory: in-track / radial

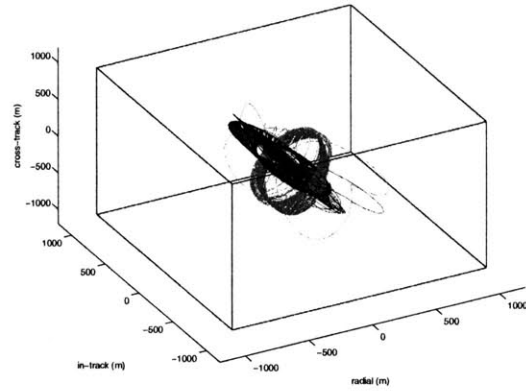


(d) LVLH Trajectory: in-track / cross-track

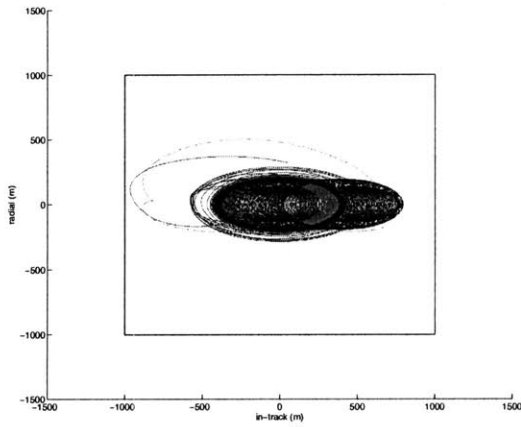
**Fig. 4-7:** Simulation #2: Stationkeeping in a passive aperture formation (500 m)



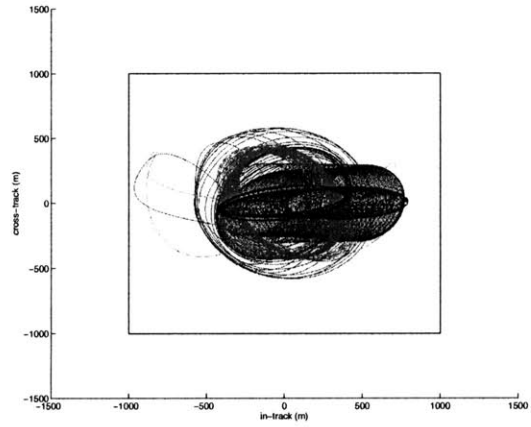
(a) Fuel Use



(b) 3D LVLH Trajectory

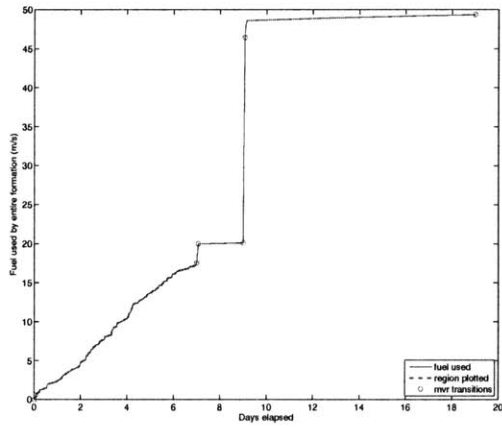


(c) LVLH Trajectory: in-track / radial

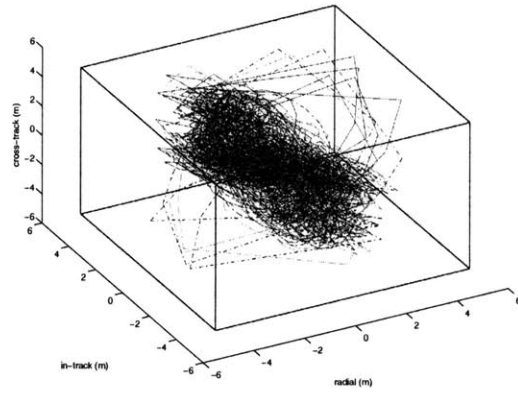


(d) LVLH Trajectory: in-track / cross-track

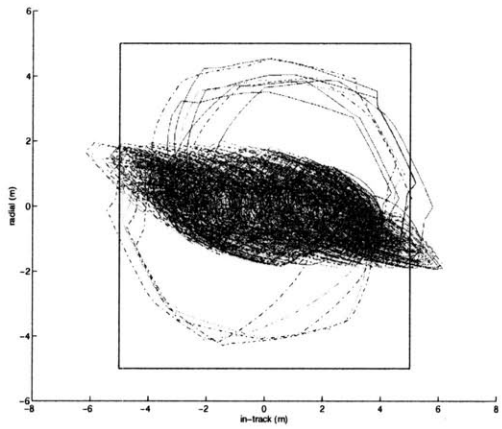
**Fig. 4-8:** Simulation #2: Stationkeeping in a passive aperture formation (5000 m)



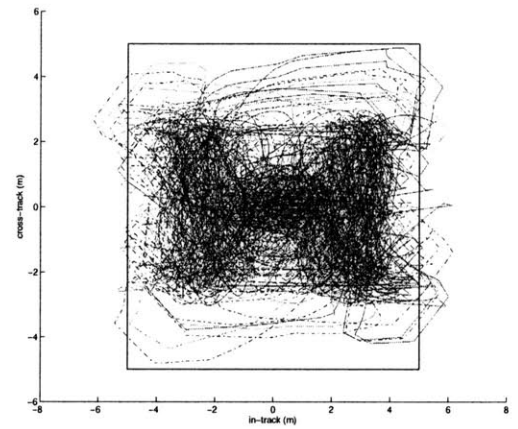
(a) Fuel Use



(b) 3D LVLH Trajectory

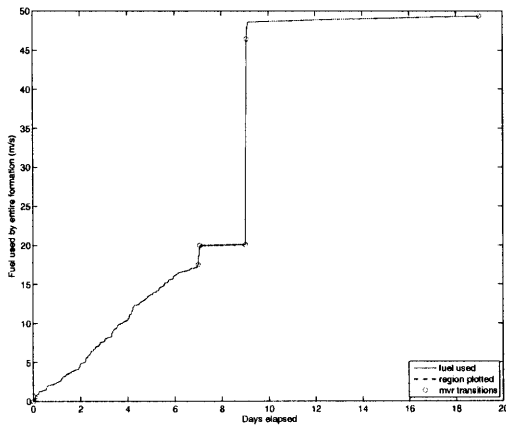


(c) LVLH Trajectory: in-track / radial

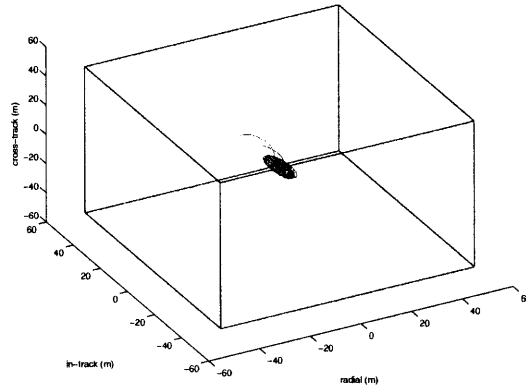


(d) LVLH Trajectory: in-track / cross-track

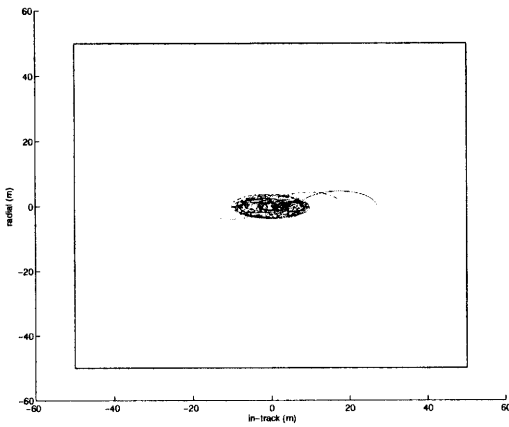
**Fig. 4-9:** Simulation #3: Stationkeeping in a passive aperture formation (50 m)



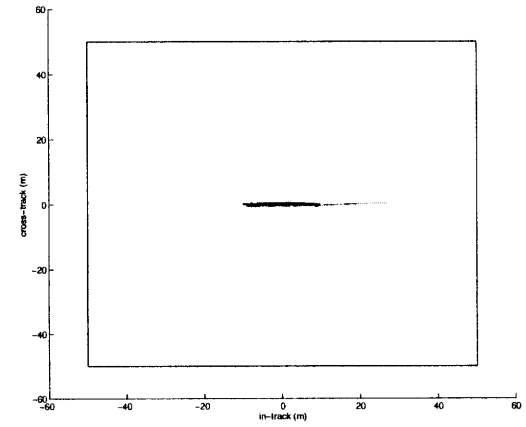
(a) Fuel Use



(b) 3D LVLH Trajectory

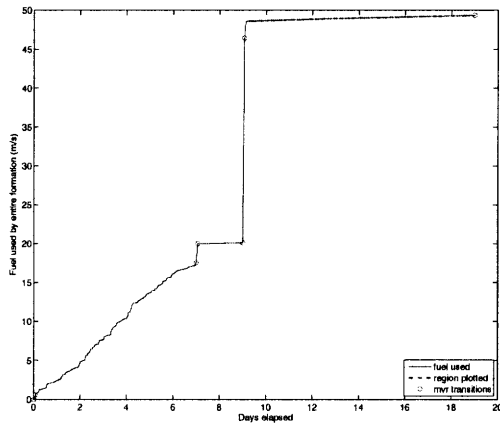


(c) LVLH Trajectory: in-track / radial

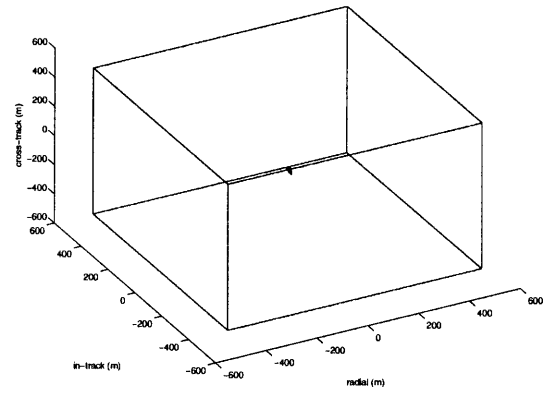


(d) LVLH Trajectory: in-track / cross-track

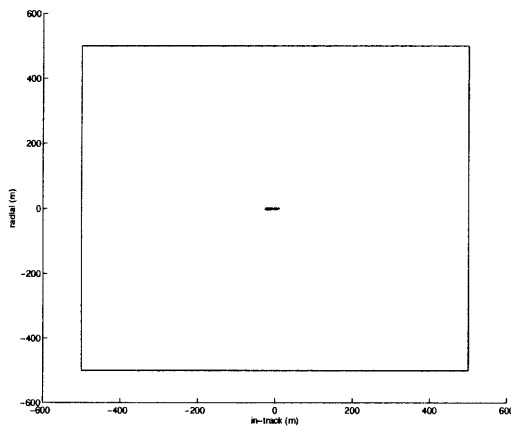
**Fig. 4-10:** Simulation #3: Stationkeeping in a passive aperture formation (500 m)



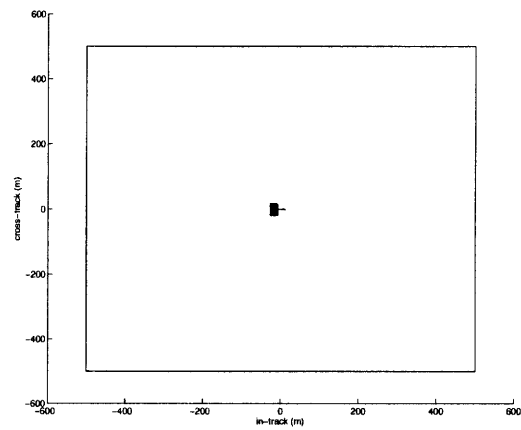
(a) Fuel Use



(b) 3D LVLH Trajectory

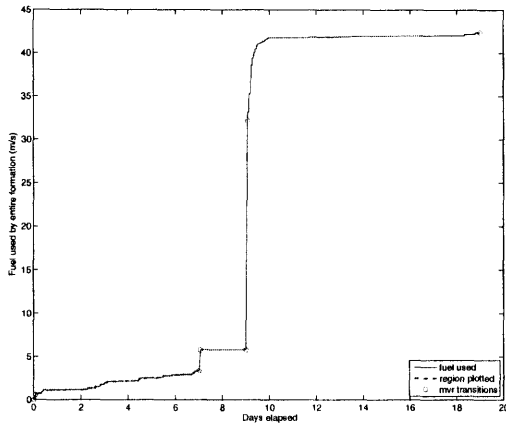


(c) LVLH Trajectory: in-track / radial

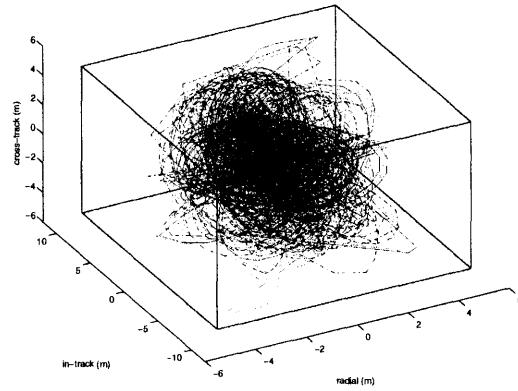


(d) LVLH Trajectory: in-track / cross-track

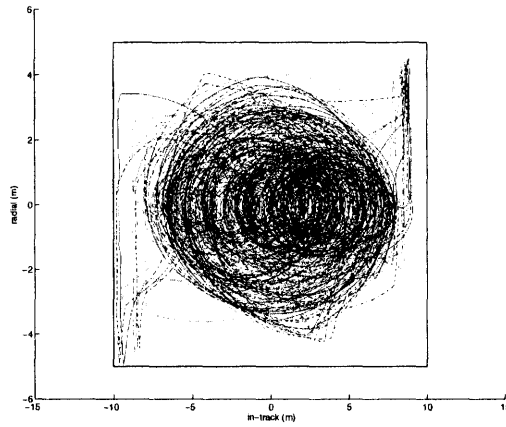
Fig. 4-11: Simulation #3: Stationkeeping in a passive aperture formation (5000 m)



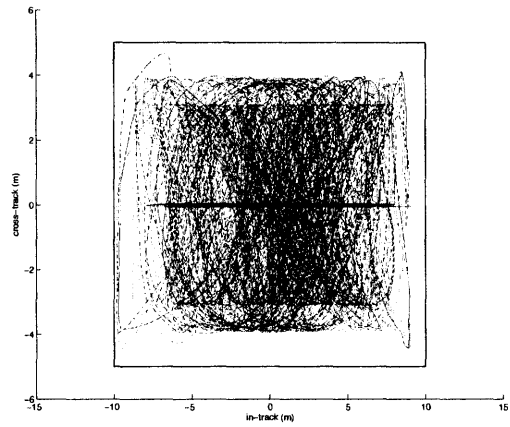
(a) Fuel Use



(b) 3D LVLH Trajectory



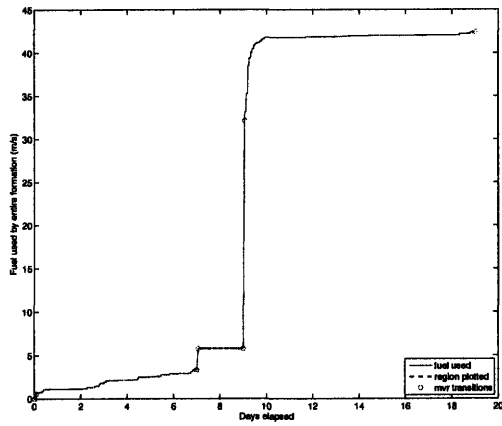
(c) LVLH Trajectory: in-track / radial



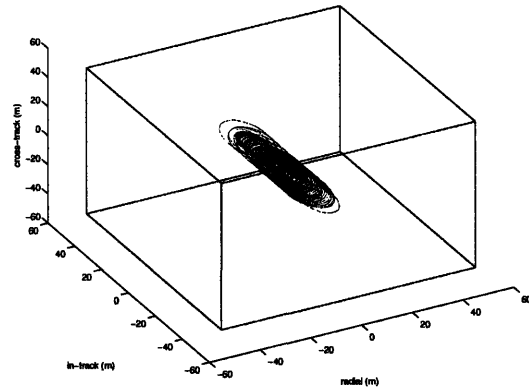
(d) LVLH Trajectory: in-track / cross-track

**Fig. 4-12:** Simulation #4: Stationkeeping in a passive aperture formation (50 m)

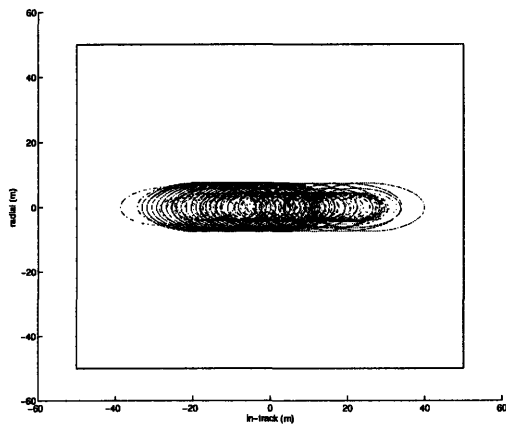




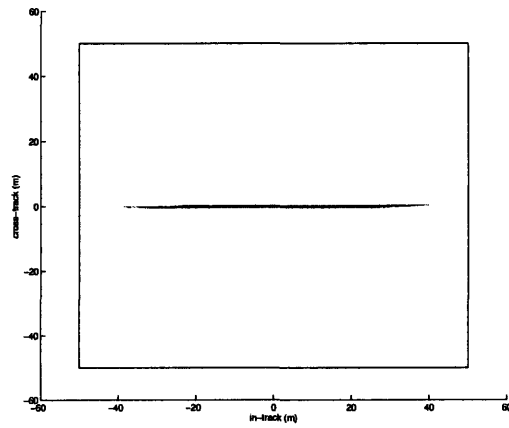
(a) Fuel Use



(b) 3D LVLH Trajectory

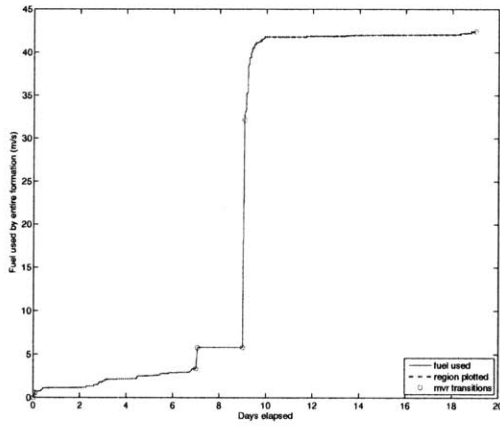


(c) LVLH Trajectory: in-track / radial

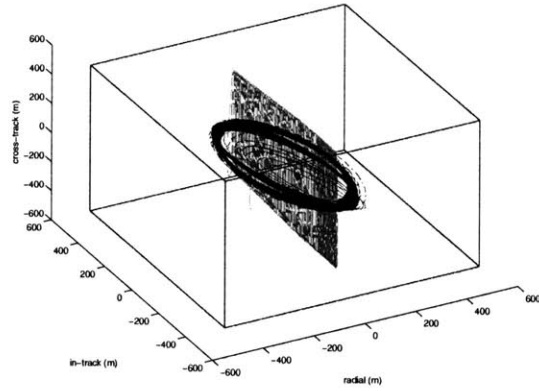


(d) LVLH Trajectory: in-track / cross-track

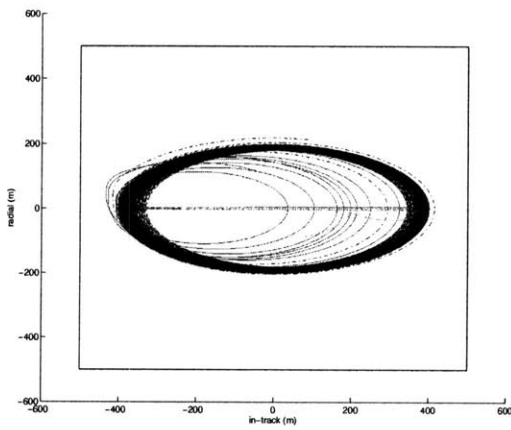
**Fig. 4-13:** Simulation #4: Stationkeeping in a passive aperture formation (500 m)



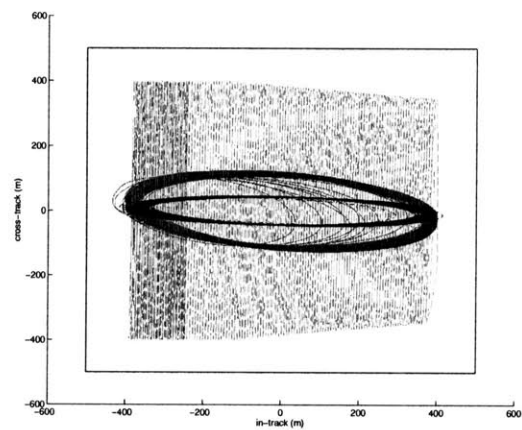
(a) Fuel Use



(b) 3D LVLH Trajectory

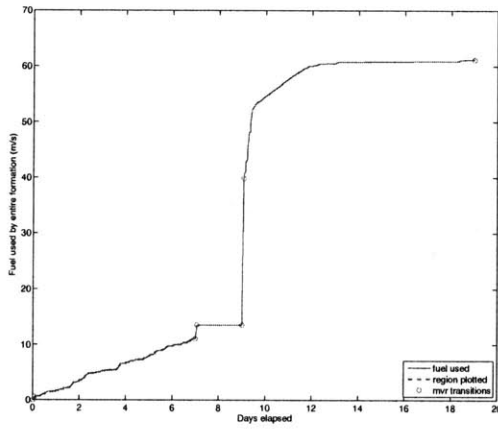


(c) LVLH Trajectory: in-track / radial

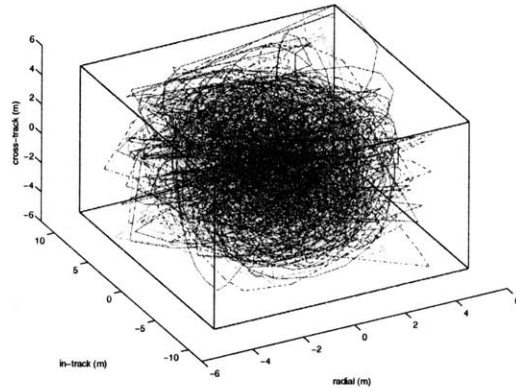


(d) LVLH Trajectory: in-track / cross-track

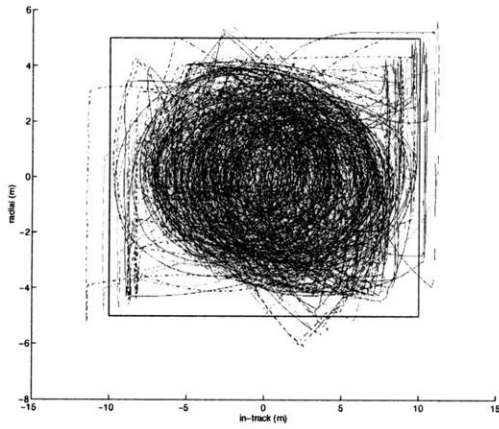
Fig. 4-14: Simulation #4: Stationkeeping in a passive aperture formation (5000 m)



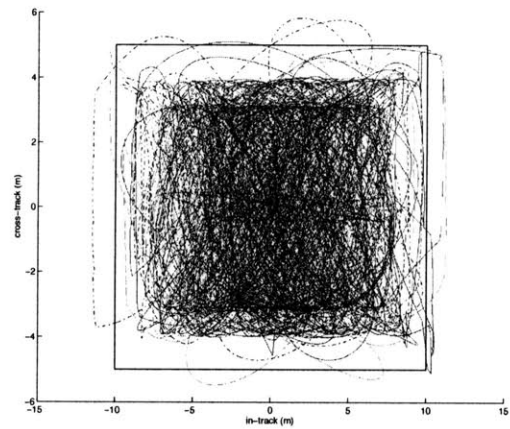
(a) Fuel Use



(b) 3D LVLH Trajectory

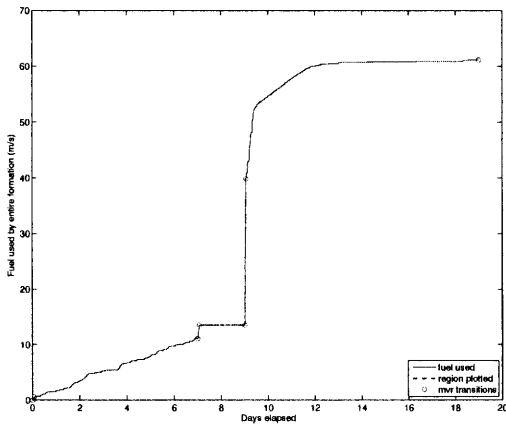


(c) LVLH Trajectory: in-track / radial

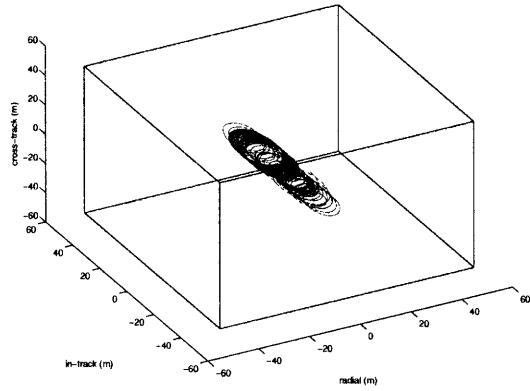


(d) LVLH Trajectory: in-track / cross-track

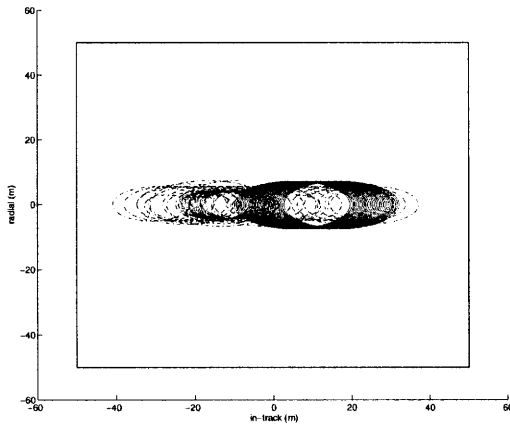
**Fig. 4-15:** Simulation #5: Stationkeeping in a passive aperture formation (50 m)



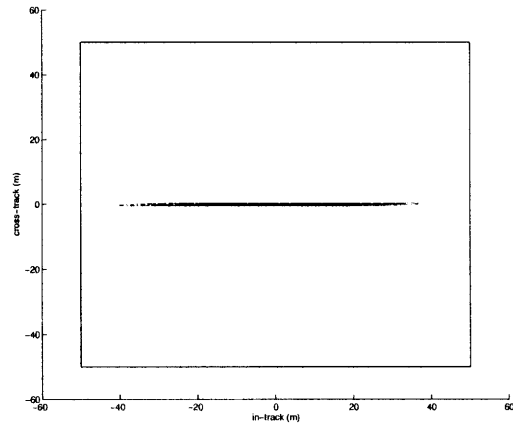
(a) Fuel Use



(b) 3D LVLH Trajectory

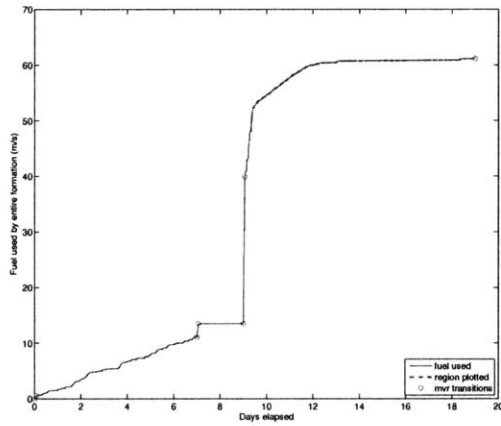


(c) LVLH Trajectory: in-track / radial

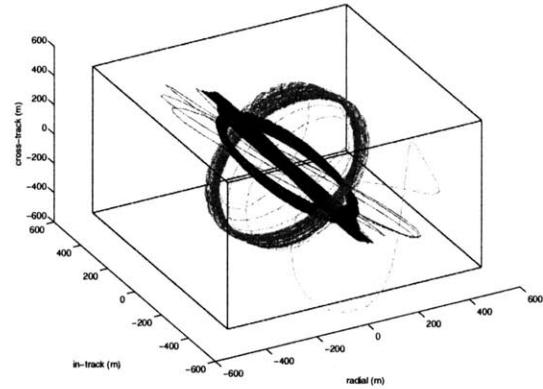


(d) LVLH Trajectory: in-track / cross-track

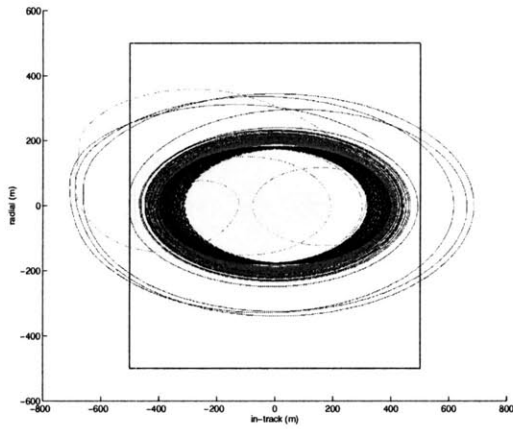
**Fig. 4-16:** Simulation #5: Stationkeeping in a passive aperture formation (500 m)



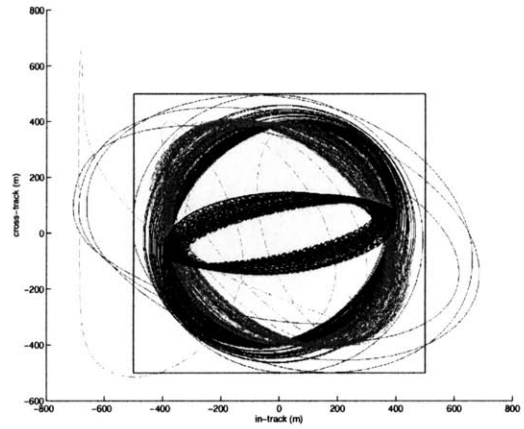
(a) Fuel Use



(b) 3D LVLH Trajectory

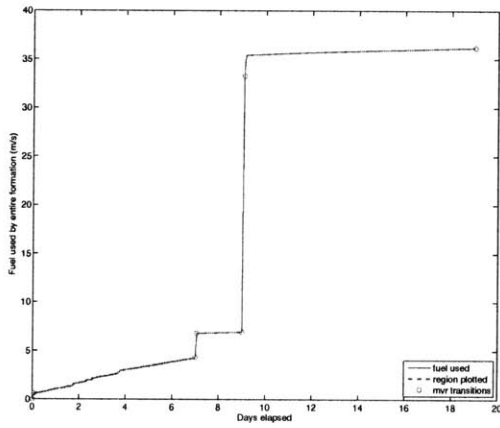


(c) LVLH Trajectory: in-track / radial

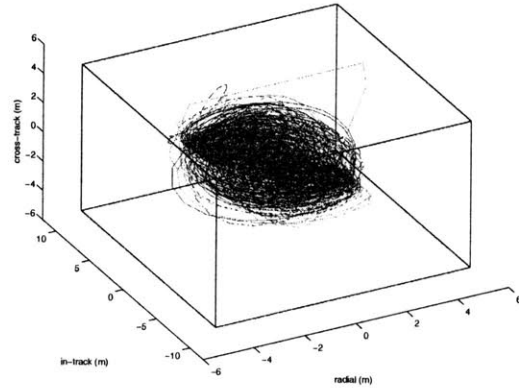


(d) LVLH Trajectory: in-track / cross-track

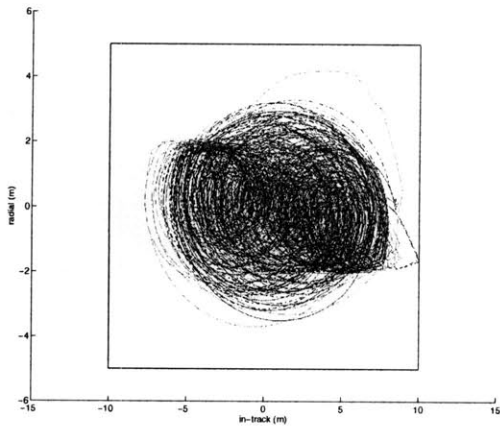
**Fig. 4-17:** Simulation #5: Stationkeeping in a passive aperture formation (5000 m)



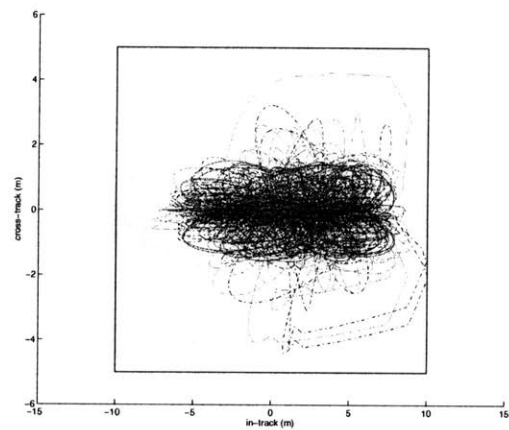
(a) Fuel Use



(b) 3D LVLH Trajectory

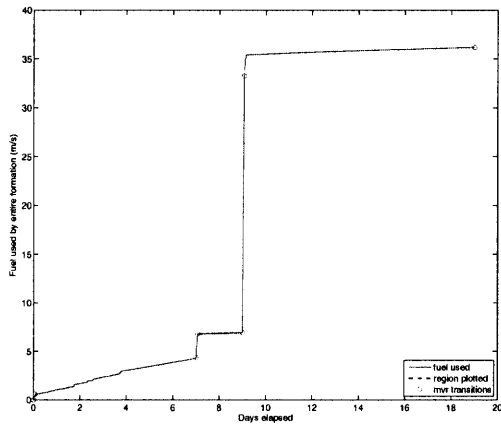


(c) LVLH Trajectory: in-track / radial

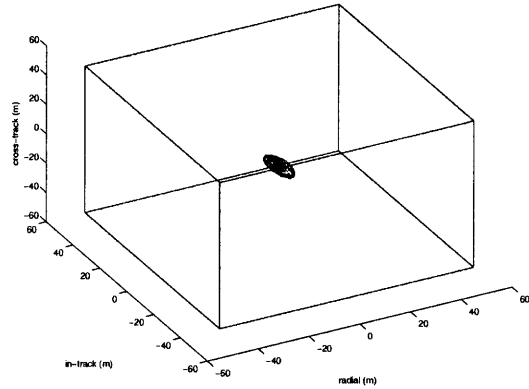


(d) LVLH Trajectory: in-track / cross-track

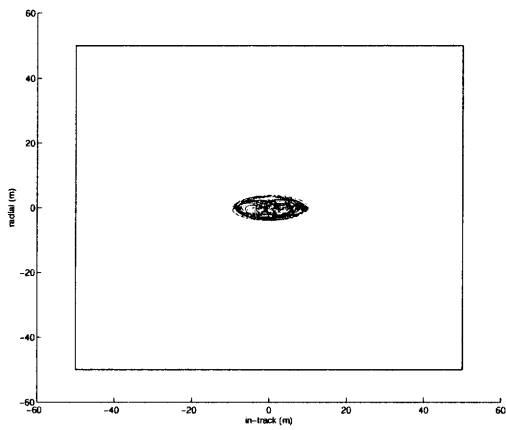
**Fig. 4-18:** Simulation #6: Stationkeeping in a passive aperture formation (50 m)



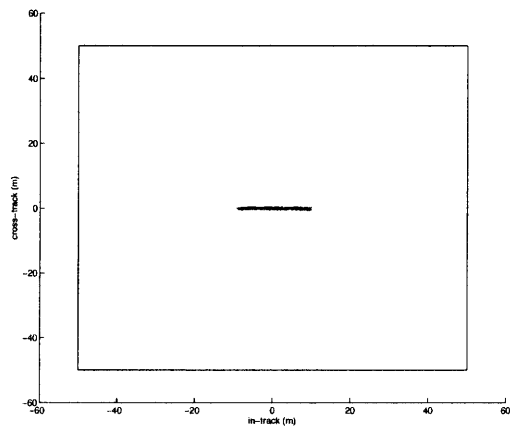
(a) Fuel Use



(b) 3D LVLH Trajectory

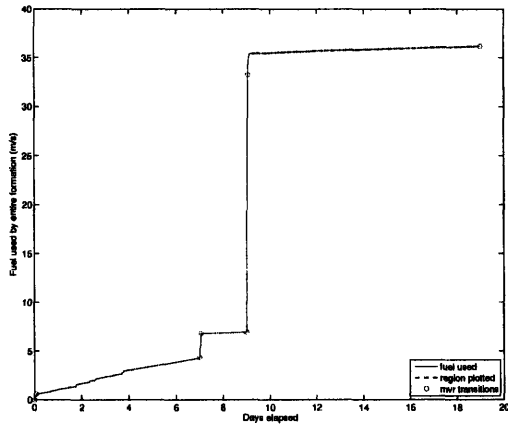


(c) LVLH Trajectory: in-track / radial

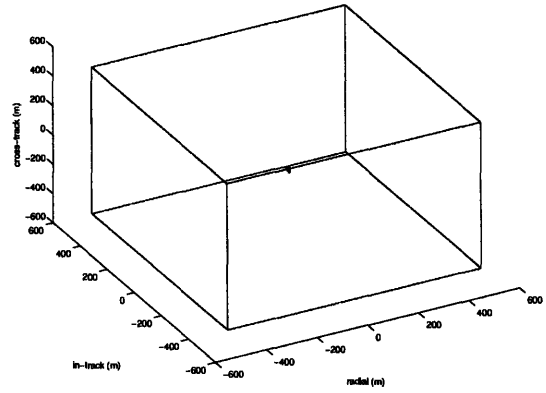


(d) LVLH Trajectory: in-track / cross-track

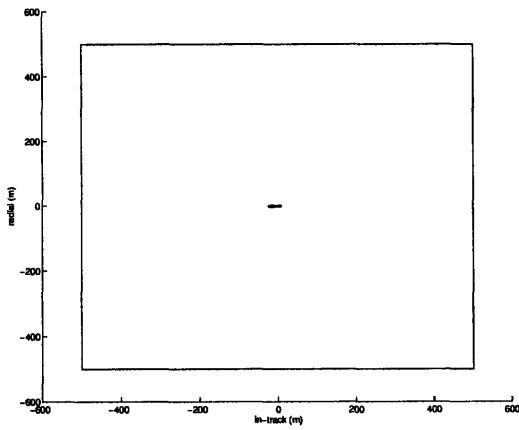
**Fig. 4-19:** Simulation #6: Stationkeeping in a passive aperture formation (500 m)



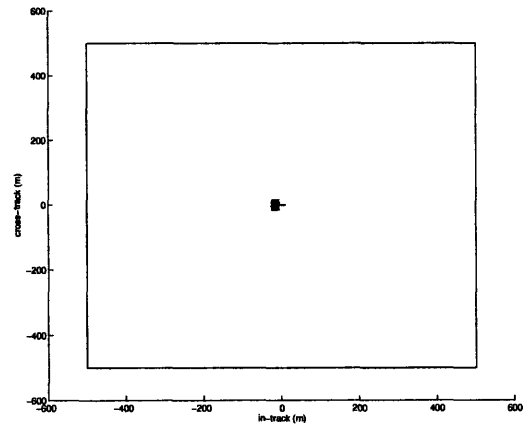
(a) Fuel Use



(b) 3D LVLH Trajectory



(c) LVLH Trajectory: in-track / radial



(d) LVLH Trajectory: in-track / cross-track

**Fig. 4-20:** Simulation #6: Stationkeeping in a passive aperture formation (5000 m)



# Chapter 5

## Safe Trajectories for Autonomous Rendezvous of Spacecraft

Autonomous spacecraft rendezvous is an enabling technology for many future space missions, but anomalies in recent flight experiments suggest that safety considerations will play an important role in the success of future missions. This chapter presents a method for online generation of safe, fuel-optimized rendezvous trajectories that guarantee collision avoidance for a large class of anomalous system behaviors. Next, the chapter examines the cost of imposing safety as a problem constraint and of additional constraints that guarantee infinite horizon passive collision avoidance while enabling future docking retries. Tradeoffs between passive and active approaches to safety are examined. A convex formulation of the collision avoidance algorithm is introduced and shown to provide much faster solutions with only a small additional fuel expense. Numerous examples using both rotating and non-rotating targets are presented to demonstrate the overall benefits of incorporating these safety constraints when compared to nominal trajectory design techniques.

### 5.1 Introduction

This chapter introduces a method for generating fuel-optimized rendezvous trajectories online that are safe with respect to a large class of possible spacecraft anomalies.

A safe trajectory is defined as an approach path that guarantees collision avoidance in the presence of a class of anomalous system behaviors. Similarly, a passive safe trajectory guarantees collision avoidance with no thrusting required for safety and an active safe trajectory requires that inputs be applied to keep the system safe in the event of a failure. Note that this definition of safety is more restrictive than guaranteeing nominal collision avoidance because it guarantees that no collisions will occur for a range of faults. In particular, for a passive safe trajectory, safety is guaranteed even if the chaser spacecraft cannot use thrusters, computers, or communications equipment. The rationale behind choosing a passive abort strategy is threefold: (a) passive abort can protect against a large set of possible system failures simultaneously; (b) an abort trajectory that does not require fuel use guarantees that remaining fuel will not be expended rapidly to increase spacecraft separation distance, thereby increasing the likelihood that future docking attempts can occur; and (c) passive abort guarantees thrusting will not be used in close proximity to the target during an anomaly, thereby eliminating the danger of plume impingement during an automatic safe-mode maneuver. Active safety is less restrictive than passive safety, but it requires that the types of any failures be identified in real-time and that some components of the control system remain operational so that a sequence of control inputs can be applied.

The following sections review a method for generating fuel-optimized trajectories from linearized relative dynamics and develop a novel approach for guaranteeing those trajectories will be safe. Several examples of safe trajectories generated for docking with both rotating and non-rotating target spacecraft establish that adding safety constraints does not result in significantly increased fuel use. Next, we examine additional constraints to guarantee desirable infinite horizon passive collision avoidance and ease of future docking attempts. To address online implementation considerations, a convex formulation of the safety problem is introduced that trades some performance for large computation reductions. An active form of safety is then considered as a means of reducing fuel costs while still remaining safe for a large set of possible failure modes.

## 5.2 Online Trajectory Optimization for Autonomous Rendezvous and Docking

A trajectory generated through online optimization can be designed by choosing the system inputs that produce that trajectory. For a linear system, methods for incorporating and propagating the effects of inputs are well-known. The trajectory optimization formulation in this section is presented in the context of linear time-invariant dynamics, but there is no inherent restriction in the formulation preventing the use of time-varying dynamics [84]. Given a chaser satellite whose state is  $\mathbf{x}_k$  at time  $k$ , the linearized dynamics of the system can be written as

$$\mathbf{x}_{k+1} = A_d \mathbf{x}_k + B_d \mathbf{u}_k \quad (5.1)$$

where  $A_d$  is the state transition matrix for a single time step,  $B_d$  is the discrete input matrix for a single time step, and  $\mathbf{u}_k$  is the input vector at step  $k$ . Typically, in a rendezvous situation, spacecraft would be in sufficiently close proximity to enable the use of the Hill-Clohessy-Wiltshire (HCW) equations [75], but GVE-based approaches [74] can be used for more widely separated situations. Examples in this chapter will use the HCW equations and hence the state  $\mathbf{x}$  is defined as

$$\mathbf{x} = \begin{bmatrix} x & y & z & v_x & v_y & v_z \end{bmatrix}^T \quad (5.2)$$

where  $x$ ,  $y$ ,  $z$ ,  $v_x$ ,  $v_y$ , and  $v_z$  are the positions and velocities of a chaser satellite in the radial, in-track, and cross-track axes, respectively, of an LVLH frame positioned on the center of gravity of a passive target vehicle. The input is defined as

$$\mathbf{u} = \begin{bmatrix} u_x & u_y & u_z \end{bmatrix}^T \quad (5.3)$$

where  $u_x$ ,  $u_y$ , and  $u_z$  are the inputs of the chaser vehicle in the axes indicated by the subscripts in the LVLH frame.

Given an initial state  $\mathbf{x}_0$ , the state at any future step  $k$  is [102]

$$\mathbf{x}_k = A_d^k \mathbf{x}_0 + \begin{bmatrix} A_d^{k-1} B_d & A_d^{k-2} B_d & \dots & A_d B_d & B_d \end{bmatrix} \begin{bmatrix} \mathbf{u}_0 \\ \vdots \\ \mathbf{u}_{k-1} \end{bmatrix} \quad (5.4)$$

$$= A_d^k \mathbf{x}_0 + \Gamma_k \begin{bmatrix} \mathbf{u}_0 \\ \vdots \\ \mathbf{u}_{k-1} \end{bmatrix} \quad (5.5)$$

where  $\Gamma_k$  is the discrete convolution matrix. Since the effects of the control on the states are readily expressed as linear combinations of the inputs, a linear optimization can be formed that optimizes the constrained control commands and constrains the states of the system. The cost function for this optimization will exclusively penalize fuel use. In an actual maneuver implementation, it may be preferable to optimize both the fuel use and the maneuver duration (see Ref. [77]), however in this chapter only fuel use will be considered to simplify presentation and cost comparisons. The cost of the optimization  $J$  is given by

$$J = \sum_{i=0}^{N-1} \|\mathbf{u}_i\|_1 \quad (5.6)$$

where the 1-norm cost is used to capture the expenditure of fuel used, which is proportional to acceleration and  $\Delta V$ , from axial thrusters. The optimal cost is then given by

$$J^* = \min_{\mathbf{u}_0, \dots, \mathbf{u}_{N-1}} \sum_{i=0}^{N-1} \|\mathbf{u}_i\|_1 \quad (5.7)$$

At each step  $k$ , it is possible to constrain the state at that time to lie inside a convex region

$$A_k \mathbf{x}_k \leq b_k \quad (5.8)$$

where  $A_k$  is a matrix and  $b_k$  is a vector that together capture a set of linear constraints on the state. Note that the costs and constraints in Eqs. 5.6 and 5.8 show an example

linear implementation of a trajectory optimization, but in general the same concepts that will be presented hold for nonlinear costs and constraints as well. Alternately, the state  $\mathbf{x}_k$  could be constrained to lie outside a region through the use of binary variables [61]

$$A_k \mathbf{x}_k \leq b_k + M \mathbf{y}_k \quad (5.9)$$

$$\|\mathbf{y}_k\|_1 \leq m - 1 \quad (5.10)$$

where  $\mathbf{y}_k$  is a vector whose elements are constrained to be 0 or 1, and  $M$  is a large number on the scale of values taken by elements of  $\mathbf{x}$ . This “Big M” method of collision avoidance works by allowing, at most, all but one of the collision avoidance constraints to be relaxed. A constraint is relaxed when the binary variable associated with it is set to 1, thereby making the right-hand side of the inequality very large and guaranteeing constraint satisfaction. Since at least one constraint is always guaranteed to not be relaxed, collision avoidance is assured (*e.g.*, knowing that one is outside of one side of a box is sufficient information to guarantee that one is not in the box).

The inputs at each time step can also be directly constrained using

$$\mathbf{u}_{\min_k} \leq \mathbf{u}_k \leq \mathbf{u}_{\max_k} \quad (5.11)$$

where  $\mathbf{u}_{\min_k}$  and  $\mathbf{u}_{\max_k}$  are vector bounds on the values of  $\mathbf{u}_k$ . Typically, the minimum thrust at all times would be  $-\mathbf{u}_{\max_k}$ . A detailed description of the full matrix forms used in linear trajectory optimizations for space vehicles can be found in Refs. [84] and [61].

This section has reviewed an approach for creating fuel-minimizing trajectories that satisfy time-varying position, velocity, and thrusting constraints. Applications of these constraint types can insure that a spacecraft remains inside a line-of-site cone, and arrives at a docking port position at a particular time with a particular speed range. In addition, the control authority available over the course of the trajectory can be varied according to desired pattern.

## 5.3 Safety Formulation

The trajectories generated by the constraints in Section 5.2 will satisfy docking requirements and use minimal fuel to arrive at a rendezvous location. However, as is typical of optimal paths, the trajectories will approach constraint boundaries and generally be sensitive to uncertain behavior. Refs. [73] and [77] describe computationally feasible methods of generating trajectories online that are robust to process and sensing noise expected under nominal operating conditions. That type of robustness to uncertainty is distinct from the definition of safety for off-nominal conditions considered herein. This section presents an approach for generating trajectories that are safe with respect to a class of system failures. While it would be desirable to avoid collisions and successfully complete docking in the presence of any system failure, it is unlikely that such a scenario is possible. Instead, a large subset of all possible failures is used, including guidance system shutdowns, which encompasses thruster failures, computer anomalies, and loss of sensing. The response to these types of failures would be a guidance system shutdown in which the chaser vehicle would go into a safe mode with all its thrusters turned off. Safety to this class of failures is called *passive abort safety*, because any rendezvous can be aborted using no thrusting. Passive abort safety guarantees collision avoidance for any failure that can be identified and responded to by disabling thrusters before the spacecraft trajectory is affected. This type of safety does not include failures in which a thruster fails on (see Section 5.8).

A consequence of passive abort is that if thrusters are disabled at any step  $T$ , counted from the start of the plan, during the trajectory implementation, then the thrusters will remain failed until the last step  $N$  of the plan. Clearly choosing  $N - T$  to be small (*i.e.*, only constraining steps toward the end of the horizon to be safe) puts fewer constraints on the trajectory optimization than a large value, but it assumes that more of the plan will be successfully implemented. Conversely, a large  $N - T$  is a more conservative approach to safety and more tightly constrains the optimization. The choice of which steps in the plan that are constrained to be safe depends on the

specific characteristics of the spacecraft and the mission requirements. The objective of this chapter is to present a systematic way of embedding the safety goals into the path planning problem so that the designer can evaluate the trade-offs associated with choosing  $T$ .

Note that enabling passive safety abort at the end of a trajectory can eliminate potential plume impingement conflicts that may result from last-minute safe-mode maneuvers. A further benefit of guaranteeing safety at the end of the trajectory is that it gives controllers an immediate safe exit from the docking procedure during the period when the spacecraft are in the closest proximity and there is the least time available to plan emergency maneuvers.

The discrete convolution approach used in Eq. 5.4 can be used to predict the state of the chaser at step  $k$  in the planning horizon in the event of a failure at time  $T$ , by considering all inputs after and including the input at time  $T$  to be zero

$$\mathbf{x}_{FT_k} = A_d^k \mathbf{x}_0 + \begin{bmatrix} A_d^{k-1} B_d & A_d^{k-2} B_d & \dots & A_d^{T-2} B_d & 0 \times A_d^{T-1} B_d & \dots & 0 \times A_d B_d & 0 \times B_d \end{bmatrix} \begin{bmatrix} \mathbf{u}_0 \\ \vdots \\ \mathbf{u}_{k-1} \end{bmatrix} \quad (5.12)$$

where  $\mathbf{x}_{FT_k}$  is the state of the chaser spacecraft at some step  $k < N$  in the planning horizon after a failure occurred at step  $T$ . The value of a failure state after the planning horizon is found through open-loop propagation of the state at time  $N$

$$\mathbf{x}_{FT_k} = A_d^{k-N} \mathbf{x}_{FT_N} \quad \text{for } k \geq N \quad (5.13)$$

Passive collision avoidance is achieved by adding constraints on the failure states of the spacecraft. Define the set of position states occupied by the target as  $\mathcal{T}_k$ , which can describe any polytopic region of position states, convex or otherwise. The safety horizon is the period of time after a failure during which both spacecraft are guaranteed not to collide. The safety horizon lasts  $S$  steps after the end of the nominal

trajectory and is guaranteed by introducing the set of constraints

$$\mathbf{x}_{FT_k} \notin \mathcal{T}_k \quad \forall k \in \{T + 1 \dots N + S\} \quad (5.14)$$

The constraints in Eq. 5.14 are then imposed for  $T \in \mathcal{F}$  where  $\mathcal{F}$  is the set of every potential failure time at which the system must guarantee collision avoidance for guidance shutdowns. The parameters to be chosen in this safety formulation are  $\mathcal{F}$  and  $S$ . This choice of parameters is highly dependent on the requirements of a particular space mission. The advantage of choosing to be safe for a large number of steps and for a long safety horizon is improved likelihood of preventing a catastrophic failure scenario in which the chaser and target collide. However, imposing many safety constraints greatly reduces the number of potential solution trajectories and as a result, likely reduces fuel efficiency. The tradeoff between safety and fuel efficiency is discussed in the scenarios in Sections 5.4.1 and 5.4.2.

## 5.4 Scenarios

The rendezvous and docking scenario to be examined in this chapter involves a target spacecraft being docked with and a chaser spacecraft maneuvering to achieve that docking. Figure 5-1 shows a target spacecraft that lies at the center of an local frame. A line-of-sight (LOS) cone protrudes from the target spacecraft and it is required that rendezvous remain within this line-of-sight cone for vision-based sensing. At the interface between the LOS cone and the target is a docking port (rectangular platform). In the rotating case (Figure 5-2) the axis of rotation is the long axis of the spacecraft and the rotation rate is orbital. The choice of rotation axis and rate was arbitrary and only enter the optimization through their effect on the time-varying constraints imposed for LOS requirements, docking, and safety. The LOS requirements are

$$A_{\text{LOS}_k} \mathbf{x}_k \leq b_{\text{LOS}_k} \quad \forall k = 1 \dots N \quad (5.15)$$



where  $A_{\text{LOS}_k}$  and  $b_{\text{LOS}_k}$  describe the states within the LOS cone at a step  $k$  in the planning horizon. The terminal constraint is

$$A_{\text{Term}_N} \mathbf{x}_N \leq b_{\text{Term}_N} \quad (5.16)$$

where  $A_{\text{Term}_k}$  and  $b_{\text{Term}_k}$  describe the states the spacecraft must occupy at the end of the planning horizon to achieve safe docking. These constraints can be both on position (*e.g.*, enter a region within reach of a grappling arm) and on velocity (*e.g.*, dock within a velocity range that produces acceptable stress on the docking port). In addition, time-varying bounds are introduced on the maximum thrusting levels in order to ensure large thrusts are not planned for the period immediately before docking. The safety constraints in Eq. 5.14 are imposed for the last quarter of the planning horizon. In the examples, an orbit with frequency  $n = 0.001$  rad/s is used and is discretized into 20 steps and the set of inputs that can fail is  $T \in \{14 \dots 19\}$ . The planning horizon is a full orbit. The chaser spacecraft, modeled after the mission in Ref. [81], has a mass of 45 kg and a maximum acceleration of  $10^{-3}$  m/s<sup>2</sup> during the first 17 steps of the plan and  $10^{-5}$  m/s<sup>2</sup> for the last 3 steps to prevent trajectory solutions with large terminal thrusts. In addition, the docking constraint specifies that the velocity of the spacecraft at the time of docking be less than 1 mm/s. In summary, the safety algorithm used in this section is

$$\begin{aligned} \min_{\mathbf{u}_0, \dots, \mathbf{u}_{N-1}} \quad & \text{Eq. (5.6)} & (5.17) \\ \text{s.t.} \quad & \text{Eq. (5.11)} \quad \forall k \in \{0, \dots, N-1\}, \\ & \text{Eq. (5.15)}, \\ & \text{Eq. (5.16)}, \\ & \text{Eq. (5.14)} \quad \forall T \in \mathcal{F} \end{aligned}$$

In these examples, the safety horizon is a full orbit. Any of the design parameters in the safety implementation can be easily adjusted and in practice one would likely conduct a simulation study or analysis [121] to find the best combination for

minimizing fuel use and guaranteeing feasible solutions.

#### 5.4.1 Case 1: Stationary Target Satellite

An optimized trajectory with no safety constraints for the stationary target case is shown in Figure 5-3. The initial trajectory to the docking port roughly corresponds to a two impulse V-bar (in-track) [67] approach. The nominal trajectory is marked with  $\bullet$  and the failure trajectories with  $\times$ . Failure trajectories, the paths followed by the spacecraft in the event of a guidance shutdown, are shown for last five possible inputs. Several of the failure trajectories overlap, a condition which corresponds to the nominal input at a step already being set to zero thrust. All of the failure trajectories clearly impact the target spacecraft. Figure 5-4 shows the same rendezvous situation for trajectories generated with safety constraints. In this case, none of the failure trajectories impact the target spacecraft. An apparent violation of the constraint boundary is visible in the lower left-hand corner of the figure. This type of corner violation is possible in the MILP framework, because only the discrete points are constrained, not the trajectory between discrete points. Reference [82] gives an approximation for the amount a constraint should be enlarged to ensure that any violations will not intersect the actual constrained region. As in the case without safety, several of the failure trajectories overlap. The fuel costs (measured in  $\Delta V$ ) of the trajectory with no safety guarantees and the trajectory with safety are 1.29 mm/s and 1.91 mm/s, respectively. Hence, in this case, imposing safety results in a 48% increase in fuel use. To put these numbers in context, an optimized approach constrained to follow a V-bar trajectory (strictly in-track) would use 37.7 mm/s of fuel.

An approximate method for over-bounding the optimized numbers would be to consider an approach based on introducing in-track drift and arriving at the docking port after a full planning horizon, with no other constraints. In this case, the planning horizon is a full orbit, with no initial radial offset and no initial velocity, an initial thrust in the in-track direction will introduce a secular drift into the relative orbit.

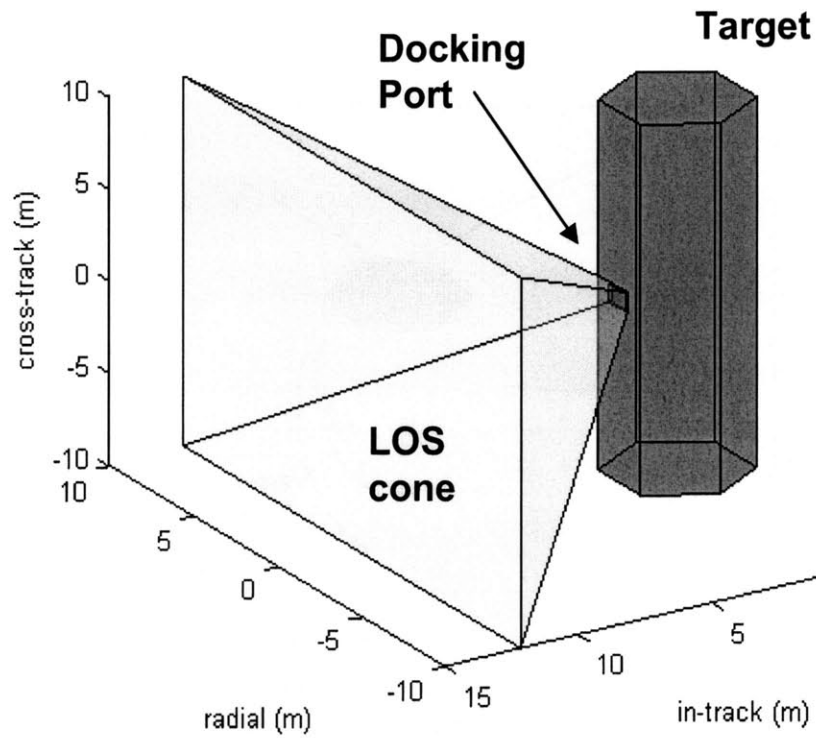


**Fig. 5-1:** Target spacecraft and docking configuration

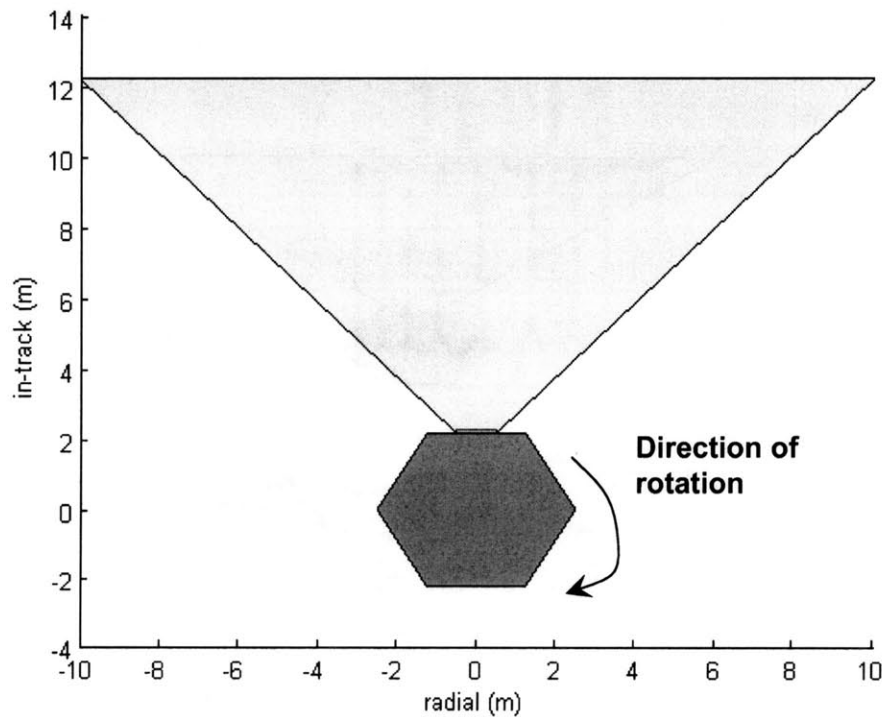


**Fig. 5-2:** Radial/in-track view of rotating target spacecraft and docking configuration

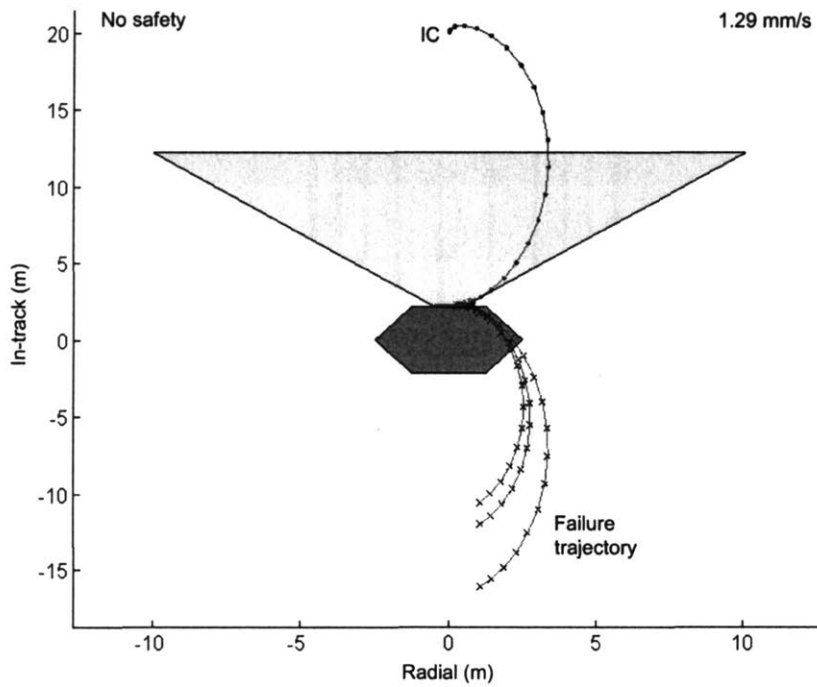


**Fig. 5-3:** Nominal trajectory planning with no safety: constraint violations occur for trajectory failures. The nominal trajectory is marked with ● and the failure trajectories with ×. The failure trajectories all result in collisions with the target spacecraft.

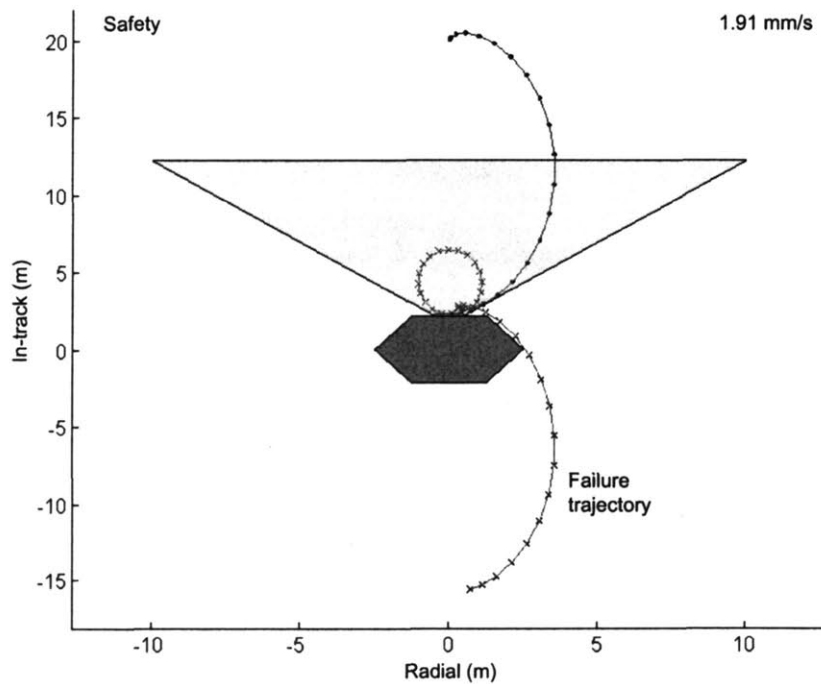


**Fig. 5-4:** Trajectory planning with safety: failed trajectories deviate around the target spacecraft, preventing collision. The nominal trajectory is marked with ● and the failure trajectories with ×.

Over the course of an orbit this secular drift causes the in-track position to shift by

$$\Delta y = \Delta v_y 6\pi/n \quad (5.18)$$

according to the in-track solution for Hill's equations [106]. For the example in this section, the amount of fuel required for this maneuver would be 0.93 mm/s. An approximate upper bound on the fuel number could be obtained by forming a constrained problem similar to the LP, but forced to follow a strict in-track (V-bar) trajectory. If the 2-norm of fuel use is minimized as an approximation instead of the correct 1-norm metric and the thruster inputs are not constrained, this problem can be solved using a pseudo-inverse. By constraining the radial position state at each step  $k$  in the planning horizon to be zero and the final in-track position to lie on the edge of the docking port, the following equality constraints are formed

$$A_Q \begin{bmatrix} \mathbf{u}_0 \\ \vdots \\ \mathbf{u}_{k-1} \end{bmatrix} = b_Q \quad (5.19)$$

with

$$A_Q = \begin{bmatrix} H_x \Gamma_1 & 0 & \dots & 0 & 0 \\ H_x \Gamma_2 & 0 & \dots & 0 & \\ H_x \Gamma_{N-1} & 0 & & & \\ H_x \Gamma_N & & & & \\ H_y \Gamma_N & & & & \end{bmatrix}, \quad b_Q = \begin{bmatrix} -H_x A_d^1 \mathbf{x}_0 \\ -H_x A_d^2 \mathbf{x}_0 \\ \vdots \\ -H_x A_d^N \mathbf{x}_0 \\ -H_y A_d^N \mathbf{x}_0 + y_{\text{des}} \end{bmatrix} \quad (5.20)$$

where  $H_x$  is a row vector that extracts the scalar radial component,  $H_y$  is a row vector that extracts the scalar in-track component, and  $y_{\text{des}}$  is the desired in-track component at step  $N$ . This form has  $N + 1$  constraints and  $3N$  input variables to choose. The trajectory that minimizes the 2-norm of the input vectors and meets

those simple constraints is given by the pseudo-inverse solution [83] of

$$\begin{bmatrix} I_{3N} & A_Q^T \\ A_Q & 0_{N+1} \end{bmatrix} \begin{bmatrix} \mathbf{u}_0 \\ \vdots \\ \mathbf{u}_{k-1} \\ \mathbf{z} \end{bmatrix} = \begin{bmatrix} 0_{3N,1} \\ b_Q \end{bmatrix} \quad (5.21)$$

where  $\mathbf{z}$  is a vector of  $N + 1$  Lagrange multipliers,  $I_p$  is a  $p \times p$  identity matrix,  $0_q$  is a  $q \times q$  matrix of zeros, and  $0_{p,1}$  is a  $p \times 1$  vector of zeros. The fuel cost of the trajectory found using this method is 39.1 mm/s, which is very close to the optimized cost of following a strict V-bar trajectory.

#### 5.4.2 Case 2: Docking Port Perpendicular to Spin Axis

The rotating docking port case uses an identical formulation to the stationary case, however, the constraint regions are time-varying. In particular, in the stationary case,  $A_1 = A_2 = A_k \forall k = 1 \dots N$ , but to formulate the rotating problem, the  $A_k$  and  $b_k$  matrices must be formed for each step of the planning horizon based on the rotation rate and, for more general cases, the motion of the target, the docking port, and the line-of-sight cone. One simple way to generate these constraints is to represent each side of an avoidance region as a plane that is specified by a sample of its constituent points. These points will remain in a plane through any reorientation of the original constraint. Thus, the rotated constraint side can be found by applying rotation matrices [80] to the points and then forming the equation of a new plane, which can then be used as an inequality constraint. The translation and rotation motion of the target spacecraft should be well-characterized through observation or cooperation before starting a rendezvous maneuver, thereby allowing the prediction of its future trajectory to be used for forming constraints. All trajectory propagations of the target spacecraft used to create constraints are formed before the rendezvous maneuver is optimized. As a result, the propagation can be carried out using any method appropriate for the specific online implementation (*e.g.*, simple linear propagation,

high accuracy numerical integration). Robustness to uncertainty in target motion can be accommodated by guaranteeing that any optimized trajectory is valid for a range of representative target initial conditions [84].

For the rotation case examined in this section, the optimized trajectory no longer matches a two-impulse V-bar approach, but is instead forced to thrust regularly to stay within the rotating LOS cone. Figure 5-5 shows this optimized trajectory with no safety constraints. As in the stationary case, in the absence of safety constraints, the nominal trajectory collides with the target in the event of guidance shutdowns. An alternate form with safety constraints prevents collisions for failures occurring in the last quarter of the trajectory (Figure 5-6). Note that in Figure 5-6, the safe trajectory appears to pass through the target, but in actuality it avoids collision because of the rotational motion of the target. The fuel costs without safety constraints and with safety constraints are 55.3 mm/s and 56.4 mm/s, respectively. In this case, the fuel cost of imposing safety as a constraint is only a 2% increase over the nominal cost. As in the non-rotating case, the increase in fuel needed to include the safety constraints is minimal and the advantage is guaranteed collision avoidance for passive abort in the last quarter of the nominal path. Another example (safe trajectory in Figure 5-7) using a target rotating at 3/2 orbital rate required 68.7 mm/s of fuel with no safety constraint and 69.1 mm/s of fuel with a safety constraint.

## 5.5 Probability of Collision

To judge the effectiveness of the safety algorithm introduced in Section 5.3, define a probability of collision metric,  $P_{col}$ , which is the probability of a failure at any time step during a maneuver resulting in a collision between the target and chaser spacecraft. The probability of collision is given by

$$P_{col} = \sum_{i=1}^N P(\text{failure at } i \mid \text{no failure before } i) \cdot P(\text{collision occurs} \mid \text{failure at } i) \quad (5.22)$$

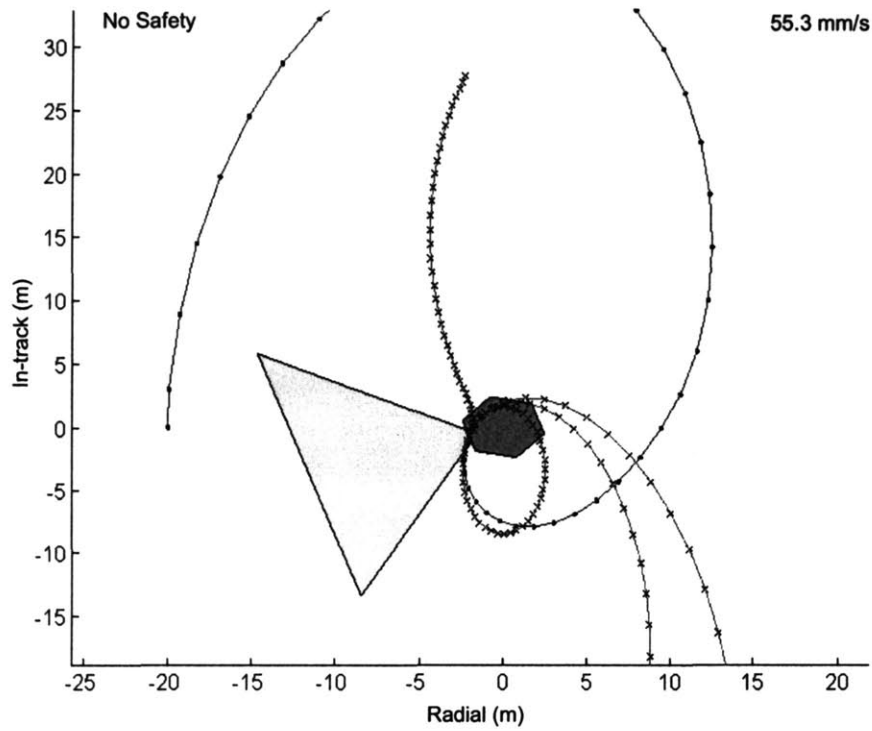


**Fig. 5-5:** Nominal trajectory planning with no safety in the rotating case: constraint violations occur for trajectory failures.

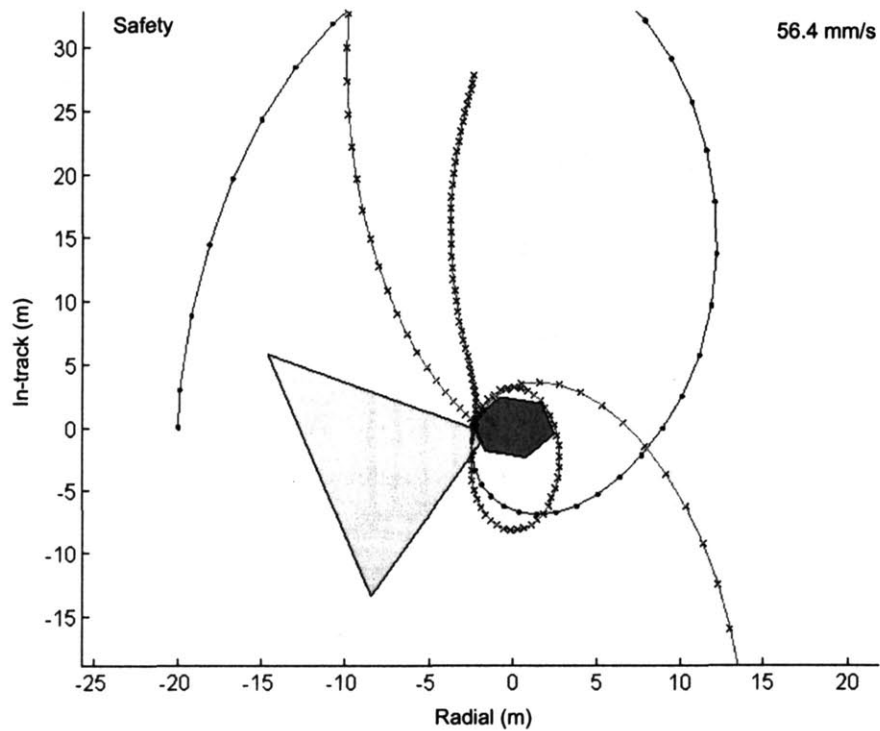


**Fig. 5-6:** Trajectory planning with safety in the rotating case: failed trajectories deviate around the target spacecraft, preventing collision



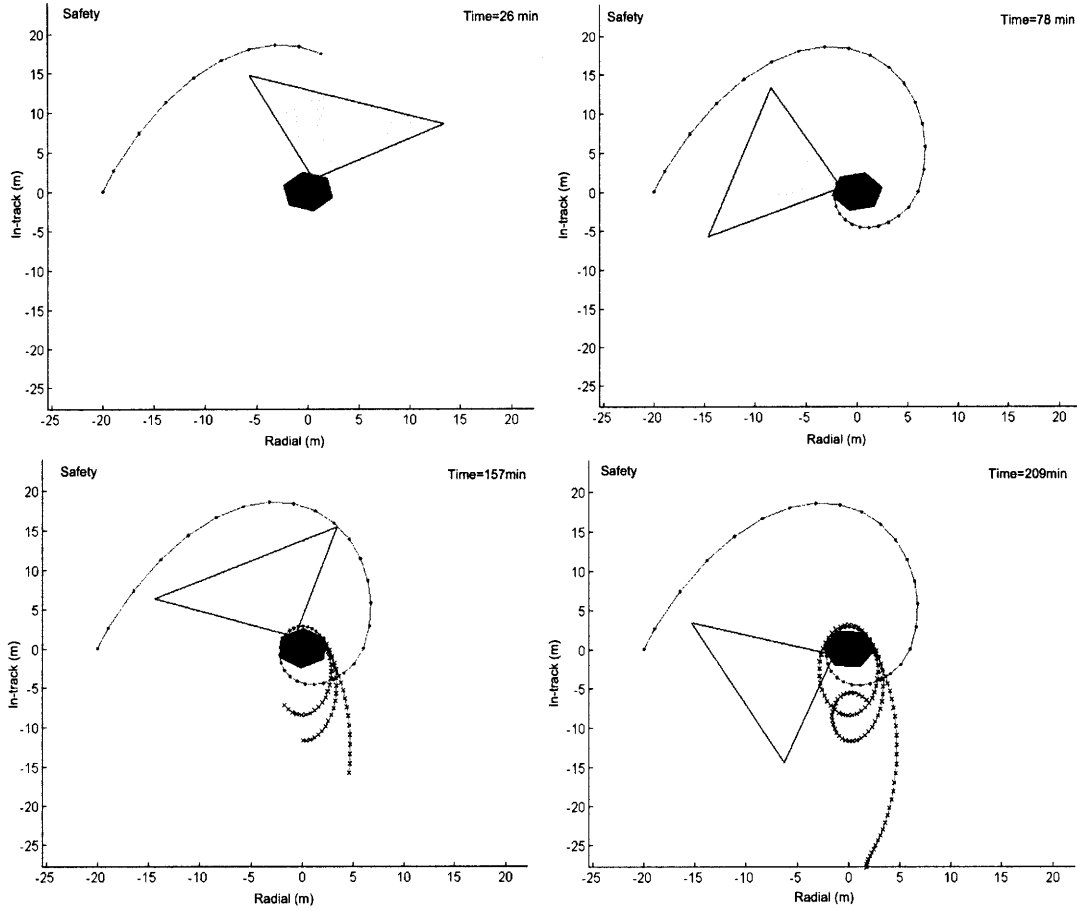


**Fig. 5-7:** Trajectory planning with safety in the fast rotating ( $3/2$  orbital speed) case. The maneuver  $\Delta V$  cost with safety is  $69.1 \text{ mm/s}$ .

where the probability  $P(\text{collision occurs} \mid \text{failure at } i)$  is either 1 or 0 and is evaluated by examining the trajectory followed if thrusters are disabled at step  $i$  and checking for future collisions. Assuming that the probability of a failure at any step in the trajectory is  $f$ , then

$$P(\text{failure at } i \mid \text{no failure before } i) = (1 - f)^{i-1} f \quad (5.23)$$

Using the metric  $P_{col}$ , the effectiveness of the safety approach was investigated by creating a series of safe trajectories starting from different initial conditions near the target. The initial condition positions were chosen to create a range of nearby starting points. The velocity vector for each position was chosen according to the conditions in

Ref. [68] to create a *safety circle*. This creates a situation where each rendezvous trajectory begins from a safe, invariant orbit within range of a final approach rendezvous trajectory.

Figures 5-8 and 5-9 show the values of  $P_{col}$  for full-orbit optimized final approach trajectories, discretized into  $N = 20$  steps. The trajectories are generated using  $\mathcal{F} = \emptyset$  (no safety constraints) and  $\mathcal{F} = \{9, \dots, 19\}$  (guaranteed safe for the last 10 steps of the trajectory), respectively, where  $f = 0.001$ . These plots show that without safety, the probably of collision for a given rendezvous trajectory tends to fall between 0.005 and 0.015. However, the addition of safety for half of the trajectory brings the collision probability for most of the trajectories below 0.001. The same optimizations were performed and analyzed for a range of other  $\mathcal{F}$  ranges and the results are summarized in Figure 5-10. The dashed line indicates an overbound,  $\bar{P}_{col}$ , for the maximum possible probability of collision, which is the case where every failure during the course of the trajectory when safety is not guaranteed (i.e., steps not in  $\mathcal{F}$ ) would result in a collision, which is given by

$$\sum_{\{0, \dots, N-1\} \setminus \mathcal{F}} P(\text{failure at } i \mid \text{no failure before } i) \quad (5.24)$$

The line marked with  $\blacklozenge$  shows the largest probability encountered in the optimized trajectories for all initial conditions considered. This is equivalent to finding the maximum height ( $z$  value) in a plot of the type in Figure 5-9 for each different set  $\mathcal{F}$  used to create Figure 5-10. The minimum (line marked by  $\bullet$ ) shows that in each case, there were some initial conditions that did not result in collision, regardless of the steps in  $\mathcal{F}$ . In those cases, the fuel-optimal rendezvous trajectory is safe. The average  $P_{col}$  (solid line), equivalent to averaging the probability heights over an area of the type in Figure 5-9, followed a similar trend to the largest  $P_{col}$ , but was significantly lower. This indicates that although some initial conditions are particularly prone to collision, on average the collision probabilities are significantly improved by safety and in no case has the addition of safety made collisions more likely than in the fuel-optimal case ( $\mathcal{F} = \emptyset$ ). Furthermore, for this particular case, the trends indicate that

guaranteeing more than the last five steps safe does not significantly decrease the probability of a collision. This conclusion would be valuable from a mission planning perspective, because each additional plan step that is guaranteed safe represents a tradeoff in which computation time and nominal fuel use potentially increase.

Eq. 5.24 indicates that the overbound  $\bar{P}_{col}$  decreases with increasing length of the safe region (i.e., fewer steps in  $\mathcal{F}$ ). For the purposes of worst-case safety guarantees, the overbound could be used as an analytic rule-of-thumb for mission design studies.

## 5.6 Invariant Formulation

The safety formulation introduced in Section 5.3 only guarantees passive collision avoidance until the end of the safety horizon. In previous examples, the safety horizon has been fixed at one orbit. Figure 5-13 shows a stationary-target case where a collision would occur soon after the end of a one orbit safety horizon. If the safety horizon is extended to multiple orbits, the resulting failure trajectories will tend to either drift away from target spacecraft or create invariant orbits that neither drift toward nor away the target spacecraft. Drifting away from the target orbit is preferable to collision, however it means that fuel will need to be expended to bring the chaser near the target for any future docking attempts. Furthermore, the longer controllers wait to cancel the drift, the farther apart the two spacecraft will become, thereby creating an additional timing consideration during an anomalous event. It is preferable for the chaser to drift into an invariant orbit that is near the target, but can never, under the assumptions of Keplerian dynamics, collide. The preference for invariant failure orbits can be captured by constraining a state in the failure trajectory at some step  $k$  to be the same one full orbit after  $k$  using a linear state transition matrix to propagate the state forward. This constraint is written

$$\mathbf{x}_{FT_{k+1}} = A_d^{N_o} \mathbf{x}_{FT_k} \quad \text{for } k \geq T \quad (5.25)$$

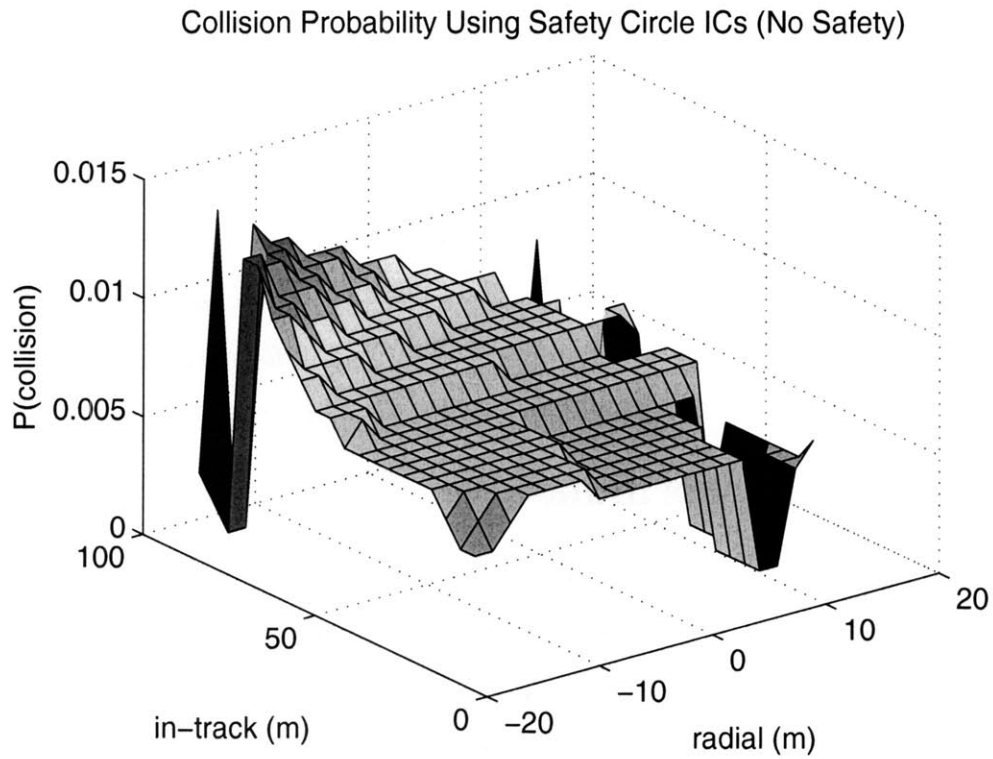


**Fig. 5-8:** Probability of a collision occurring for a range of initial conditions with  $\mathcal{F} = \emptyset$  (No safety guarantees).

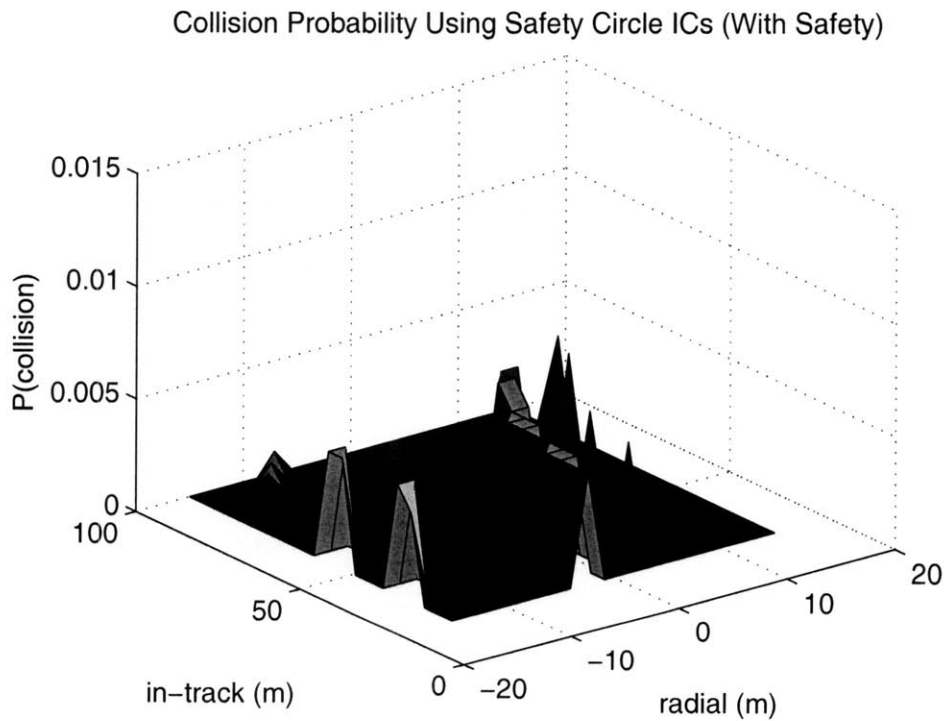


**Fig. 5-9:** Probability of a collision occurring for a range of initial conditions with  $\mathcal{F} = \{9, \dots, 19\}$  (latter half of trajectory guaranteed safe)

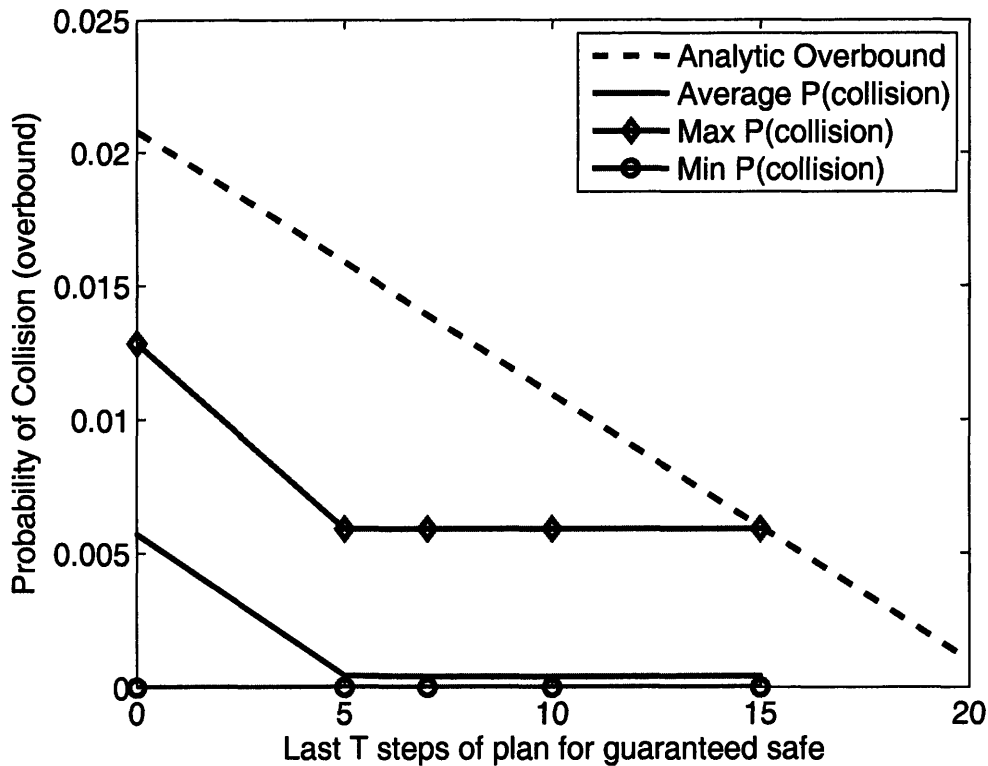
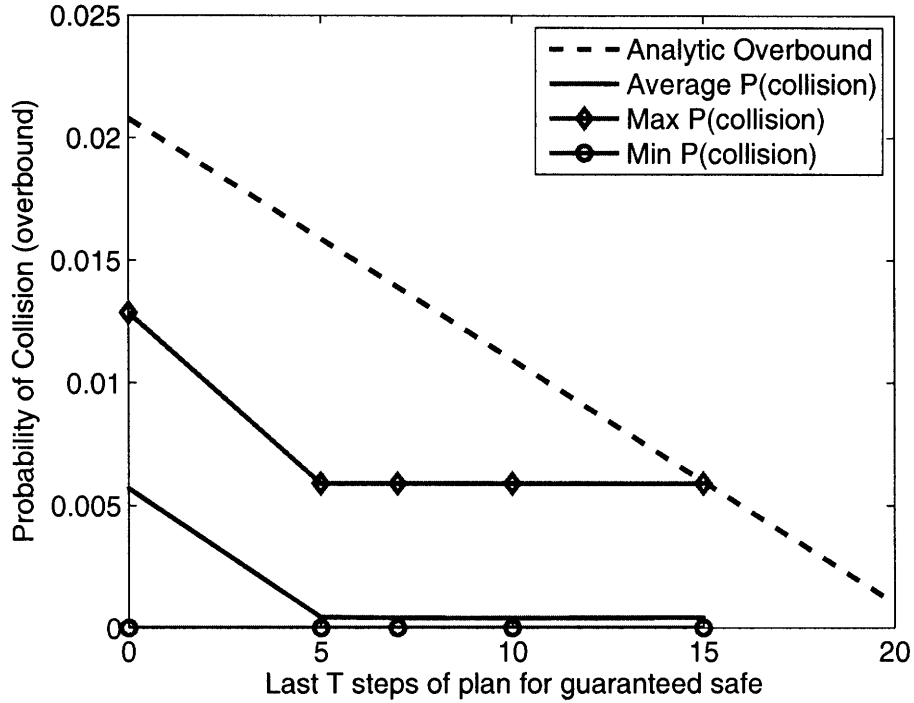


Fig. 5-10: Probability of collision occurring for various values of  $\mathcal{F}$

where  $N_o$  is the number of steps in an orbit. By imposing this constraint for all possible failures times in  $\mathcal{F}$ , all failure orbits are guaranteed to be invariant with respect to the target. The safety algorithm in Eq. 5.17 is only altered by the addition of the new constraints in Eq. 5.25.

Figure 5-14 shows the same rendezvous problem from Figure 5-13, but with additional invariance constraints on failures occurring in the last quarter of the rendezvous trajectory. Imposing invariance constraints yields circular trajectories relative to the target, which are traversed once per orbit with no fuel expenditure. Some of the six failure trajectories shown in Figure 5-14 overlap each other where the optimized trajectory did not require fuel inputs. The safe trajectory with no invariance constraint used 3.4 mm/s of fuel and the safe trajectory with invariance used 7.1 mm/s of fuel. In this case, the invariance constraints have roughly doubled fuel requirements. However, this tradeoff may be beneficial when there is a danger of collision after the safety horizon or when the fuel requirements for canceling drift after a failure



**Fig. 5-11:** Fuel required for rendezvous maneuvers for various values of  $\mathcal{F}$

are taken into account. For this case, the lower-bound estimated fuel numbers from Eq. 5.18 predict 1.4 mm/s of fuel required and the strict V-bar approach solution from Eq. 5.21 predicts 61.4 mm/s of fuel use, which is close to the optimized V-bar solution which requires 59.2 mm/s. The cost of using an optimized rendezvous trajectory with no safety constraints is 3.1 mm/s, making safety only 1.3% more expensive. The cost of using a strict V-bar approach is roughly 18 times more expensive than the optimized safe approach and 8.6 times more expensive than the optimized safe invariant approach. Thus, when compared to the cost of using a standard non-optimized maneuver, the fuel premium for using safety with invariance is small.

The examples using invariance constraints presented in this section used Hill's dynamics [75], meaning that the particular type of invariance achieved is effectively equivalent to constraining the relative semimajor axes of the target and chaser spacecraft to be zero. Alternate equations of motion exist which model additional orbital perturbations. For example, the dynamics presented in Chapter 2 could be used for

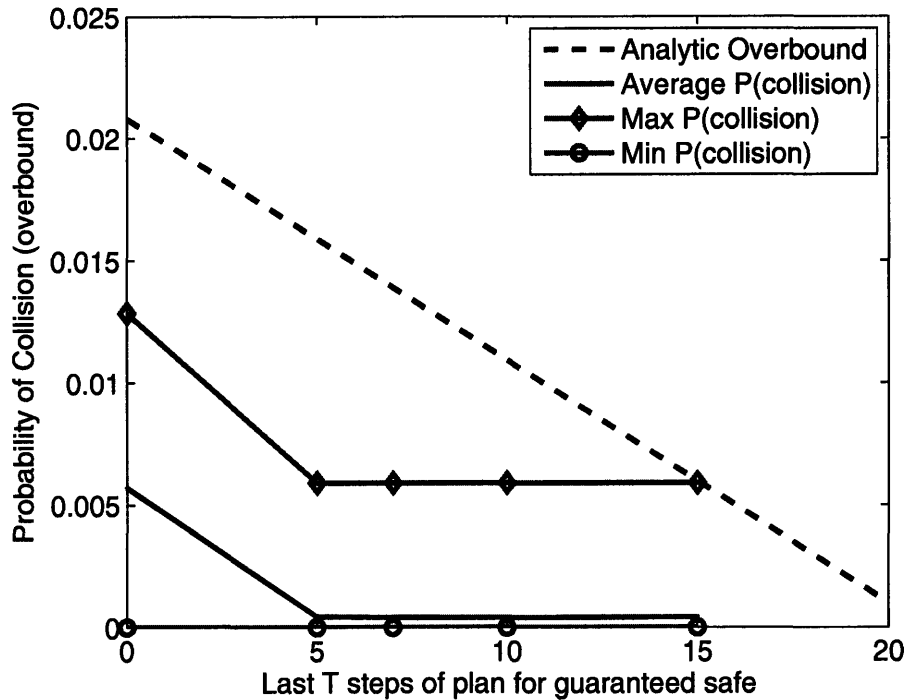


**Fig. 5-12:** Amount of time required to optimize rendezvous trajectories for various values of  $\mathcal{F}$

rendezvous and docking trajectory generation to create invariant orbits that account for the effects of differential  $J_2$ . Likewise, the effects of differential drag can also be taken into account using the method in Ref. [84].

## 5.7 Convex Safety Formulation

The safety constraints introduced in Section 5.3 guaranteed that the chaser states would not collide with the target in the event of a failure. The collision avoidance in those constraints is accomplished using binary variables to capture the nonconvexity of the problem. The problem with binaries was formulated as a Mixed-Integer Linear Program (MILP) and posed to a commercial solver. Solving a MILP can be a computationally intensive task and the time required to solve tends to grow very quickly with the number of discrete variables in the problem [111]. The trajectory shown in Figure 5-4 required 8.92 seconds to solve on a 3 GHz computer. That problem had

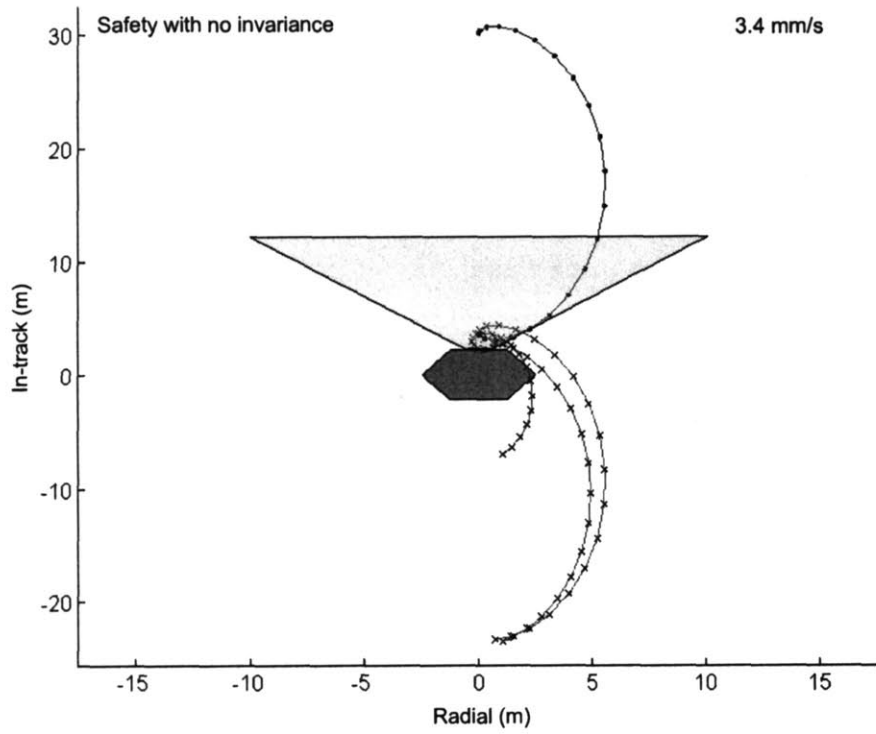


**Fig. 5-13:** Case where end of safety horizon is followed by a collision.

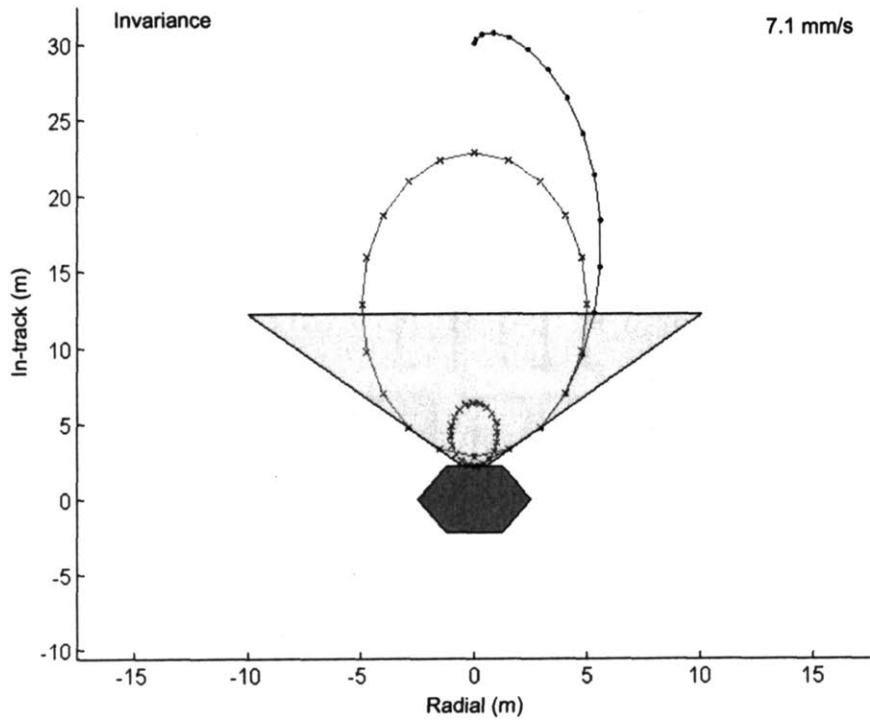


**Fig. 5-14:** Use of invariance constraints guarantees infinite horizon passive collision avoidance and prevents failure trajectories from drifting away from the target.



a 20 step safety horizon, an avoidance region with 8 sides, and six inputs that were safe in the event of guidance shutdown. Each avoidance region side requires a binary variable at each step of the safety horizon and those constraints are included 6 times, each propagating forward from a different failed thruster step. Thus, implementing collision avoidance over the safety horizon for that simple example required 960 binary variables. Solving the same trajectory for a two orbit safety horizon required 24.6 seconds. Using the same horizon duration with a finer discretization step would further increase the required computation time. It is likely that online implementations would need to solve with limited computer resources and that a nonconvex implementation may be impractical for implementations requiring short discretization steps.

An alternative to the nonconvex formulation is to use a more restrictive form of collision avoidance that is convex. Instead of requiring the chaser to remain outside an avoidance region, the failure trajectories are instead constrained to remain inside a region that is known to not contain the target. This is similar to the type of convex passively safe trajectory examined for rotating satellite capture in Ref. [70], however the approach in this chapter explicitly minimizes fuel use. Figure 5-15 shows an example of the optimized trajectory for the rendezvous problem in Figure 5-4, but instead solved as a linear program (LP) using the convex safety constraints

$$H_y \mathbf{x}_{FT_k} \geq y_{\min} \quad \forall k \in \{T + 1 \dots N + S\} \quad (5.26)$$

where  $y_{\min}$  is the maximum in-track position of the target spacecraft. The nonconvex case results in failure trajectories that are not permitted in the convex case and as a result, there is a fuel penalty for imposing convexity. Using the convex formulation in Eq. 5.26 does not require altering the basic safety algorithm in Eq. 5.17. Instead, only the target geometry, given by the set  $\mathcal{T}$  in Eq. 5.14, needs to be altered to ensure that its complement is convex. The nonconvex case requires 1.5 mm/s of  $\Delta V$  and the convex case requires 3.7 mm/s. The more restrictive area in which failure trajectories can lie caused the required fuel to increase by more than a factor of 2. However, the

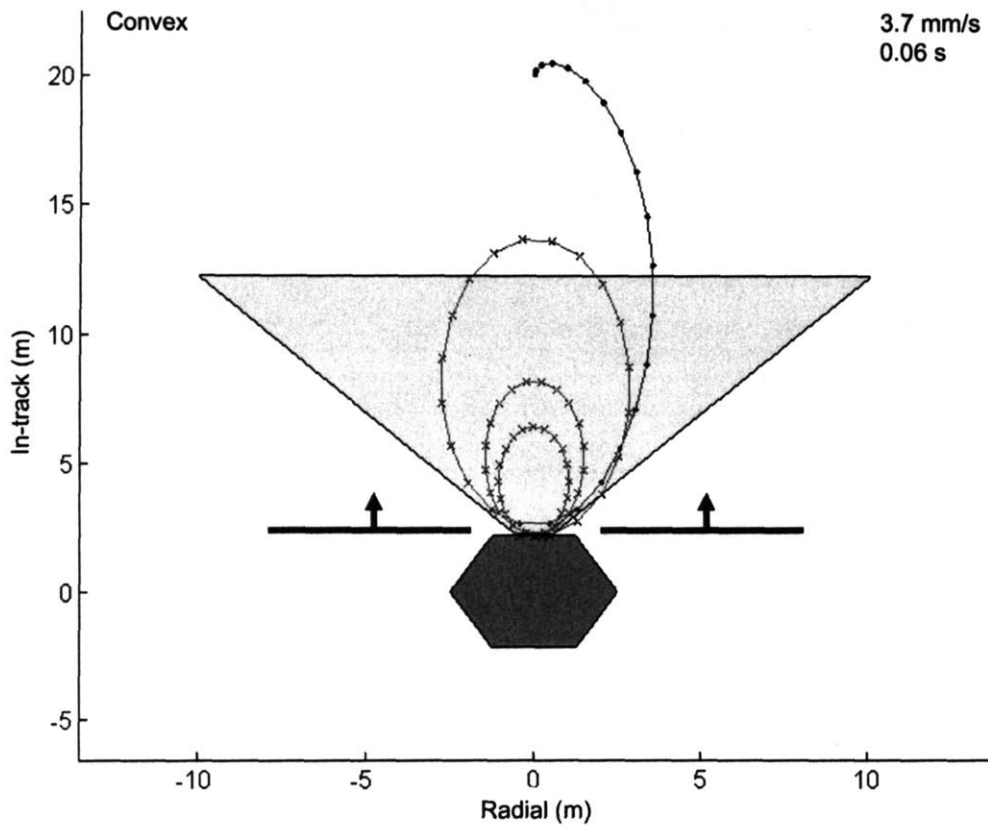


**Fig. 5-15:** Collision avoidance for failure trajectories using convex constraints indicated by arrows.

amount of time required to compute the convex trajectory was only 0.06 seconds, a decrease from the nonconvex case by a factor of 150. In cases where it is impractical to dedicate significant computational resources to planning, it may be desirable to trade the fuel optimality of the more general MILP formulation for the speed of the LP formulation. In addition, the convex solution is often similar to the invariant given in Eq. 5.25. For the example in Figure 5-15, the trajectory cost when invariance and convexity are imposed is 4.2 mm/s, which is the same as the cost of using invariance in the fully nonconvex problem.

## 5.8 Active Safety

An alternative to passive safety is *active safety*, in which a set of thruster inputs is applied to ensure rendezvous safety. The active response is a set of input sequences that is used instead of passive safety. The *safe input sequence* can be designed a priori (*e.g.*, thrust in-track, thrust radially) and chosen in real-time or optimized at the time the nominal rendezvous maneuver is optimized. In either case, the safe inputs are known at all times during the maneuver and no additional optimization is required in the event of a failure. The advantages of active safety over passive safety are significant: by allowing thrusting in the event of a failure, a significantly larger portion of the nominal trajectory can be guaranteed safe and the fuel costs of guaranteeing the safety of the nominal trajectory are reduced. Passively safe trajectories can be considered a subset of active safe trajectories in which the active input sequence has no thrusting. The primary limitation of active safety is that it provides safety guarantees for a smaller set of possible system malfunctions than passive safety. In the case of passive safety, any anomaly in which the thrusters can be disabled can be made safe. Safety guarantees resulting from an active safety trajectory require that some thrusters continue to work properly and in the correct directions in the event of a failure. An extension at the end of this section will show how active safety can be modified to provide safety guarantees for single thruster failures.

To create an active safety constraint, the optimization from Section 5.3 is altered to allow the possibility of using a safe input sequence by introducing an additional discrete convolution matrix. Rewriting Eq. 5.12 for a predetermined safe input se-

quence

$$\begin{aligned}
\mathbf{x}_{FT_k} = & A_d^k \mathbf{x}_0 + \begin{bmatrix} A_d^{k-T-1} B_d & \dots & A_d B_d & B_d \end{bmatrix} \begin{bmatrix} \mathbf{v}_0 \\ \vdots \\ \mathbf{v}_{k-T-1} \end{bmatrix} \\
& + \begin{bmatrix} A_d^{k-1} B_d & A_d^{k-2} B_d & \dots & A_d^{T-2} B_d & 0 \times A_d^{T-1} B_d & \dots & 0 \times A_d B_d & 0 \times B_d \end{bmatrix} \begin{bmatrix} \mathbf{u}_0 \\ \vdots \\ \mathbf{u}_{k-1} \end{bmatrix}
\end{aligned} \tag{5.27}$$

where  $T < k < N$ ,  $k - T < N_s$ ,  $N$  is the number of steps in the nominal plan, and  $N_s$  is the number of steps in the safe input sequence. If  $k \leq T$  then  $\mathbf{x}_{FT_k} = \mathbf{x}_k$  because no potential failure could have occurred at that time. Equation 5.27 can be written more generally as

$$\mathbf{x}_{FT_k} = \begin{cases} \Gamma_k S(T, k) \mathbf{U}_k + A_d^k \mathbf{x}_0 + \Gamma_{k-T} S(k - T, N_s) \mathbf{V}_k, & T < k \leq N, \\ & T < k - T \leq N_s \\ A_d^{k-N} \Gamma_N S(T, N) \mathbf{U}_N + A_d^k \mathbf{x}_0 + \Gamma_{k-T} S(k - T, N_s) \mathbf{V}_k, & k > N, k - T \leq N_s \\ \Gamma_k S(T, k) \mathbf{U}_k + A_d^k \mathbf{x}_0 + A_d^{k-N_s} \Gamma_{N_s} \mathbf{V}_{N_s}, & k \leq N, k - T > N_s \\ A_d^{k-N} \Gamma_N S(T, N) \mathbf{U}_N + A_d^k \mathbf{x}_0 + A_d^{k-N_s} \Gamma_{N_s} \mathbf{V}_{N_s}, & k > N, k - T > N_s \end{cases} \tag{5.28}$$

where  $k$  is the time step that the failure trajectory is propagated forward to,  $S(q, N_q) = \text{diag}(\mathbf{I}_{3(q)}, \mathbf{0}_{3(N_q - q)})$ ,  $\mathbf{I}_n$  is an  $n \times n$  identity matrix,  $\mathbf{0}_n$  is an  $n \times n$  matrix of zeros, the decision variables for the nominal input are the vector  $\mathbf{U}_k^T = [ \mathbf{u}_0^T \dots \mathbf{u}_{k-1}^T ]$ , and the predetermined safe input sequence  $\mathbf{V}_k^T = [ \mathbf{v}_0^T \dots \mathbf{v}_{k-1}^T ]$ . The possible ranges in Equation 5.28 correspond to the steps before the nominal plan has ended and before the end of the safe input sequence ( $k \leq N$ ,  $k \leq k - T$ ), the times after the nominal plan has ended and before the end of the safe input sequence ( $k > N$ ,  $k \leq k - T$ ), times before the nominal plan has ended and after the end of the safe input sequence ( $k \leq N$ ,  $k > k - T$ ), and the times after the both the nominal plan and the safe

input sequence have ended ( $k > N$ ,  $k > k - T$ ). All four cases must be considered in order to allow for safe input sequences that are longer or shorter than the nominal plan length. Active safety can be guaranteed by introducing the set of constraints

$$\mathbf{x}_{FT_k} \notin \mathcal{T}_k \quad \forall k \in \{T + 1, \dots, N + S\} \quad (5.29)$$

The set of constraints in Eq. 5.29 is applied for each step  $T$  at which safety should be guaranteed in the event of a failure.

An alternate approach to active safety where the safe input sequence is optimized online can be implemented by moving the safe input sequence  $\mathbf{V}_{N_s}$  into the decision vector of Eq. 5.28

$$\mathbf{x}_{FT_k} = \begin{cases} \begin{bmatrix} \Gamma_k S(T, k) & \Gamma_{k-T} S(k - T, N_s) \end{bmatrix} \begin{bmatrix} \mathbf{U}_k \\ \mathbf{V}_k \end{bmatrix} + A_d^k \mathbf{x}_0, & \begin{array}{l} T < k \leq N, \\ T < k - T \leq N_s \end{array} \\ \begin{bmatrix} A_d^{k-N} \Gamma_N S(T, N) & \Gamma_{k-T} S(k - T, N_s) \end{bmatrix} \begin{bmatrix} \mathbf{U}_N \\ \mathbf{V}_{N_s} \end{bmatrix} + A_d^k \mathbf{x}_0, & k > N, k - T \leq N_s \\ \begin{bmatrix} \Gamma_k S(T, k) & A_d^{k-N_s} \Gamma_{N_s} \end{bmatrix} \begin{bmatrix} \mathbf{U}_N \\ \mathbf{V}_{N_s} \end{bmatrix} + A_d^k \mathbf{x}_0, & k \leq N, k - T > N_s \\ \begin{bmatrix} A_d^{k-N} \Gamma_N S(T, N) & A_d^{k-N_s} \Gamma_{N_s} \end{bmatrix} \begin{bmatrix} \mathbf{U}_N \\ \mathbf{V}_{N_s} \end{bmatrix} + A_d^k \mathbf{x}_0, & k > N, k - T > N_s \end{cases} \quad (5.30)$$

such that the safe input sequence  $\mathbf{V}_{N_s}$  is optimized at the same time as the nominal rendezvous trajectory. Active safety uses the same safety algorithm in Eq. 5.17, but with Eq. 5.14 replaced by Eq. 5.29 using the active failure trajectory given by Eq. 5.28 for *a priori* known safe input sequences or Eq. 5.30 for safe input sequences optimized online.

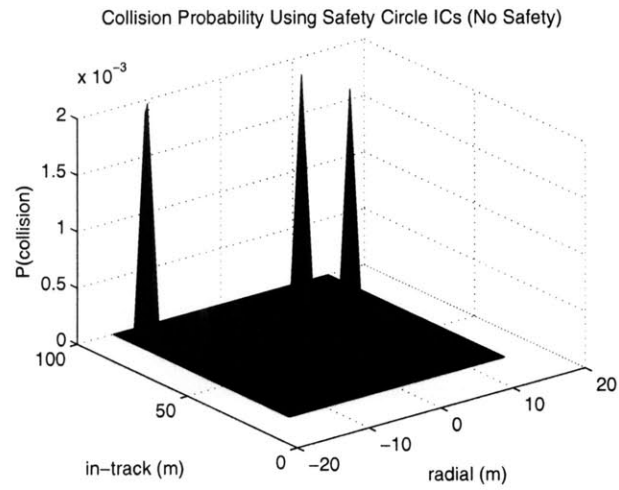
The implementation of an active safe trajectory would be similar to that of a safe trajectory. Before entering the trajectory, the spacecraft is assumed to be in a nominal state (*i.e.*, all systems are functioning correctly). If a fault has not yet

occurred, the spacecraft follows the nominal trajectory, which is given by  $\mathbf{U}_N$ . If a fault occurs during a step that has been guaranteed to be safe in the event of that fault, then the spacecraft begins using the safe input sequence. For the duration of the safe input sequence, the chaser and target spacecraft are guaranteed to not collide. If the invariance constraints in Section 5.6 are used, safety can be guaranteed for any time horizon over which the dynamics are valid.

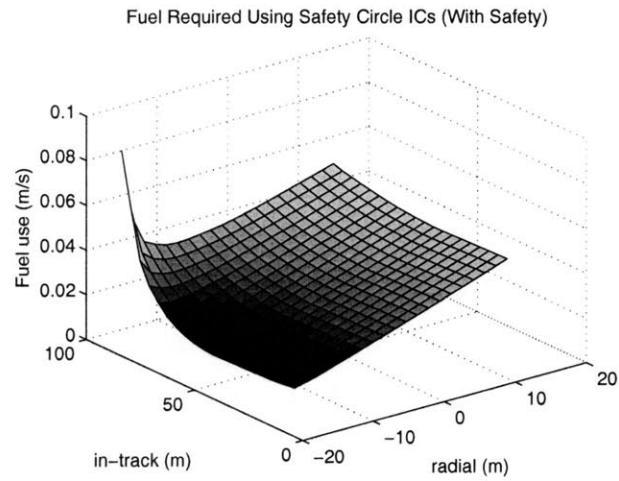
### 5.8.1 Examples

A stochastic analysis of the type performed in Section 5.5 was conducted using active safety, guaranteeing safety for the last 3/4 of the nominal trajectory ( $\mathcal{F} = \{4, \dots, 19\}$ ). The maps of collision probability, fuel use, the trajectory computation time are shown in Fig. 5-16. The results indicated that the average collision probability for failures accounted for by active safety was reduced to  $1.96 \times 10^{-5}$  from 0.0057 for the optimal unsafe case and  $4 \times 10^{-4}$  for the passive safety case ( $\mathcal{F} = \{4, \dots, 19\}$ ). The average fuel use across the grid is 27.4 mm/s and the average time required to optimize a trajectory is 1.5 seconds.

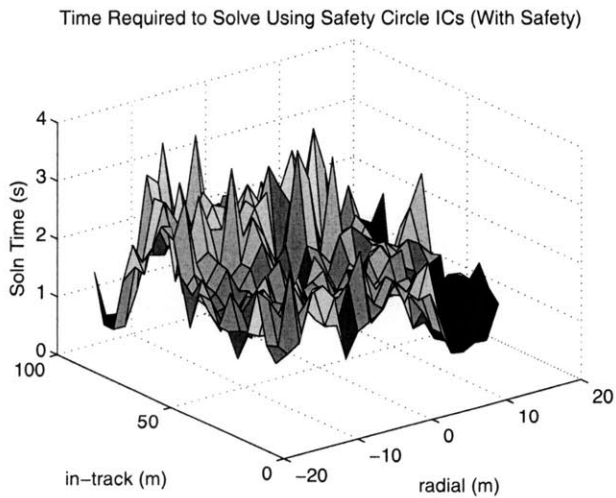
The differences between the active safety approaches are demonstrated in Figures 5-17-5-20. Figure 5-17 shows an active safe rendezvous trajectory beginning from a safety circle holding orbit. In this case, the safe input sequence  $\mathbf{V}$  has been arbitrarily chosen to be an orbit of constant thrusting at  $10^{-6}$  m/s<sup>2</sup> in the  $-x$  direction of an LVLH frame centered on target. The last three quarters of the rendezvous trajectory have been guaranteed through constraints to be actively safe. In the figure, the nominal rendezvous trajectory (line marked with  $\bullet$ ) shows the planned rendezvous maneuver which will be followed in no failures occur. Each portion of the trajectory marked with  $\triangle$  shows a possible path followed by the chaser in the event that the safe input sequence is used. Constraints guarantee safe collision avoidance for the entire red portion of the trajectory, however, no safety guarantees exist for the trajectory after the safe input sequence is enacted. The trajectories marked by  $\times$  show the how the path drifts after the end of each safe trajectory. In several cases, the drifting path would result in a collision at some time in the future. To ensure colli-



(a) Probability of Collision



(b) Fuel Use (mm/s)



(c) Trajectory Optimize Time

**Fig. 5-16:** Active safety demonstrated for a range of initial conditions with  $\mathcal{F} = \{4, \dots, 19\}$  (latter 3/4 of trajectory guaranteed safe)

**Table 5.1:** Comparison of various types of safe rendezvous trajectories. Fuel costs in mm/s.

	No Safety, Nominal	Passive Safety	Passive Safety, invariant	Active Safety, <i>a priori</i>	Active Safety, <i>a priori</i> invariant	Active Safety, optimized	Active Safety, optimized, invariant
Nominal Cost	13.67	14.21	19.32	13.84	18.17	13.67	17.58
Safety Cost	0	0	0	6.28	6.28	0.76	2.14
P(collision)	0.012	0	0	0	0	0	0

sion avoidance, Figure 5-19 shows an active safe trajectory optimized from the same initial conditions, but with the invariance constraint from Eq. 5.25 imposed. In this case, a failure at any step in the last three quarters of the nominal trajectory would result in the chaser spacecraft entering a safe, invariant trajectory near the target spacecraft. Figures 5-19 and 5-20 show the optimized active safe trajectories using the constraints in Eq. 5.30 without and with invariance constraints, respectively.

Table 5.1 compares various approaches for creating rendezvous trajectories with and without safety using the same initial conditions as the examples in Figures 5-17-5-20. The first row refers to the fuel cost (mm/s) of implementing the nominal rendezvous trajectory. The second row gives the cost of implementing a full safe input sequence (mm/s). The last row gives the probability of collision for the trajectory using the method introduced in Section 5.5. The columns compare the fuel-optimal path with no safety to the passive safety path and paths using active safety. The active safety columns labeled *a priori* use the predefined safe input sequence approach in Eq. 5.28 and the columns labeled *optimized* use the approach in Eq. 5.30. The columns marked invariant also use the invariance constraints in Eq. 5.25. It is notable that for the example in the table, the probability of collision for the fuel-optimal trajectory (*i.e.*, no safety) is 0.012, but the addition of passive or active safety to the problem causes the probability to drop to zero. Note that this probability is predicated on the assumption that a failure is identified within a time-step of its occurrence and that the thrusters can be turned off (for passive safety) or used nominally (for active safety).



Passive safety requires more fuel for rendezvous than the case without safety, however, active safety with an optimized safe input sequence has the same cost as the fuel-optimal case. In the cases where invariance is imposed as a constraint, the fuel cost using active optimized safety is lower than the passive invariance case, but not as low as the optimal trajectory. Thus, for these initial conditions, both the nominal trajectory and the safe abort trajectory must be shaped to achieve active invariance. The cost of safety for the nominal and passive safety trajectories is zero, because those cases do not consider safety and do not require thrusting for failures, respectively. In each active safety case, the safety cost is very small compared to the cost of the nominal trajectory, indicating that it should be possible to implement active safety on a space mission without significantly increasing the  $\Delta V$  budget.

### 5.8.2 Active Safety for Thruster Failures

The active safety approach in Eq. 5.30 can be modified to guarantee safety for cases of individual thruster failure by optimizing multiple safe input sequences. Each safe input sequence is constrained to only use a single thruster direction, or alternately, a single thruster assuming that thrusters act through the center of gravity. This guarantees that if only one thruster fails, another safe trajectory which does not use the failed thruster still exists. Thus, in a system with at least two thrusters, any single thruster failure to the off state will be in the set of possible system failures covered by active safety. Likewise, if thrusters in the system can be used to cancel each other (*e.g.*, a system with axial thrusters) then this active safety extension can also be used in the presence of thruster-on failures. In that case, the thruster opposite that which failed can be used to cancel erroneous thrusting while a thruster in another direction can be used to enact a preplanned safe input sequence.

Modifying Eq. 5.30 to include multiple safe input sequences yields

$$\mathbf{x}_{FT_k} = \left\{ \begin{array}{l} \left[ \begin{array}{ccc} \Gamma_k S(T) & \Gamma_k S(T-k)H_x & \mathbf{0} \\ \Gamma_k S(T) & \mathbf{0} & \Gamma_k S(T-k)H_y \end{array} \right] \begin{bmatrix} \mathbf{U}_k \\ \mathbf{V}_k^x \\ \mathbf{V}_k^y \end{bmatrix} + A_d^k \mathbf{x}_0, & \begin{array}{l} k \leq N, \\ k - T \leq N_s \end{array} \\ \left[ \begin{array}{ccc} A_d^{k-N} \Gamma_N S(T) & \Gamma_k S(T-k)H_x & \mathbf{0} \\ A_d^{k-N} \Gamma_N S(T) & \mathbf{0} & \Gamma_k S(T-k)H_y \end{array} \right] \begin{bmatrix} \mathbf{U}_k \\ \mathbf{V}_k^x \\ \mathbf{V}_k^y \end{bmatrix} + A_d^k \mathbf{x}_0, & \begin{array}{l} k > N, \\ k - T \leq N_s \end{array} \\ \left[ \begin{array}{ccc} \Gamma_k S(T) & A_d^{k-N} \Gamma_{N_s} H_x & \mathbf{0} \\ \Gamma_k S(T) & \mathbf{0} & A_d^{k-N} \Gamma_{N_s} H_y \end{array} \right] \begin{bmatrix} \mathbf{U}_k \\ \mathbf{V}_k^x \\ \mathbf{V}_k^y \end{bmatrix} + A_d^k \mathbf{x}_0, & \begin{array}{l} k \leq N, \\ k - T > N_s \end{array} \\ \left[ \begin{array}{ccc} A_d^{k-N} \Gamma_N S(T) & A_d^{k-N} \Gamma_{N_s} H_x & \mathbf{0} \\ A_d^{k-N} \Gamma_N S(T) & \mathbf{0} & A_d^{k-N} \Gamma_{N_s} H_y \end{array} \right] \begin{bmatrix} \mathbf{U}_N \\ \mathbf{V}_{N_s}^x \\ \mathbf{V}_{N_s}^y \end{bmatrix} + A_d^k \mathbf{x}_0, & \begin{array}{l} k > N, \\ k - T > N_s \end{array} \end{array} \right. \quad (5.31)$$

where  $\mathbf{V}_{N_s}^x$  is the safe input sequence of only  $x$ -direction inputs,  $\mathbf{V}_{N_s}^y$  is the safe input sequence of only  $y$ -direction inputs, and  $H_x$  and  $H_y$  are matrices that extract only elements of  $\Gamma$  pertaining to  $u_x$  inputs and  $u_y$  inputs, respectively. The active safety algorithm remains the same, but the failure trajectory used in formulating Eq. 5.29 must be propagated using Eq. 5.30 instead of Eqs. 5.28 or 5.30.

Figure 5-21 shows an example trajectory using the multi-solution active safety form in Eq. 5.31 to solve the safe rendezvous problem for the initial conditions used in Table 5.1. The left side of the figure shows the nominal rendezvous trajectory and the safe trajectories that would be used in the event of a failure in the  $\pm y$  direction thruster (resulting from using  $\mathbf{V}_{N_s}^x$ ). The right side shows the same nominal trajectory, but the safe trajectories shown correspond to  $\mathbf{V}_{N_s}^y$ . In this case, a single optimization has produced two sets of safe input sequences, either valid at any time

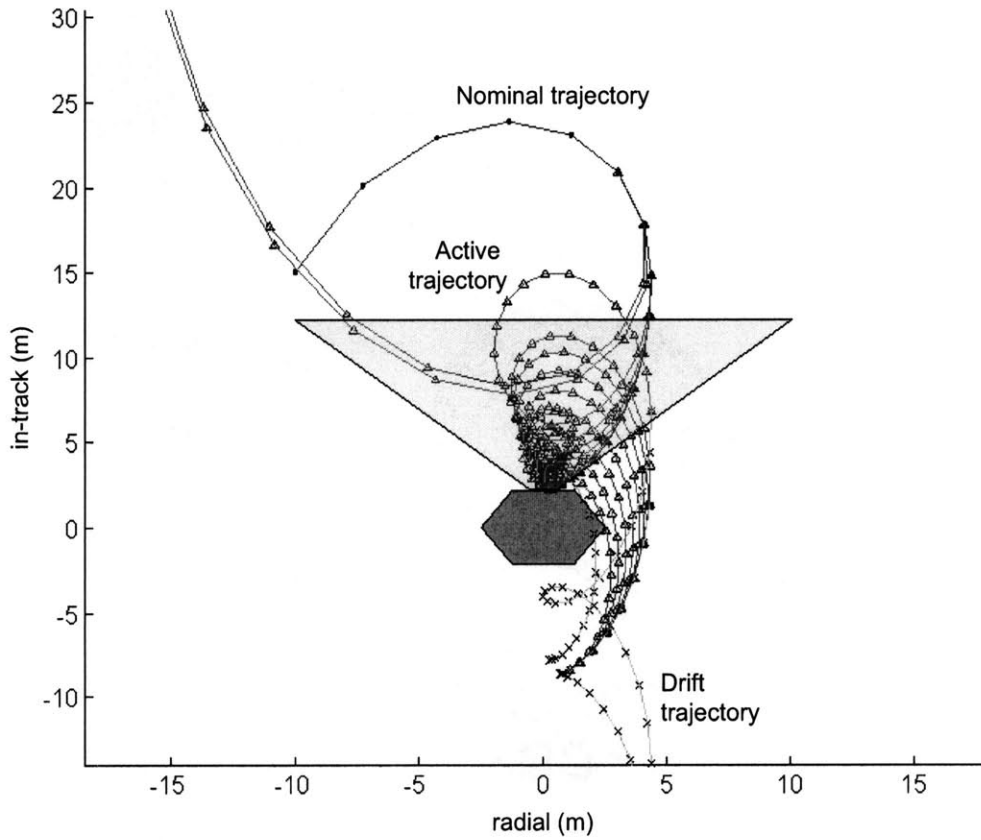


Fig. 5-17: Rendezvous trajectories using active safety.

step with guaranteed safety. The safe input sequence solutions are

$$\mathbf{V}_{N_s}^x = \begin{bmatrix} -4.56 \times 10^{-6} \\ 0 \\ 0 \\ 0 \end{bmatrix} \quad \mathbf{V}_{N_s}^y = \begin{bmatrix} 3.06 \times 10^{-6} \\ 0 \\ 0 \\ 0 \end{bmatrix} \quad (5.32)$$

The nominal trajectory in this case requires 13.67 mm/s of fuel, equivalent to the fuel-optimal, “unsafe” trajectory. The cost of safety for implementing  $\mathbf{V}_{N_s}^x$  is 1.43 mm/s and for  $\mathbf{V}_{N_s}^y$  is 0.96 mm/s, which follows the trend of low safety trajectory costs observed in Table 5.1.

The algorithm for using passive safety only requires that thrusters be disabled in the event of a failure and active safety only requires that a predetermined safe input sequence be used. The implementation algorithm for the modified active safety formu-

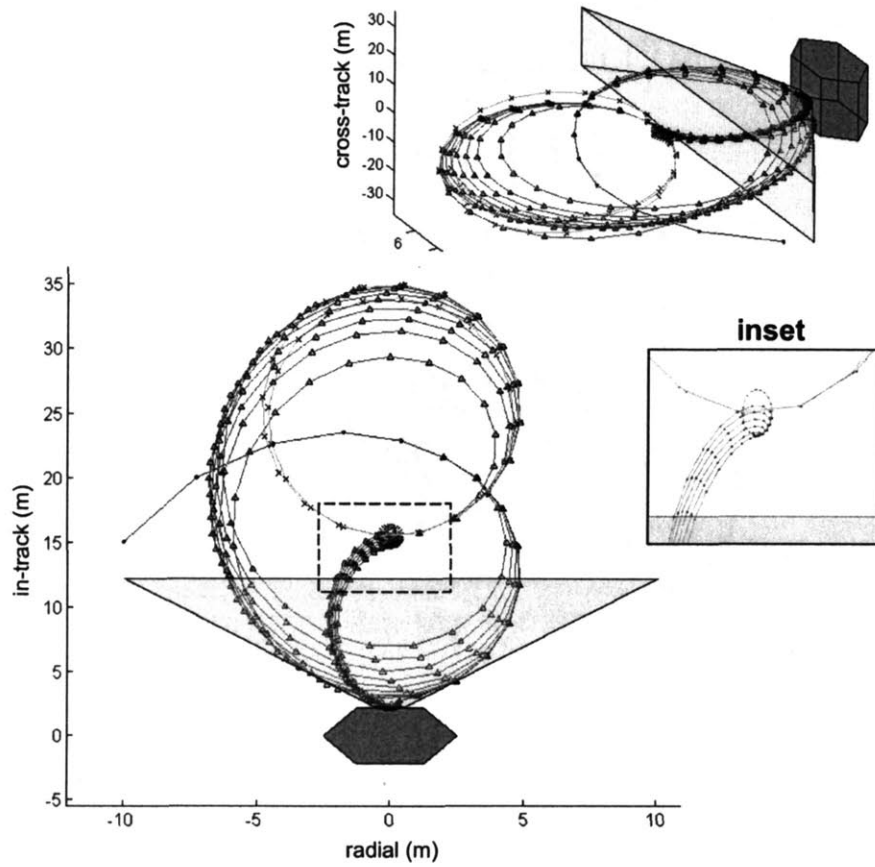


**Fig. 5-18:** Rendezvous trajectories using active safety with invariance constraints.

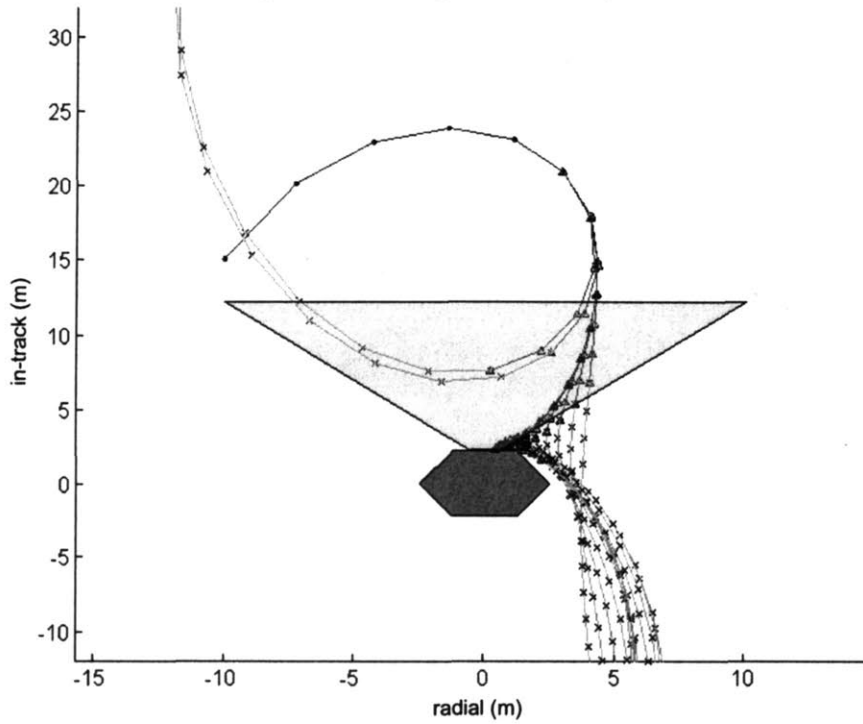


**Fig. 5-19:** Rendezvous trajectories using optimized active safety.

lation in this section requires an additional input from the spacecraft fault detection and isolation system which indicates the type of fault. In the case of thruster failure, this would also need to include which thruster failed and the nature of the failure. This additional information enables the active safety implementation to choose the appropriate safe input sequence to use.

### 5.8.3 Mitigating Impact of Process Noise and Navigation Error

The safety formulation in Equations 5.12 and 5.14 assumes that the state of the chaser spacecraft relative to the target spacecraft is precisely known. In practice, this relative state is only known to within the accuracy provided by the navigation system. Likewise, the propagation used in Eq. 5.12 is only as accurate as the linear dynamics used to formulate that equation, since the actual vehicle would be subject to nonlinear dynamics, and disturbances from effects such as drag,  $J_2$ , separation distance, and eccentricity. Equation 5.12 can also be rewritten to enable time-varying dynamics or an additional vector of modeled disturbances can be added to the problem without increasing the complexity of the resulting optimization [84]. This permits a more sophisticated dynamics model to be used, which could reduce some of the effects of modeling error [120]. To account for navigation error, the constraints in Eq. 5.14 can be made robust by posing them multiple times for a representative sampling of possible initial states that cover the space of likely navigation errors. Reference [115] introduces such an approach and an algorithm for minimizing the effect of robustness constraints on the size of the resulting optimization. Figure 5-22 shows a safe trajectory optimized using the same initial conditions as those used to create Table 5.1. In the figure, active safety with guaranteed collision avoidance for the last 3/4 of the trajectory is used with the addition of robustness to initial condition uncertainty. In this case, the initial velocity of the chaser is only known to within  $\pm 0.75$  mm/s in the radial direction and  $\pm 0.0002$  mm/s in the in-track direction. The resulting trajectory requires 13.84 mm/s nominally and the safe input

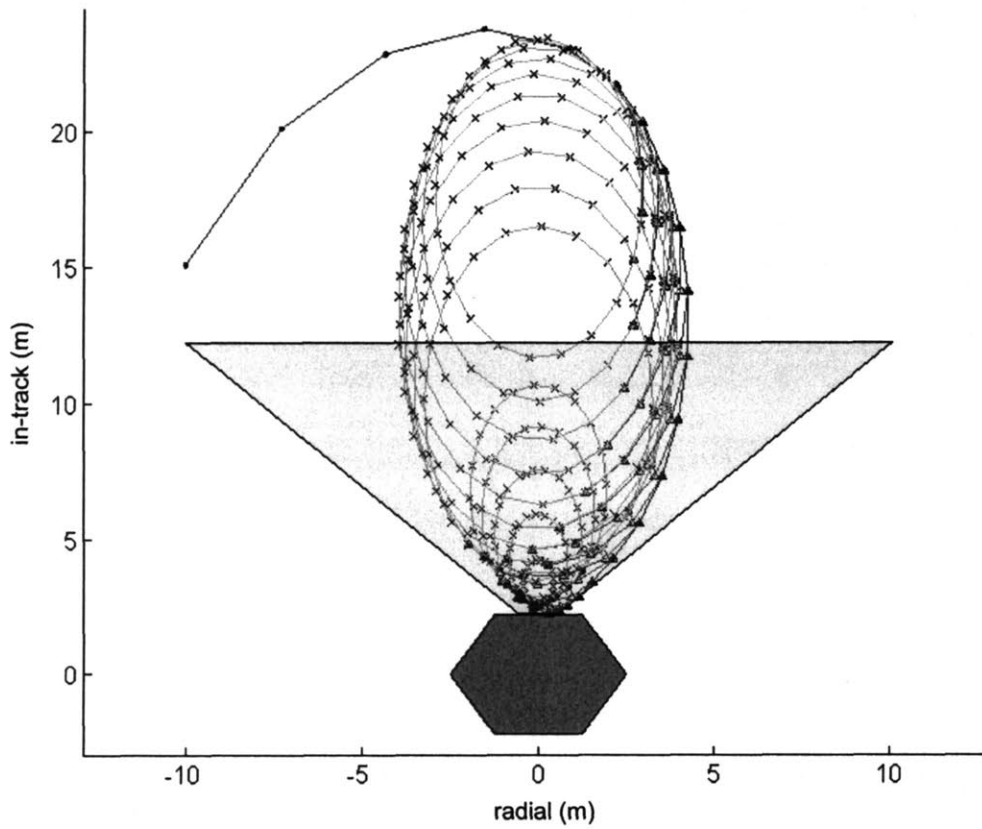


**Fig. 5-20:** Rendezvous trajectories using optimized active safety with invariance constraints.

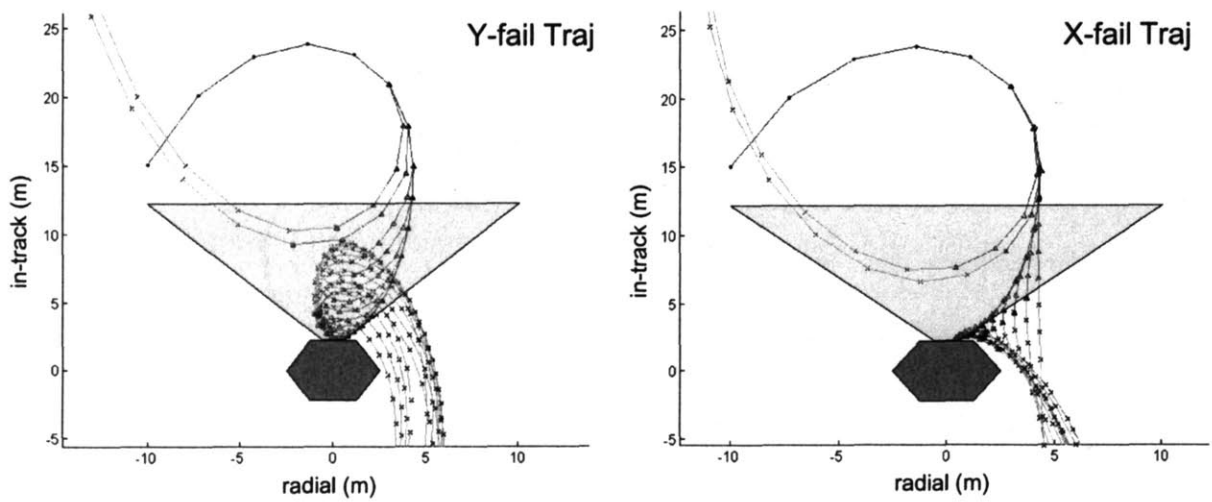


**Fig. 5-21:** Rendezvous trajectories for using active safety optimized for two possible thruster failure directions.

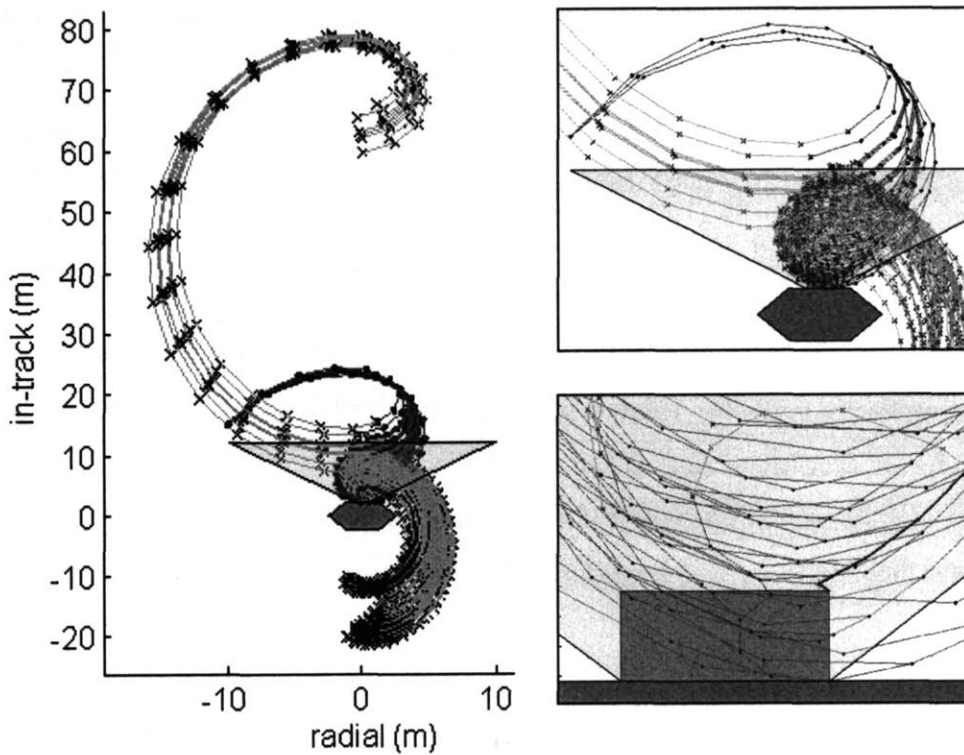


**Fig. 5-22:** Safe rendezvous trajectory with robustness to initial condition velocity uncertainty

sequence requires 2.1 mm/s. The cost of robustness in this case is less than 2% of the cost of the nominal safe trajectory without robustness. However, the problem is particularly sensitive to the amount of uncertainty present in the in-track velocity and can quickly become infeasible for larger uncertainties.

## 5.9 Summary

Safety in autonomous spacecraft rendezvous trajectory design allows abort with guaranteed collision avoidance for a class of anomalous system behaviors. This chapter introduced several online optimization formulations that guarantee passive and active safety and demonstrated in numerous simulations that the additional fuel costs are comparatively small, particularly relative to commonly considered suboptimal trajectories. Additional restrictions to guarantee failure trajectories that minimize drift

and guarantee long-horizon passive collision avoidance were shown to require fuel use on the same order of magnitude as optimized solutions that do not include safety guarantees. Approximate analytic methods for creating upper and lower bounds on the expected fuel use for several mission types yielded accurate estimates compared to optimized fuel costs. A convex formulation of the safety problem was introduced which uses approximately twice as much fuel, but more than 150 times less computation time than the nonconvex formulation. An active safety approach was developed and shown to be capable of achieving the same fuel costs as trajectories without safety while still guaranteeing collision-free escape trajectories for a large class of potential anomalies, including single thruster failures. The safety algorithms presented provide a fuel-efficient, computationally feasible framework for designing safe mode procedures for multi-spacecraft missions.



## Chapter 6

# Safe Docking Demonstrations on SPHERES

This section describes several safe autonomous rendezvous and docking experiments performed using the Synchronized Position Hold Engage and Reorient Experimental Satellites (SPHERES) hardware testbed aboard the International Space Station (ISS).

### 6.1 SPHERES Background

The SPHERES testbed (shown in Fig. 6-1) is presently in orbit aboard ISS. The SPHERES testbed is intended to facilitate the development and evaluation of control algorithms for spacecraft formation flying and autonomous rendezvous and docking. Three SPHERES satellites are onboard the ISS as of December, 2006. Each satellite has a mass of 4.2 kg and is capable of producing a 0.22 N thrust in any axial direction [78]. The SPHERES experiments flown on ISS are first tested on the SPHERES flat table testbed in the MIT SSL laboratory. The flat table testbed uses the same type of satellites that are aboard ISS, but mounted on air carriages so that the vehicles experiment double integrator dynamics in two dimensions. The mass of the combined satellite/air carriage system is 12.4 kg.

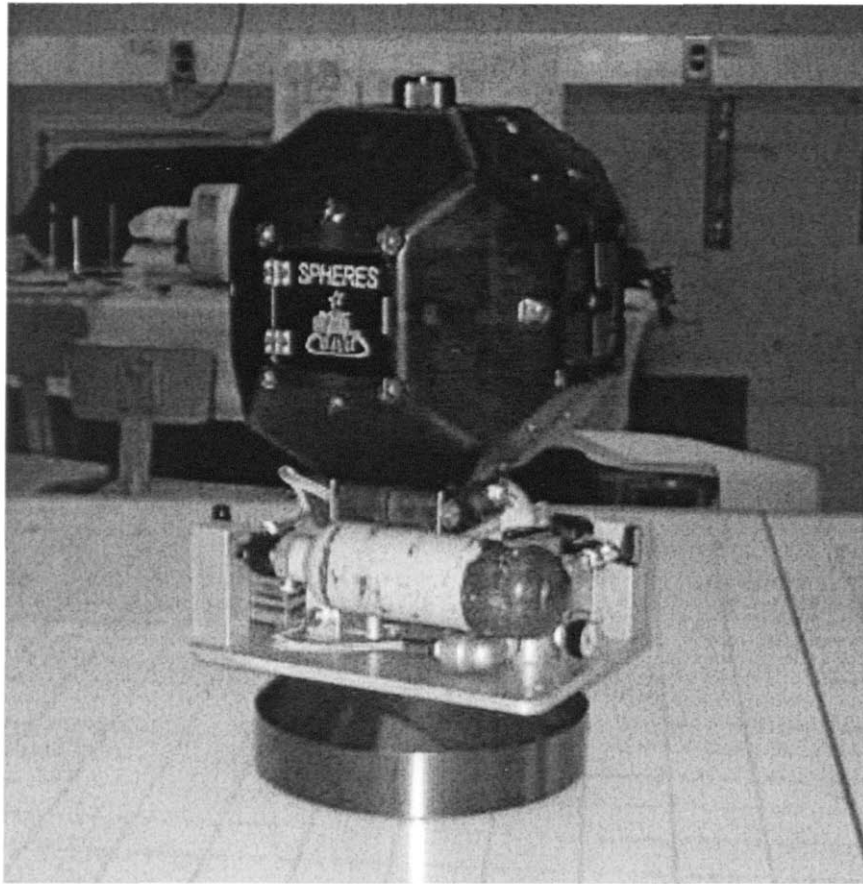


Fig. 6-1: SPHERES Microsatellite in air carriage on flat table testbed

## 6.2 Safe Autonomous Rendezvous and Docking on the SPHERES Testbed

The safe rendezvous and docking algorithms introduced in Chapter 5 were demonstrated on the SPHERES testbed onboard the ISS. The SPHERES microsatellites did not contain a linear programming solver at the time of the safe rendezvous and docking experiment, so instead of solving for an optimized rendezvous trajectory online, a trajectory was optimized offline and flown onboard the microsatellites as a series of waypoints. The waypoints were followed use the SPHERES PID-controller [78]. The waypoints were stored in an LVLH frame in which the target and chaser satellites both begin with a specified separation distance on the  $y$  axis and no offset from the  $x$  or  $z$  axes. During the experiment, the chaser satellite follows the waypoints in the

trajectory and the target satellite uses a station-keeping controller to stay stationary at the origin. Onboard ISS, the LVLH frame for the trajectory-following is oriented according to the following algorithm:

1. Chaser and target satellites point toward each other
2. Chaser adjusts the distance between itself and the target to the distance of the initial waypoint in the rendezvous trajectory.
3. LVLH frame is aligned to the chaser body-fixed frame

Following this frame orientation procedure allows the satellites to begin from most positions in the feasible operating areas for SPHERES on ISS. The initialization instructions for the astronauts specify that the target spacecraft should be placed near the center of the operating area for SPHERES and the chaser satellite should be placed nearby.

To design the safe rendezvous trajectory for use in the ISS experiment, the system dynamics used were double integrators, because the operating area inside the ISS is sufficiently small that the Earth gravity gradient effects are minimal. In the notation of Chapter 5, double integrator dynamics are [102]

$$A_k = A = \begin{bmatrix} I_3 & \Delta t I_3 \\ 0_3 & I_3 \end{bmatrix}, \quad B_k = B = \begin{bmatrix} \frac{(\Delta t)^2}{2} I_3 \\ \Delta t I_3 \end{bmatrix} \quad \forall k \quad (6.1)$$

Two experiment scenarios were prepared for testing on ISS: safe docking with a stationary target and safe docking with a rotating target. During the ISS test session, the astronaut conducting the SPHERES test only had time to conduct the stationary safe docking experiments. This chapter will present the scenario for rotating docking as well and describe an alternate test that was performed using the SPHERES flat-table testbed in the MIT Space Systems Laboratory (SSL). All optimized rendezvous trajectories presented in this chapter assume that the chaser satellite has a mass of 12.4 kg so that the resulting trajectory can be tested on the flat table testbed or on the ISS testbed. Because only the state waypoints in the trajectory are used

as inputs to the SPHERES flight software and not the optimized thrust input, the effect of the spacecraft mass parameter only serves to determine the effective control authority available at each step in the plan. Passive safety will be tested by randomly disabling the chaser satellite's thruster during one of the last 5 time steps and leaving the thrusters disabled for the remainder of the trajectory. If no collision occurs, then the actual trajectory that the satellite followed will have been passively safe.

The optimized safe rendezvous path for the stationary safe rendezvous experiment is shown in Figures 6-2 and 6-3. The chaser satellite begins with an 80 cm offset from the target. This distance was chosen to balance the preference for a large approach distance within the ISS SPHERES operating area against the danger of losing metrology near the edges of the working area. The optimized trajectory in this cases enforces safety for the last 5 steps of the trajectory. Because of the double integrator dynamics, the trajectory in the event of a failure continues to follow the path of the trajectory before the failure. This is particularly challenging for a safe rendezvous problem, because any direct approach to target spacecraft would collide in the event of a failure. The optimized safe trajectory approaches in such a way that it succeeds in passing through the docking region even in the event of a failure. Thus, one would expect failure, as well as nominal, trajectories to dock successfully.

Figures 6-4 and 6-5 show the optimized safe rendezvous path for docking with a rotating target. The initial state of the chaser spacecraft is half distance from the target as in the stationary case, because the chaser will need space to travel in a line-of-sight cone that rotates with the target. The target rotates at 0.039 rad/s, which was chosen to allow the experiment to complete in under two minutes (the maximum designated duration). The dynamics of docking with a rotating spacecraft force the velocity vector of the chaser satellite to change direction constantly. As a result of this, the problem of guaranteeing safety is significantly less constrained for the rotating case, allowing the last 20 steps (40 s) of the 40 step trajectory to be guaranteed safe. For failures earlier in the guaranteed-safe region of the trajectory, the expected abort trajectory would drift away from the target. A failure occurring in the last step of the rendezvous trajectory would result in a passive rendezvous.

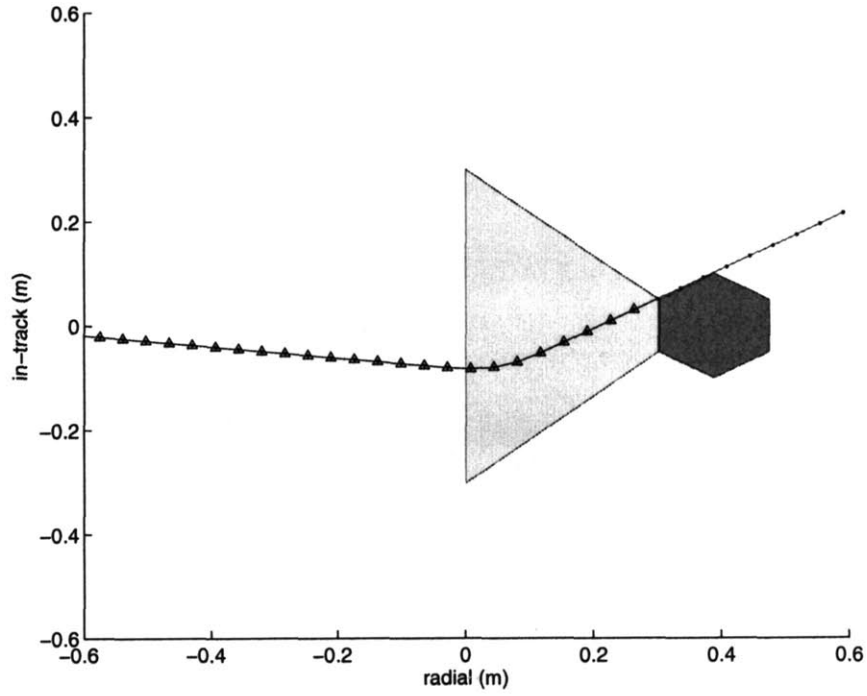


**Fig. 6-2:** Planned safe trajectory for stationary rendezvous:  $x$ - $y$  view. Note that trajectory  $z$  offset is zero at all times

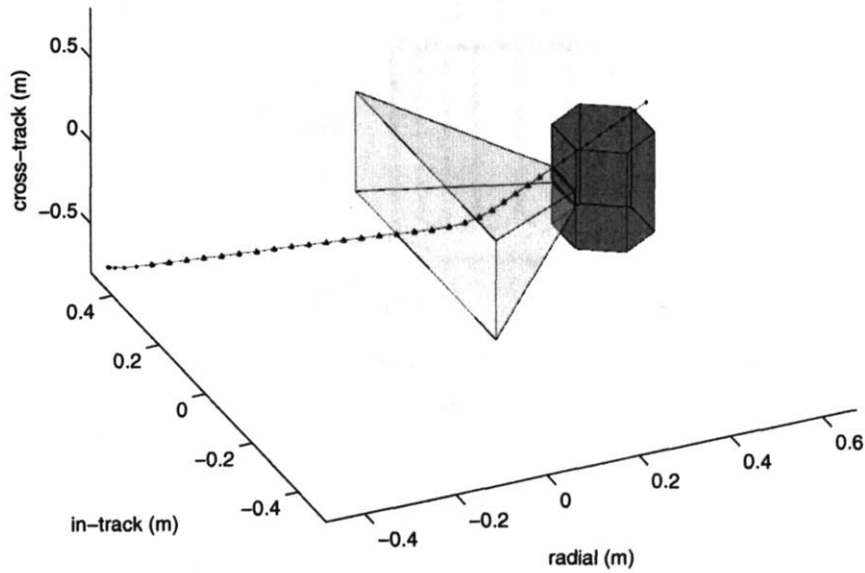


**Fig. 6-3:** SPHERES Microsatellite in air carriage on flat table testbed: Perspective view

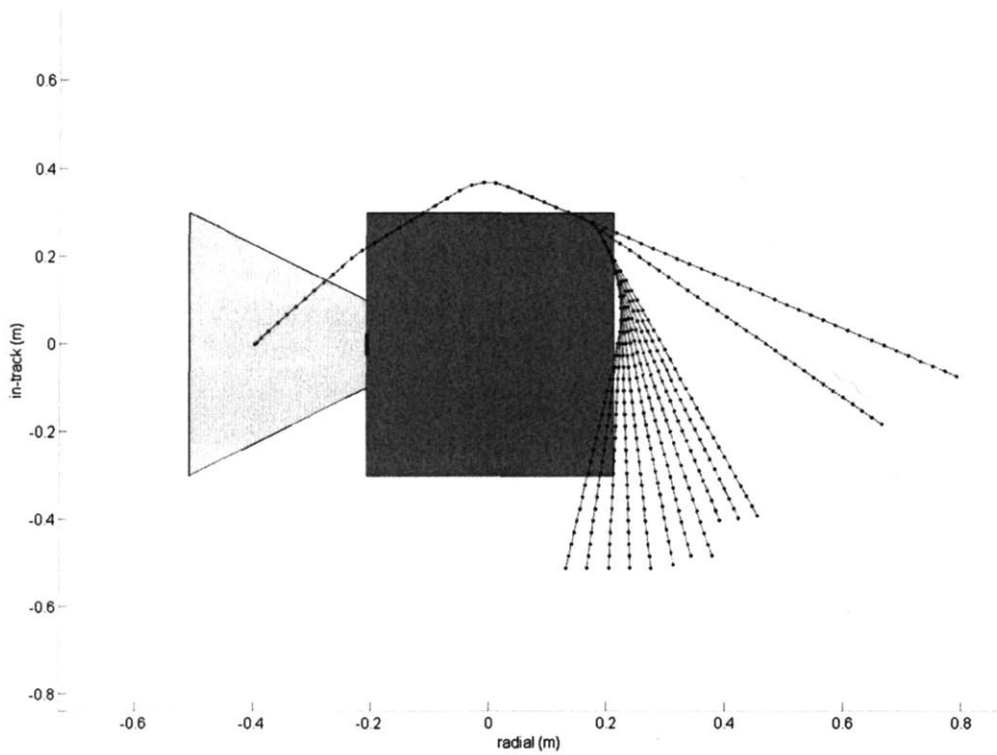


**Fig. 6-4:** Planned safe trajectory for rotating rendezvous:  $x$ - $y$  view. Note that trajectory  $z$  offset is zero at all times

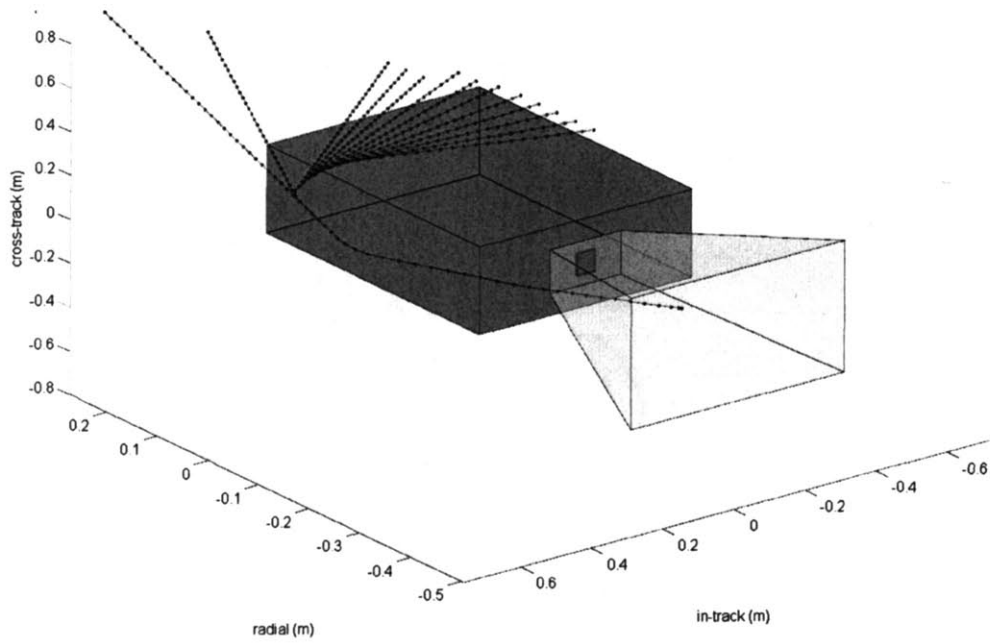


**Fig. 6-5:** Planned safe trajectory for rotating rendezvous: testbed: Perspective view

## 6.3 Flight Experiment Results

The results of the ISS experiment to demonstrate nominal safe docking are shown in Figures 6-7, 6-8, 6-9, and 6-10. The experiment begins with the target and chaser satellites deployed near the center of the ISS SPHERES feasible operating space. After waiting for the satellites' estimators to converge, the vehicles adjust their attitudes to point at one another. Then, the chaser satellite adjusts its distance along the pointing vector between the two spacecraft until it achieves the initial separation specified in the pre-optimized rendezvous trajectory. In the figures below, the line corresponding to "Sat1" refers to the chaser and the line corresponding to "Sat2" refers to the target. Compared to previous test sessions, the trajectory following error was significantly reduced, with a maximum of less than 5 cm of error. The reasons for this were likely twofold: in this test session, the 5 beacon estimator was used, greatly improving the accuracy of the estimates; and the trajectory following in this test session was accomplished using a PID controller instead of a PD controller. However, it should be noted that the greatest trajectory error occurred when the desired trajectory experienced its highest rate of change, indicating that the bandwidth of the desired trajectory should be reduced for future experiments using the same tracking controller. The goal of this experiment was for the chaser satellite to dock with the target satellite and the data indicates that this goal was achieved successfully 6-6.

The results for the demonstration of a stochastic failure in the safe trajectory are shown in Figs. 6-11, 6-12, 6-13, and 6-14. The goal of this test was to follow a trajectory demonstrating safe rendezvous with a simulated failure toward the end of the trajectory. The time of the failure is decided online in the SPHERES flight software at the time the test begins. The only restriction on the failure time is that it occur during a window in which the optimized trajectory has been guaranteed to be safe in presence of failures. Since the optimized trajectory is chosen prior to the failure time, this test is a demonstration of the safety algorithm to handle arbitrary failures that occur during the time. Ideally, a test such as this one would be run many times as a stochastic demonstration of the safety properties of the safe rendezvous

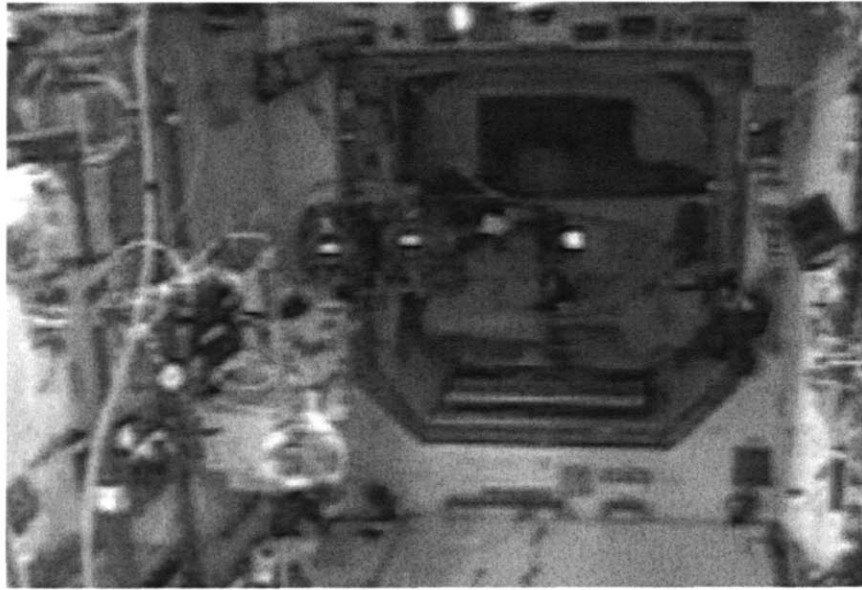


**Fig. 6-6:** SPHERES satellites docked together aboard the International Space Station using a safe optimized rendezvous trajectory.

and docking trajectory optimization algorithm.

The results in Figs. 6-11, 6-12, 6-13, and 6-14 indicate that the stochastic failure experiment proceeded nearly identically to nominal experiment until the end of the trajectory when the simulated failure occurred. At that point, as anticipated, the spacecraft disabled its thrusters and entered a drift mode. As in the nominal experiment, the target held its position with very little state error and the chaser spacecraft followed its trajectory very accurately. Also, as in the previous case, the maximum trajectory-following error occurred at the “knee” in the desired trajectory where the rate of change reached its maximum. The trajectory followed after the thruster failure occurred was very close to the expected trajectory in the event of a failure. According to the telemetry gathered in flight (truth data from video footage is not yet available) failure trajectory entered the predefined terminal docking box and successfully docked even for the failure case. Although a safe trajectory is defined specifically in terms of collision avoidance, the terminal docking box was not inside failure avoidance region and so the resulting rendezvous is not inconsistent with a safe maneuver.



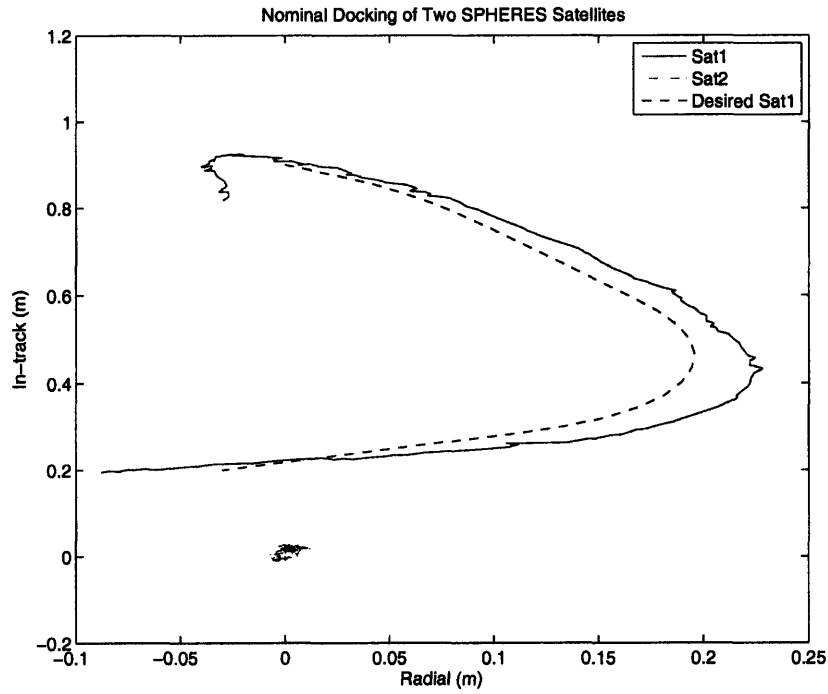


**Fig. 6-7:** Position trajectory followed during nominal docking ISS experiment:  $x$ - $y$  view

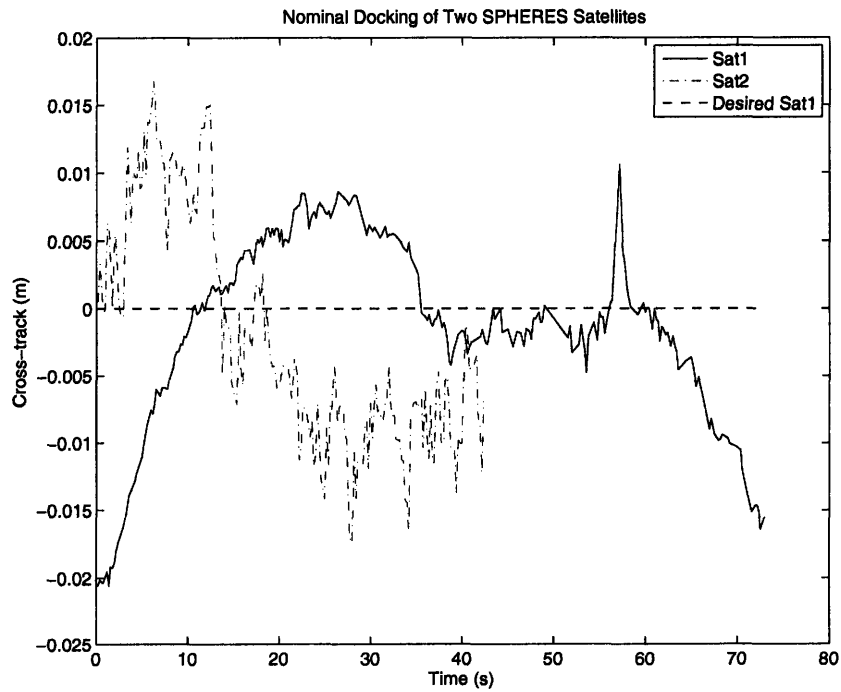


**Fig. 6-8:** Position time-series for  $z$  axis during nominal docking ISS experiment

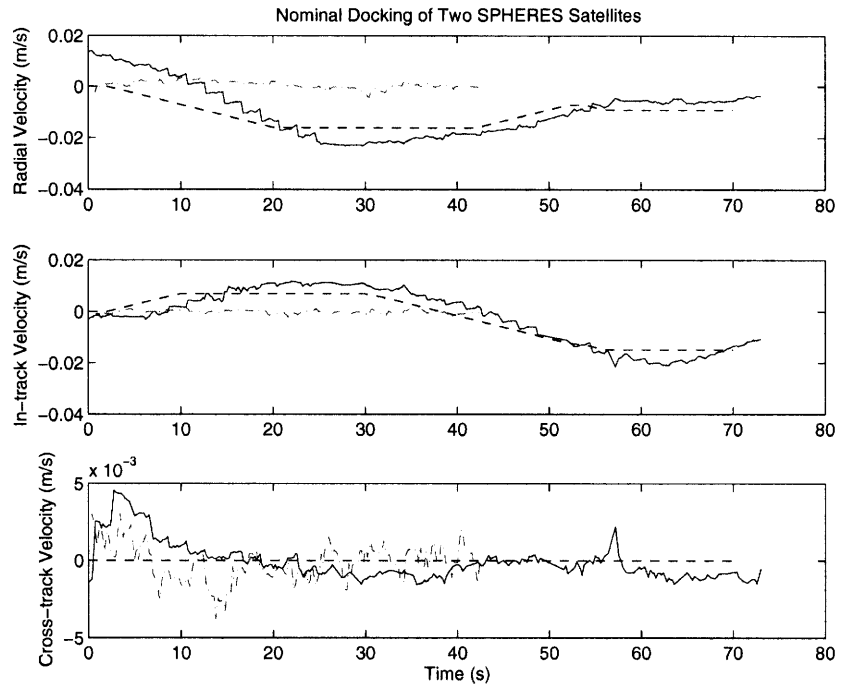


**Fig. 6-9:** Velocity time-series view during nominal docking ISS experiment

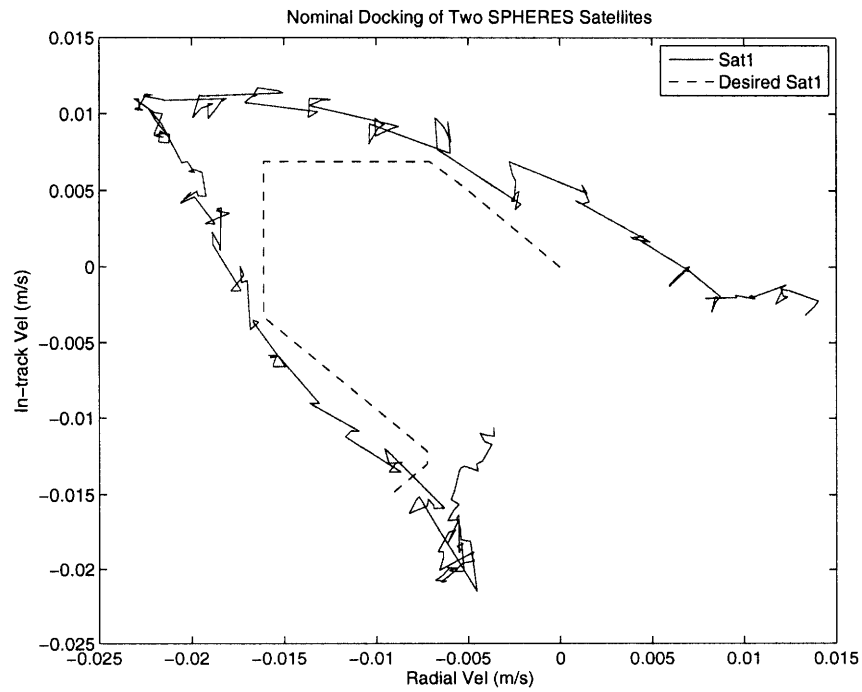


**Fig. 6-10:** Velocity trajectory followed during nominal docking ISS experiment:  $x$ - $y$  view

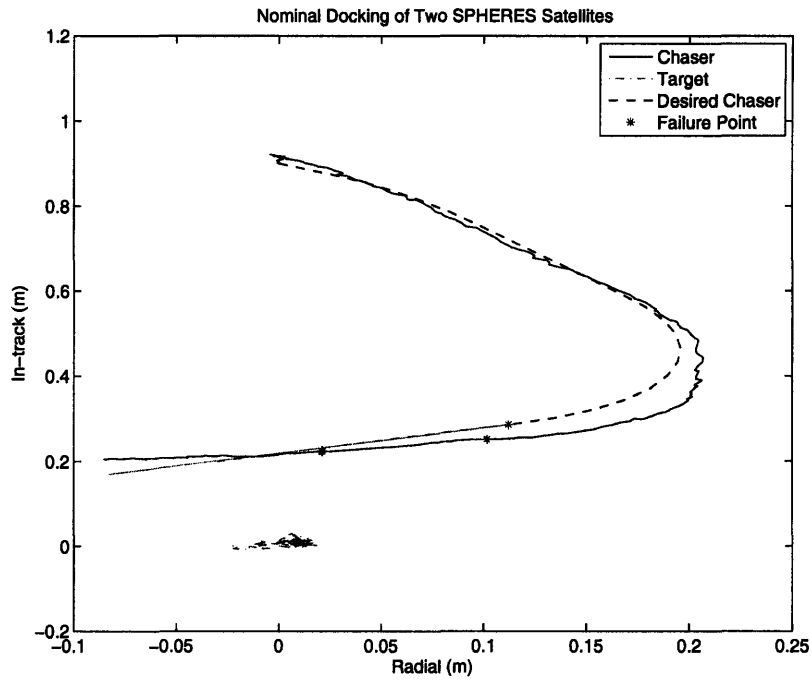


**Fig. 6-11:** Position trajectory followed during failed docking ISS experiment:  $x$ - $y$  view

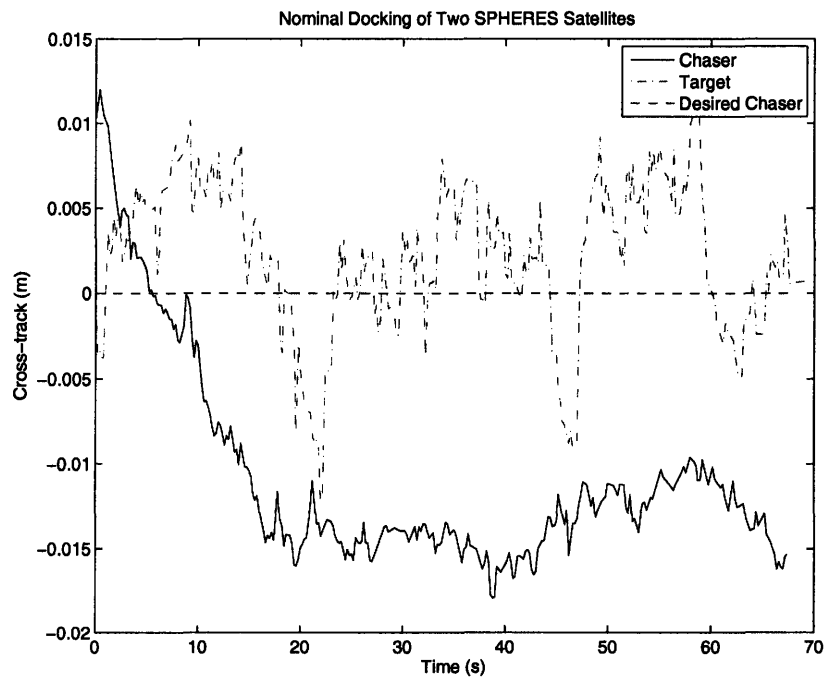


**Fig. 6-12:** Position time-series for  $z$  axis during failed docking ISS experiment

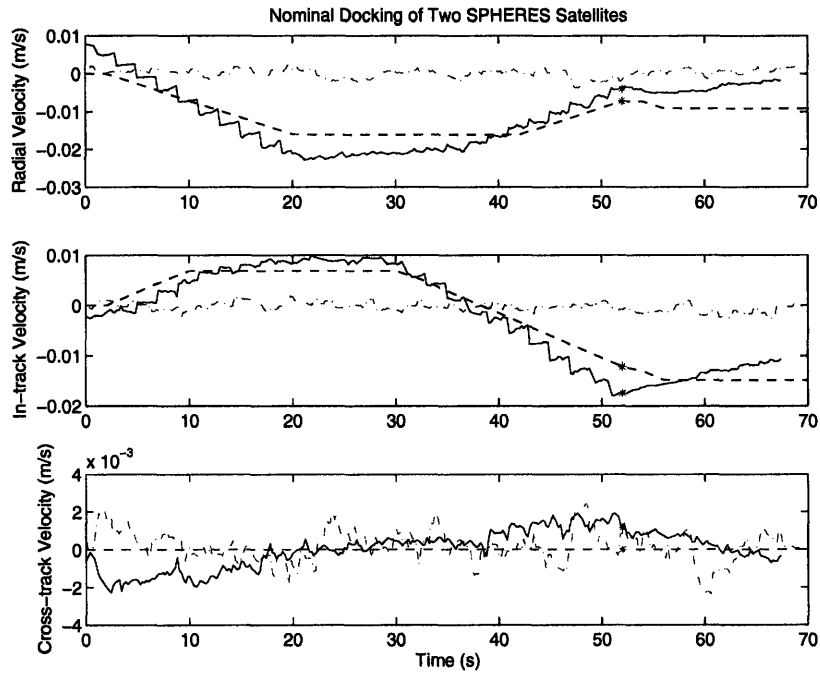


Fig. 6-13: Velocity time-series view during failed docking ISS experiment

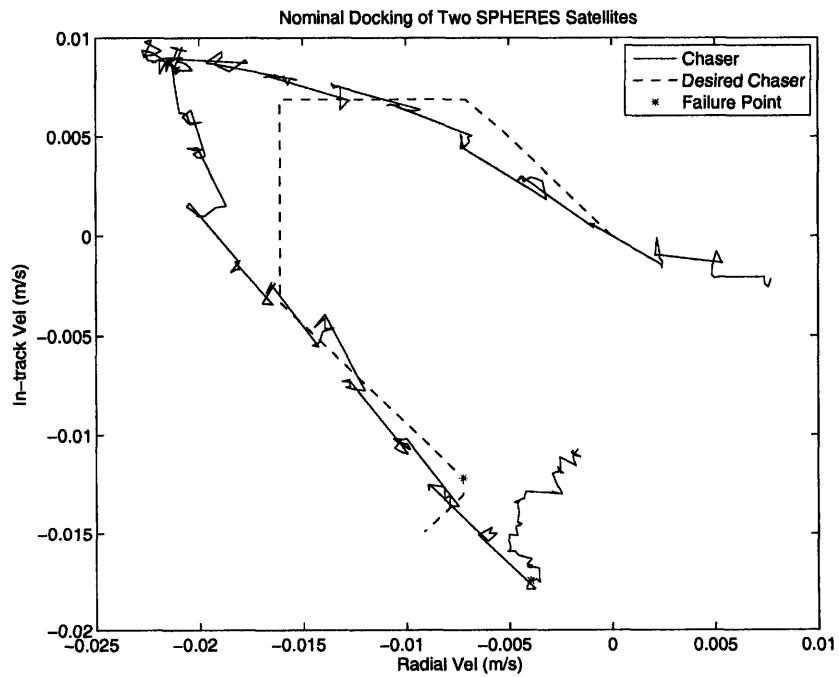


Fig. 6-14: Velocity trajectory followed during failed docking ISS experiment:  $x$ - $y$  view

## 6.4 Flat Table Experiment Results

The results in Figs. 6-15, 6-16, 6-17, 6-18 show a rotating target rendezvous experiment with a stochastic thruster failure inserted. The failure occurred at the 38th step in the 40 step rendezvous trajectory. Fig. 6-15 shows that the target spacecraft performed its station-keeping task to within centimeters of the origin. Likewise, the chaser spacecraft also tracked its desired safe rendezvous trajectory well. After the simulated failure occurred, the chaser spacecraft drifted away from the chaser along an unforced trajectory. Video of the experiment indicates that the chaser vehicle did not make contact with the target. The velocity tracking data in Figs. 6-17 and 6-18 is considerably more error prone than that of the velocity tracking for the ISS experiment. This is likely the product of additional disturbances entering the flat table environment from the air carriage system and imperfections in the degree to which the table was perfectly level and flat. Future experiments should consider incorporating additional uncertainty robustness into the trajectory design.

## 6.5 Summary

The safe autonomous rendezvous and docking tests performed aboard the International Space Station using the SPHERES testbed successfully demonstrated a safe rendezvous with a stationary target and a successful rendezvous after a stochastic thruster failure. A similar experiment for a rotating rendezvous trajectory demonstrated collision avoidance on the flat table testbed.

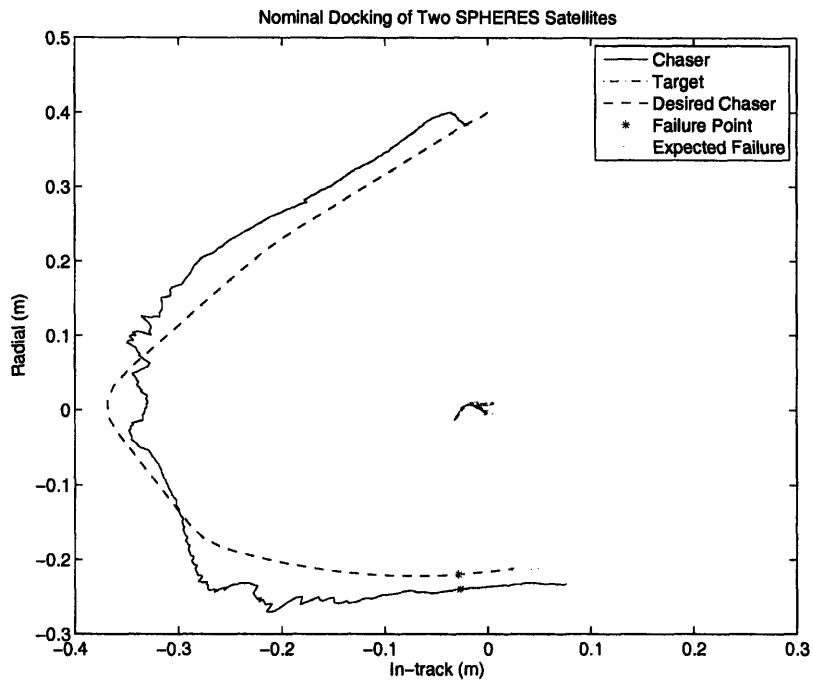


**Fig. 6-15:** Position trajectory followed during failed docking flat table experiment: *x-y* view

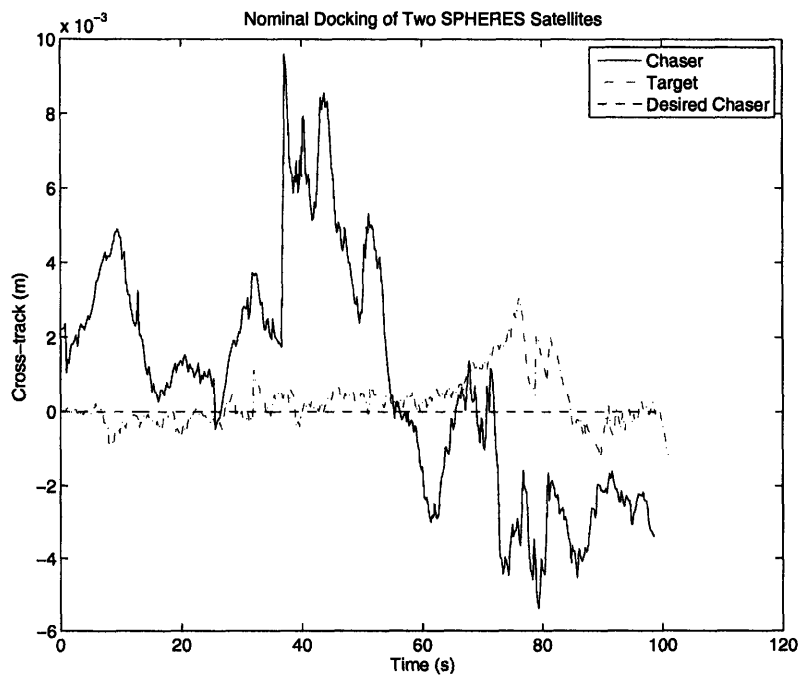


**Fig. 6-16:** Position time-series for *z* axis during failed docking flat table experiment

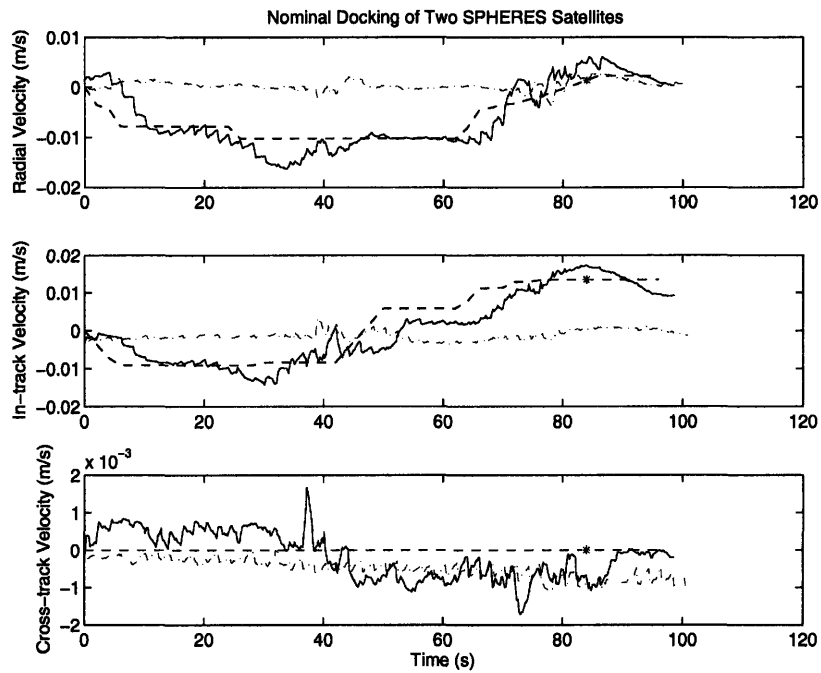


**Fig. 6-17:** Velocity time-series view during failed docking flat table experiment

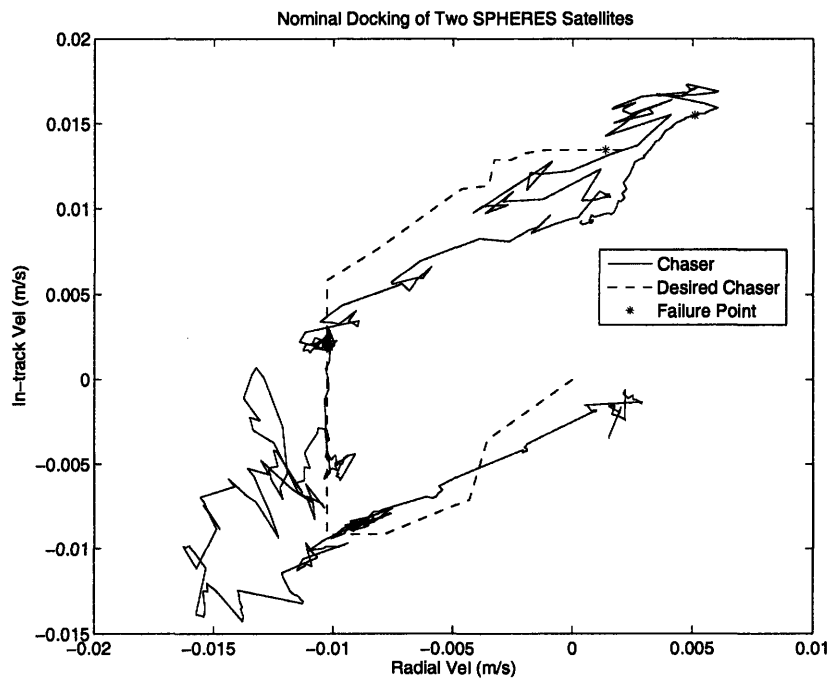


**Fig. 6-18:** Velocity trajectory followed during failed docking flat table experiment: *x-y* view





# Chapter 7

## Conclusions and Future Work

### 7.1 Conclusions

This thesis has presented, analyzed, and applied several new technologies related to autonomous control of spacecraft in proximity operations. Future missions falling into that broad category include formations of spacecraft cooperating to achieve common goals and autonomous rendezvous of spacecraft. The ideas explored in this thesis focus on commonalities between these mission types: an emphasis on relative dynamics, adherence to inter-vehicle performance constraints, and preventing relative drift. The following subsections summarize the contributions of this work.

#### 7.1.1 Linearized Relative Dynamics

Chapter 2 derived and validated linearized relative spacecraft dynamics that incorporate the effects of Earth oblateness and are valid for widely separated, eccentric orbits. Linearization and discretization assumptions were examined and shown to be valid for modeling the relative trajectories within expected error box sizes for several planned missions (including MMS). The new dynamics extend the range of missions in which linear controllers and linear optimization-based model predictive controllers can be used. The enhanced capabilities were demonstrated by embedding the dynamics in a model predictive controller to control a high fidelity multi-week simulation of

a four spacecraft MMS-like mission. The results showed that the controller is reliable and that formation flying using MPC with  $J_2$ -modified GVEs requires fuel use that is comparable to using unmodified GVEs in simulations that do not include the  $J_2$  effects.

### 7.1.2 Optimized Initialization of Semi-Invariant Orbits

Chapter 3 introduced an approach for optimizing  $J_2$  invariance between spacecraft that explicitly minimized the fuel use required to achieve the invariant states. This approach also allowed weights to be assigned to the relative emphasis on invariance, minimizing fuel use, and maintaining a desired fleet relative configuration. The algorithm extends previous approaches to  $J_2$  invariance by explicitly considering arbitrary time frames, as opposed to the infinite horizon, and by allowing the osculating Cartesian drift to be penalized, as opposed to the secular mean drift. Furthermore, the approach can be formulated to use a linear optimization, enabling a fast online implementation, whereas previous methods for optimizing multi-objective formation initial conditions relied on highly nonlinear optimization techniques. The range of possible optimized conditions were examined for example orbits in LEO and HEO. The optimized conditions were compared to analytic solutions and found to provide similar levels of drift at lower maneuver cost and more closely matching desired geometric configurations. In a formation where the principal control objective is to “not drift,” the proposed approach can be used for fuel-optimized online initialization of a formation flying mission.

### 7.1.3 Control of Spacecraft Formations Using MPC

Chapter 4 demonstrated the use of the trajectory dynamics and optimization formulation developed in Chapter 2 in a closed-loop model predictive controller. This controller was applied to a proposed formation flying mission and demonstrated in a series of high fidelity multi-week simulations, which modeled all realistic orbital disturbances and navigation uncertainty. The simulations are the first instance in the

literature of formation flying spacecraft using variable thrusting constraints to enforce passive observation periods with error box constraint satisfaction. The effects of the passive observation constraints on fuel-use and feasibility are examined, as are the effects of imposing passive invariance as a control constraint and several types of error box relaxation. These simulations demonstrated that model predictive control using the new linearized dynamics can be used to control an actual mission with realistic control requirements.

#### **7.1.4 Safety in Autonomous Rendezvous and Docking**

Chapter 5 introduced a new approach for generating rendezvous trajectories that are safe in the presence a large class of system failures. This approach is flexible (*i.e.*, same problem formulation captures many rendezvous situations including tumbling targets), fuel-optimized, and computationally feasible. Previous rendezvous approaches in the literature which provide guaranteed safety do not minimize fuel use or are not computationally feasible for online implementation. The new safe formulation was evaluated using a stochastic analysis and determined to improve safety (*i.e.*, reducing the likelihood of a failure resulting in a collision) with minimal additional fuel costs over fuel-optimal trajectories. Approximate, but verifiable, analytic bounds were found for the maximum and minimum fuel that a safe trajectory would require. Additional restrictions to guarantee failure trajectories that minimize drift and guarantee long-horizon passive collision avoidance were shown to require fuel use on the same order of magnitude as optimized solutions that do not include safety guarantees. A convex formulation of the safety problem was introduced which uses approximately twice as much fuel, but more than 150 times less computation time than the nonconvex formulation. An active safety approach was developed and shown to be capable of achieving the same fuel costs as trajectories without safety. The active approach still guarantees collision-free escape trajectories for a large class of potential anomalies, including single thruster failures. Previous approaches to planning active abort strategies were planned offline or did not use fuel minimization. The safe trajectory generation algorithm is the first computationally feasible, fuel-optimized

approach for guaranteeing passive and/or active safety for rendezvous with stationary and tumbling targets.

### **7.1.5 Safe Autonomous Rendezvous Demonstration on Orbit**

Chapter 6 used the safe trajectory generation algorithm from Chapter 5 to generate safe rendezvous trajectories for the SPHERES hardware testbeds. Safe trajectories were demonstrated onboard the International Space Station and on a flat table. Trajectories were followed in both nominal and simulated-failure configurations, demonstrating the feasibility of following automatically-generated fuel-minimizing safe trajectories in space. The on-orbit demonstration is the first known instance of a spacecraft rendezvous following a fuel-minimized trajectory guaranteed to be safe up to the moment of docking.

## **7.2 Future Extensions**

The work presented in this thesis addresses several areas where spacecraft formation flying and spacecraft rendezvous and docking technologies overlap. Optimizations using relative dynamics and exploiting the concept of passive relative invariance are used to reliably plan fuel-efficient trajectories in both mission types. Imposing safety as a constraint on rendezvous and docking trajectories was examined from the unique perspective of constraining the paths followed by a spacecraft in the event of a failure. This approach has the immediate benefit of collapsing an enormous space of possible multi-vehicle safe mode responses into a simple, guaranteed-safe plan for one spacecraft and continued nominal operation for the other. This same approach could be applied to formation flying spacecraft as well, potentially greatly decreasing the complication of considering the space of potential off-nominal interactions between arbitrary numbers of vehicles in close proximity. Adding convex safety constraints to formation flying trajectories generated using the MPC formulation in Chapter 2 may prove to be a simple, computationally inexpensive way to guarantee that a glitch in one spacecraft in a formation does not result in the catastrophic failure of two or

more spacecraft.

The formation initialization algorithm presented in Chapter 3 is presented in the form of a multi-objective optimization. However, the optimization provides no guarantee that a resulting trajectory will achieve certain minimal goals in its objectives, should those goals be critical mission objectives. A modified form of the initialization algorithm could be created that would provide constraint-based minimum guarantees for the optimized objectives. Also, the initialization algorithm as presented represents the beginnings of a hybrid between initial conditions and maneuver planning, two aspects of formation flying that are usually treated separately. Expanding on this idea to incorporate robustness or sensitivity to expected process and sensor noise would improve the approach. Further improvements might make maneuver-optimized initialization a viable option for closed-loop feedback control, in which each new trajectory optimization would simultaneously allow alterations of the formation configuration.

The safe rendezvous technique could be made safer through the addition of more uncertainty robustness. In particular, types of uncertainty not considered in the current formulation include: process noise (*e.g.*, attitude errors and thruster magnitude errors) and uncertainty in the future trajectory of the target spacecraft. Adding guarantees for constraint satisfaction in the presence of these sources of error is a difficult proposition, because additional robustness will likely lead to less feasibility. The current navigation error robustness approach is computationally simple, but known to be overly conservative in a system using feedback optimization. Enhancing the current safe trajectory generation approach to have safety guarantees in the presence of and explicitly account for feedback are critical next steps.



# Appendix A: Station-keeping Costs and Maneuver Costs for MELCO Formation Flying Mission

This appendix examines several LP-designed maneuvers as planned trajectories in an LVLH frame, a differential orbital element frame, and as thruster inputs. These trajectories were generated using the  $J_2$ -modified GVE-based planner described in Chapter 2. Each maneuver is planned to occur over the course of two orbits using a 10.8 second time step, with inputs allowed at all times. The large size of the formations examined in this section necessitated an additional step in formation design: after creating the desired LVLH states using the procedures in Ref. [109], the desired states were converted to relative orbital elements, where any desired differential semimajor axis was eliminated. This approach ensures that formations are based on passive-apertures, but still have the same period (*i.e.*, the satellites do not drift with respect to each other over time).

The MELCO formation flying mission consists of two different formation types: 1) in-track separation formations and 2) in-track/cross-track passive aperture formations (triangular). Figures 7-1 and 7-2 show the average amount of fuel required to maintain various sizes of in-track formations and passive aperture formations, respectively. For each type of formation at each baseline, one or more four day simulations were conducted to determine the average fuel usage. Each formation size uses an error box that is 10% of the baseline, except the 50 meter passive aperture. In that case, the error box is sufficiently small that the navigation errors [73] strongly influence the

closed-loop behavior, so a  $5 \times 10 \times 5$  meter (radial/in-track/cross-track) error box is used instead. This change allows a slightly more natural relative elliptical motion in the radial/cross-track plane (typically a  $1 \times 2$  ellipse).

Maneuver trajectories generated in this section cover a wide range of different maneuver types and are summarized in Table 7.1. Fuel use for each maneuver type is summarized in Figures 7-3-7-6. Maneuvers from an in-track formation configuration to a passive aperture examine two different types of passive apertures: projected in-plane and projected out-of-plane. For each passive aperture radius, the in-plane formations require significantly less fuel to create than the out-of-plane formations. Also, note that generally it requires less fuel to create an in-track formation than a passive aperture. The costs of the maneuver types in Table 7.1 are characterized by the cost coefficient  $\alpha$ , the approximate fuel cost of each maneuver,  $\Delta V$  in m/s is given by

$$\Delta V = \alpha \times r \quad (7.1)$$

where  $r$  (in meters) is the baseline of a passive aperture or the separation between satellites for an in-track formation. The table shows how the expected maneuver costs change as additional orbit disturbances are modeled in the planner. To compute the cost maneuvers with no eccentricity modeled, the eccentricity of the reference orbit was set to zero and, similarly, cost computations with no  $J_2$  effect used the dynamics matrices from Chapter 2 computed with the  $J_2$  constant set to zero. Interestingly, in several cases, maneuvers required slightly less fuel when the effects of  $J_2$  were modeled, indicating that the trajectory optimizer was able to use the additional natural dynamics complexity in lieu of some thrusting. This phenomenon also appears when comparing the column of no disturbances with the column where only eccentricity is modeled. However, in all cases with both eccentricity and  $J_2$  effects, the costs are expected to be higher than the cases in which disturbances are only partially modeled. Note that one should not conclude that it is possible to use less complicated dynamics models to achieve fuel savings. It is still desirable to use the higher-fidelity models in the control formulation, because although they may initially produce more



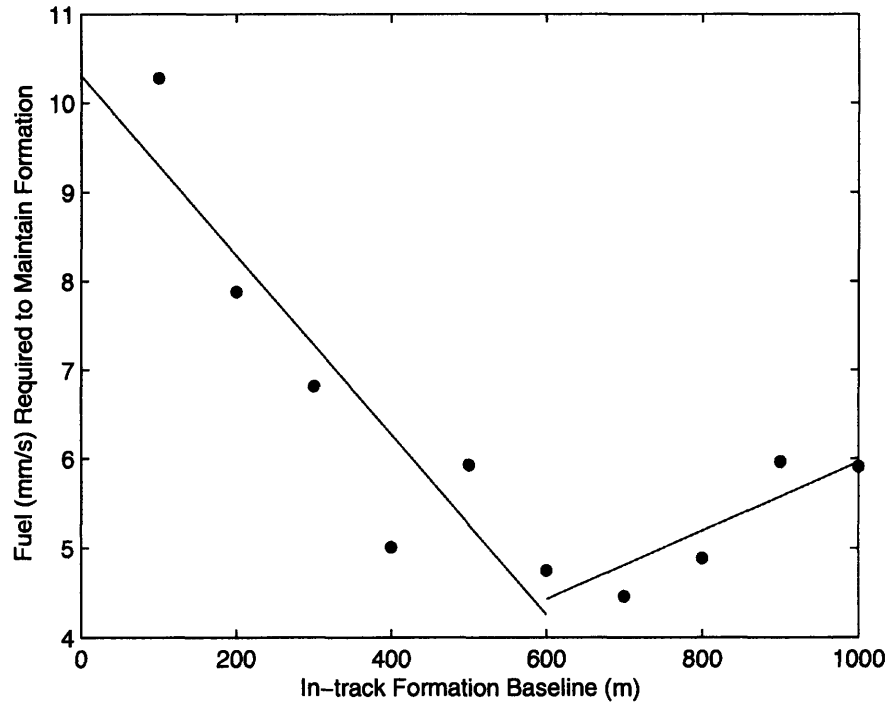


Fig. 7-1: Fuel Required to Maintain an In-track Formation

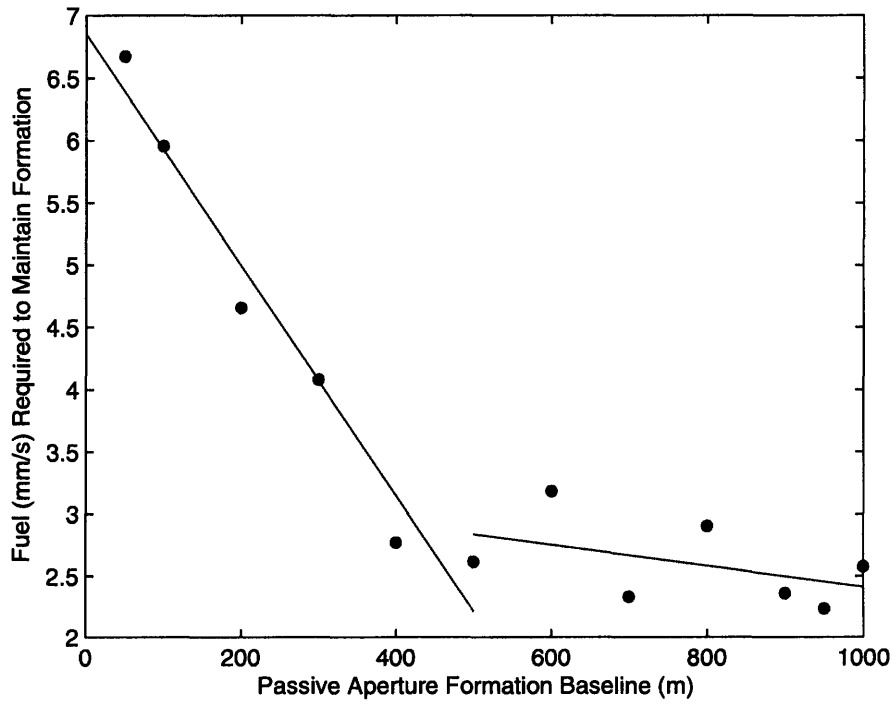
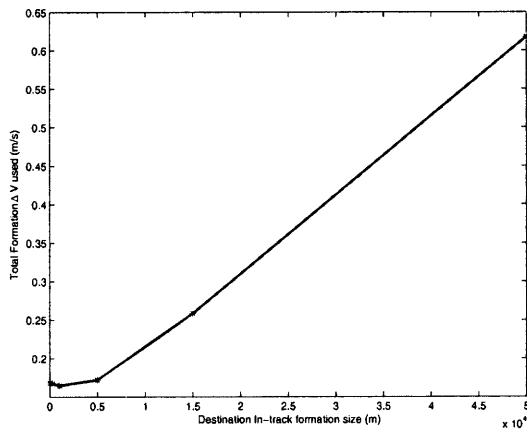


Fig. 7-2: Fuel Required to Maintain a Passive Aperture Formation

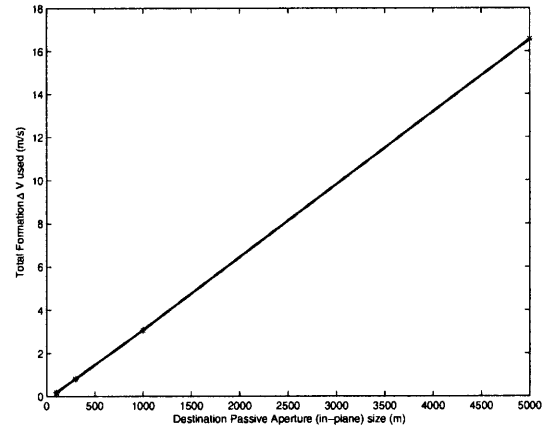
**Table 7.1:** Table of maneuvers planned using combinations of  $J_2$  and eccentricity. In the table, PA $\equiv$ passive aperture, IT $\equiv$ in-track formation, IP $\equiv$ in-plane passive aperture, and OP $\equiv$ out-of-plane passive aperture. The scalar  $\alpha$  is the fuel use coefficient, where the approximate fuel use in m/s is  $\alpha$  multiplied by the aperture size in meters.

Type	From	To	$J_2$ , Ecc $\alpha$	No $J_2$ , Ecc $\alpha$	$J_2$ , No Ecc $\alpha$	No $J_2$ , No Ecc $\alpha$
1	PA (50m)	IT (50m-50km)	0.0001693	0.0001206	0.0001170	0.0001214
2	PA (50m)	PA (50m-5km)	0.005030	0.004935	0.004941	0.004941
3	IT (1km)	IT (50m-50km)	0.0001656	0.0001142	0.0001135	0.0001158
4	IT (1km)	PA (IP) (50m-5km)	0.005055	0.004959	0.004967	0.004967
		PA (OP) (50m-5km)	0.01052	0.008272	0.008281	0.008281

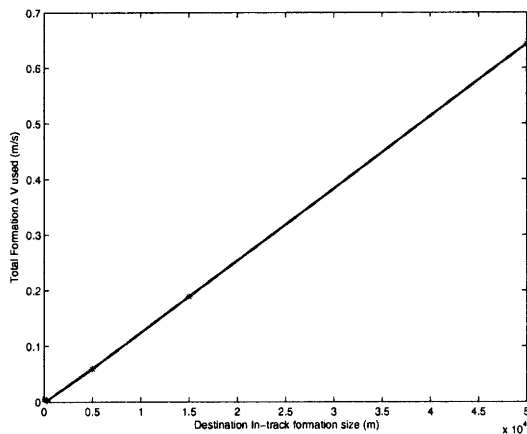
costly trajectories, fewer future corrective actions should be required at the end of those trajectories.



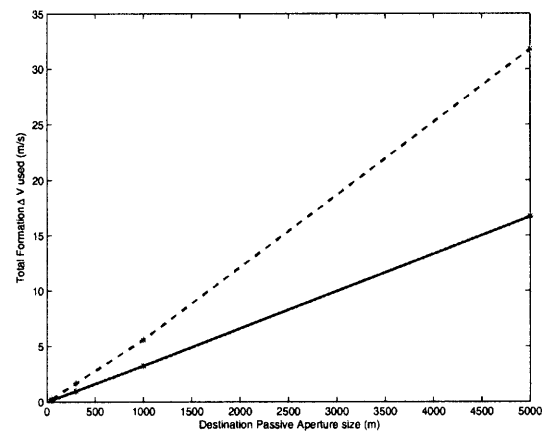
(a) Cost of maneuvering from a 50m Passive Aperture (in-plane) to an In-track Formation.



(b) Cost of maneuvering from a 50m Passive Aperture (in-plane) to a Passive Aperture (in-plane).

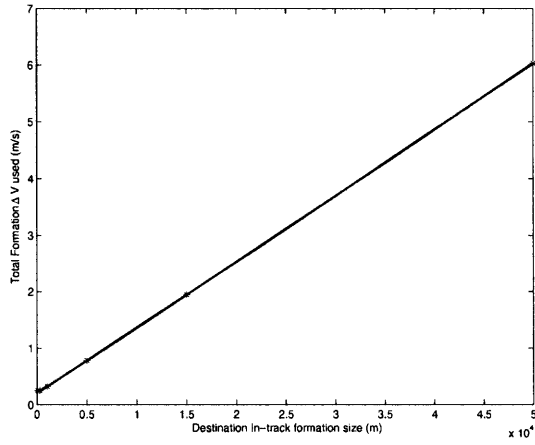


(c) Cost of maneuvering from a 1km In-track Formation to an In-track Formation.

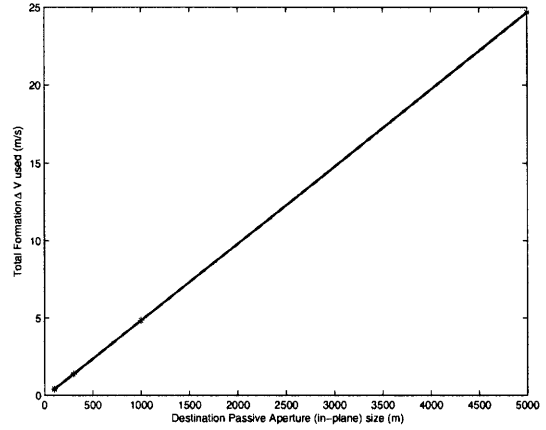


(d) Cost of maneuvering from a 1km In-track Formation to a Passive Aperture (in-plane=blue, solid; out-of-plane =red,dashed).

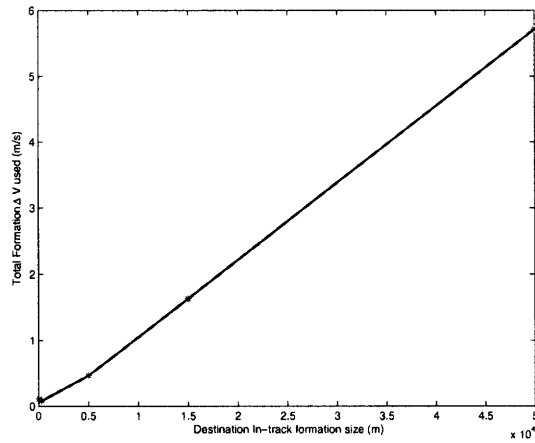
**Fig. 7-3:** Maneuver costs: plans created accounting for eccentricity and  $J_2$  effects



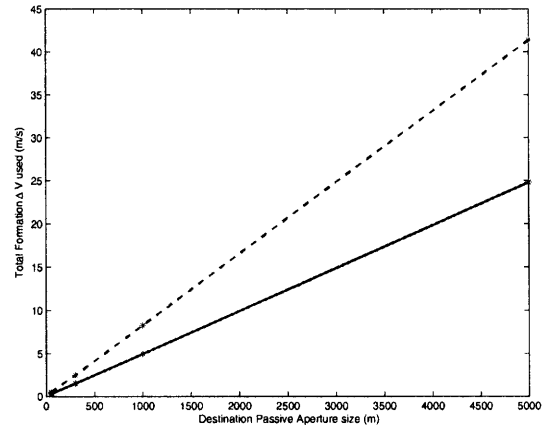
(a) Cost of maneuvering from a 50m Passive Aperture (in-plane) to an In-track Formation.



(b) Cost of maneuvering from a 50m Passive Aperture (in-plane) to a Passive Aperture (in-plane).

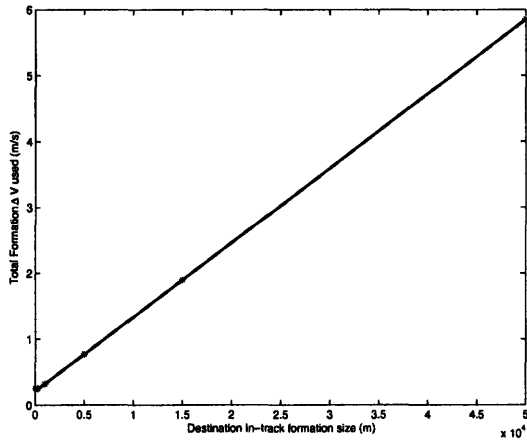


(c) Cost of maneuvering from a 1km In-track Formation to an In-track Formation.

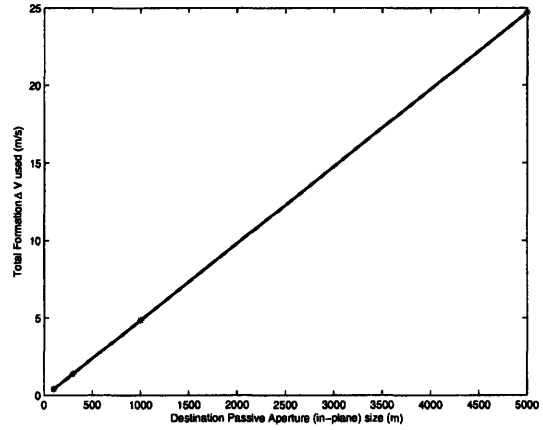


(d) Cost of maneuvering from a 1km In-track Formation to a Passive Aperture (in-plane=blue, solid; out-of-plane =red,dashed).

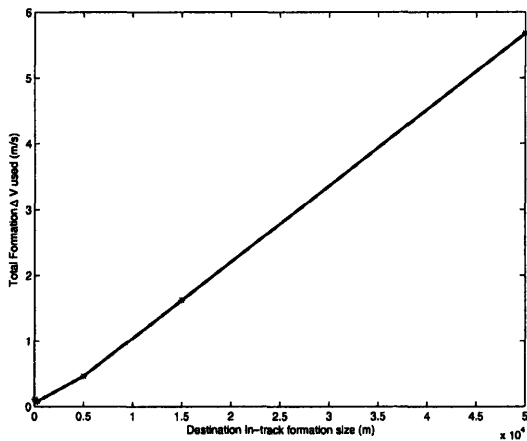
**Fig. 7-4:** Maneuver costs: plans created accounting for eccentricity with no  $J_2$  effects modeled



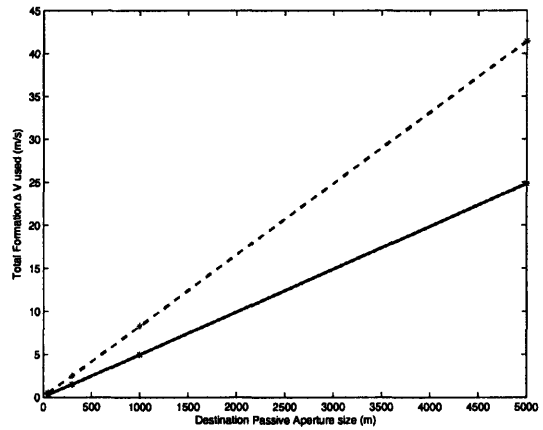
(a) Cost of maneuvering from a 50m Passive Aperture (in-plane) to an In-track Formation.



(b) Cost of maneuvering from a 50m Passive Aperture (in-plane) to a Passive Aperture (in-plane).

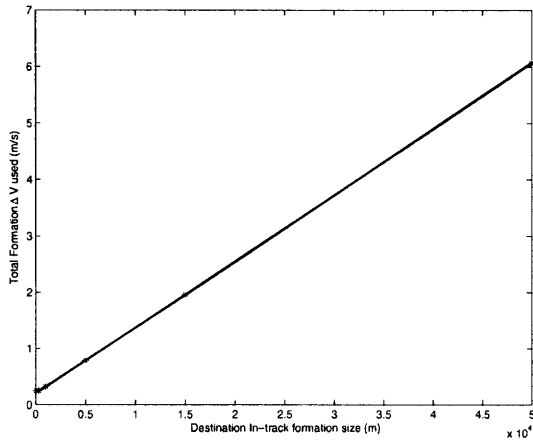


(c) Cost of maneuvering from a 1km In-track Formation to an In-track Formation.

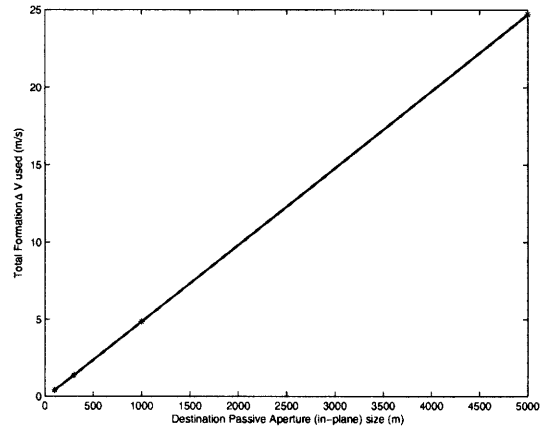


(d) Cost of maneuvering from a 1km In-track Formation to a Passive Aperture (in-plane=blue, solid; out-of-plane =red,dashed).

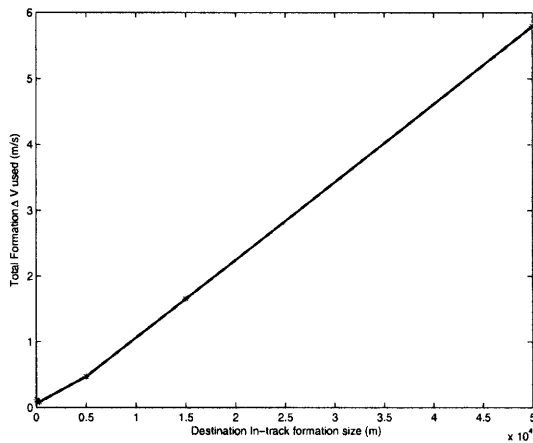
**Fig. 7-5:** Maneuver costs: plans created accounting for eccentricity with no  $J_2$  effects modeled



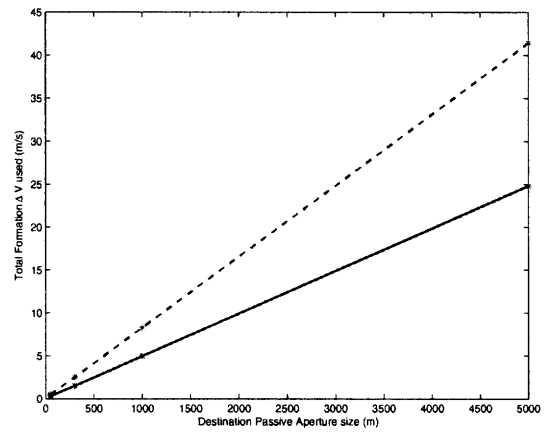
(a) Cost of maneuvering from a 50m Passive Aperture (in-plane) to an In-track Formation.



(b) Cost of maneuvering from a 50m Passive Aperture (in-plane) to a Passive Aperture (in-plane).



(c) Cost of maneuvering from a 1km In-track Formation to an In-track Formation.



(d) Cost of maneuvering from a 1km In-track Formation to a Passive Aperture (in-plane=blue, solid; out-of-plane =red,dashed).

**Fig. 7-6:** Maneuver costs: plans created not accounting for eccentricity with no  $J_2$  effects modeled

# Bibliography

- [1] J. Leitner, F. Bauer, D. Folta, M. Moreau, R. Carpenter, and J. P. How, "Distributed Spacecraft Systems Develop New GPS Capabilities," in *GPS World: Formation Flight in Space* Feb. 2002.
- [2] F. Bauer, K. Hartman, J. Bristow, D. Weidow, J. P. How, F. Busse, "Enabling Spacecraft Formation Flying Through Spaceborne GPS and Enhanced Autonomy Technologies," *ION-GPS '99*, Proceedings of the 12th International Technical Meeting of the Satellite Division of the Institute of Navigation, Nashville, TN, Sept. 14-17, 1999 (A01-27218 06-32), Alexandria, VA, Institute of Navigation, 1999, p.369-383.
- [3] J. R. Carpenter, J. A. Leitner, D.C. Folta, and R.D. Burns, "Benchmark Problems For Spacecraft Formation Flying Missions," *AIAA Guidance, Navigation, and Control Conference*, August 2003, AIAA Paper 2003-5364.
- [4] A. Das, R. Cobb, "TechSat 21 - Space Missions Using Collaborating Constellations of Satellites," *Proceedings of AIAA/USU Annual Conference on Small Satellites*, 12th, Utah State University, Logan, Aug. 31-Sept. 3, 1998, Proceedings (A99-10826 01-20), Logan, UT, Utah State University, 1998.
- [5] C. Beichman, "The Terrestrial Planet Finder - The search for life-bearing planets around other stars," *Proceedings of Astronomical Interferometry Meeting*, Kona, HI, Mar. 20-24, 1998. Pt. 2 (A98-40801 11-35), Bellingham, WA, Society of Photo-Optical Instrumentation Engineers (SPIE Proceedings. Vol. 3350), 1998, p. 719-723.

- [6] F. Bauer, J. Bristow, D. Folta, K. Hartman, D. Quinn, J. How, "Satellite Formation Flying Using an Innovative Autonomous Control System (AutoCon) Environment," *Proceedings of AIAA Guidance, Navigation, and Control Conference*, New Orleans, LA, Aug. 11-13, 1997, Collection of Technical Papers. Pt. 2 (A97-37001 10-63), Reston, VA, American Institute of Aeronautics and Astronautics, 1997, p. 657-666.
- [7] M. Martin and M. Stallard, "Distributed Satellite Missions and Technologies-TheTechSat 21 Program," AIAA Paper 99-4479, Sept. 1999.
- [8] C. Sabol, et al, "Satellite Formation Flying Design and Evolution," *AIAA Journal of Spacecraft and Rockets*, v. 38, no. 2, Mar-Apr 2001.
- [9] J. Bristow, D. Folta, and K. Hartman. "A Formation Flying Technology Vision," *Proceedings of AIAA Space 2000 Conference and Exposition*, Long Beach, CA, Sept. 19-21, 2000. AIAA Paper 2000-5194.
- [10] E. Frazzoli. Quasi-random algorithms for real-time spacecraft motion planning and coordination. *Acta Astronautica*. 53(410):485495, 2003.
- [11] Air Force Research Laboratory Space Vehicles Directorate, "TechSat 21 factsheet page." <http://www.vs.afrl.af.mil/factsheets/TechSat21.html>.
- [12] J. P. How, R. Twigg, D. Weidow, K. Hartman, and F. Bauer, "Orion - A low-cost demonstration of formation flying in space using GPS," *Proceedings of AIAA/AAS Astrodynamics Specialist Conference and Exhibit*, Boston, MA, Aug. 10-12, 1998, Collection of Technical Papers (A98-37348 10-13), Reston, VA, American Institute of Aeronautics and Astronautics, 1998, p. 276-286.
- [13] J. Leitner, F. Bauer, D. Folta, M. Moreau, R. Carpenter, and J. P. How, "Distributed Spacecraft Systems Develop New GPS Capabilities," in *GPS World: Formation Flight in Space* Feb. 2002.
- [14] R. Sedwick, D. Miller, and E. Kong, "Mitigation of Differential Perturbations in Clusters of Formation Flying Satellites," *Proceedings of the AAS/AIAA Space*



- Flight Mechanics Meeting*, Breckenridge, CO, Feb. 7-10, 1999. Pt. 1 (A99-39751 10-12), San Diego, CA, Univelt, Inc. (Advances in the Astronautical Sciences. Vol. 102, pt.1), 1999, p. 323-342.
- [15] D. Vallado. *Fundamentals of Astrodynamics and Applications*. McGraw-Hill, 1997.
- [16] D. Lawden, *Optimal Trajectories for Space Navigation*, Butterworths, London, 1963.
- [17] T. Carter, M. Humi, "Fuel-Optimal Rendezvous Near a Point in General Keplerian Orbit," *AIAA Journal of Guidance, Control, and Dynamics*, vol. 10, Nov.-Dec. 1987, p. 567-573.
- [18] T. Carter, "New Form for the Optimal Rendezvous Equations Near a Keplerian Orbit," *AIAA Journal of Guidance, Control, and Dynamics*, vol. 13, Jan.- Feb. 1990, p. 183-186.
- [19] V. Kapila, A. G. Sparks, J. M. Buffington, and Q. Yan, "Spacecraft Formation Flying: Dynamics and Control," *2003 American Control Conference*, San Diego, CA, June 2-4, 1999, Institute of Electrical and Electronic Engineers, 1999, p. 4137-4141.
- [20] H. Schaub and K. T. Alfriend, "J2 Invariant Orbits for Spacecraft Formations," *Celestial Mechanics and Dynamical Astronomy*, Vol. 79, 2001, pp. 77-95.
- [21] P. Cefola, "A Recursive Formulation for the Tesseral Disturbing Function in Equinoctial Variables," *AIAA/AAS Astrodynamics Conference*, 1976, San Diego, CA, Aug. 18-20.
- [22] N. H. Smith, "*Automated Station-Keeping for Satellite Constellations*," S.M. Thesis, Massachusetts Institute of Technology, CSDL-T-1336, Cambridge, Massachusetts, June 1997.

- [23] J. E. Smith, “*Application of Optimization Techniques to the Design and Maintenance of Satellite Constellations*,” S.M. Thesis, Massachusetts Institute of Technology, CSDL-T-1336, Cambridge, Massachusetts, June 1999.
- [24] G. Inalhan, J. P. How, “Relative Dynamics and Control of Spacecraft Formations in Eccentric Orbits,” *Proceedings of the AIAA Guidance, Navigation, and Control Conference and Exhibit*, Denver, CO, Aug. 14-17, 2000, Collection of Technical Papers, Reston, VA, American Institute of Aeronautics and Astronautics, 2000. AIAA Paper 2000-4443.
- [25] M. Tillerson, J. P. How, “Formation Flying Control in Eccentric Orbits,” *Proceedings of the AIAA Guidance, Navigation, and Control Conference*, Montreal, Canada, Aug. 6-9, 2001, Collection of Technical Papers, Reston, VA, American Institute of Aeronautics and Astronautics, 2001.
- [26] M. Tillerson and J. P. How, “Advanced Guidance Algorithms for Spacecraft Formation Flying,” *Proceedings of the American Control Conference*, May 2002, pp. 2830-2835.
- [27] H. Yeh, A. Sparks, “Geometry and Control of Satellite Formations,” *Proceedings of the 2000 American Control Conference*, Chicago, IL, June 28-30, 2000. Vol. 1 (A01-12703 01-63), Piscataway, NJ, Institute of Electrical and Electronics Engineers, 2000, p. 384-388.
- [28] S. Vadali, S. Vaddi, K. Naik, K. T. Alfriend, “Control of Satellite Formations,” *Proceedings of the AIAA Guidance, Navigation, and Control Conference*, Montreal, Canada, Aug. 6-9, 2001. AIAA Paper 2001-4028.
- [29] A. Sparks, “Satellite Formationkeeping Control in the Presence of Gravity Perturbations,” *Proceedings of the 2000 American Control Conference*, Chicago, IL, June 28-30, 2000. Vol. 2 (A01-12740 01-63), Piscataway, NJ, Institute of Electrical and Electronics Engineers, 2000, p. 844-848.

- [30] A. Robertson, G. Inalhan, and J. P. How, "Formation Control Strategies for a Separated Spacecraft Interferometer," *Proceedings of the 1999 American Control Conference*, San Diego, CA, June 2-4, 1999, Proceedings. Vol. 6 (A00-15511 02-63), Piscataway, NJ, Institute of Electrical and Electronics Engineers, 1999, p. 4142-4147.
- [31] R. Bate, D. Mueller, and J. White, *Fundamentals of Astrodynamics*, Dover Publications Inc., NY, 1971.
- [32] V. Chobotov, *Orbital Mechanics*, Second Edition, AIAA Educational Series, 1996.
- [33] A. I. Solutions, "FreeFlyer User's Guide", Version 4.0, March 1999.
- [34] R. Sedwick, T. Hacker, and D. Miller, "Optimum Aperture Placement for a Space-Based Radar System Using Separated Spacecraft Interferometry," *Proceedings of the AIAA Guidance, Navigation, and Control Conference*, Portland, OR, Aug. 9-11, 1999. AIAA Paper 99-4271.
- [35] A. Richards, T. Schouwenaars, J. P. How, and E. Feron, "Spacecraft Trajectory Planning With Collision and Plume Avoidance Using Mixed Integer Linear Programming," submitted to the *AIAA Journal of Guidance, Control and Dynamics*, October, 2001.
- [36] F. Busse, G. Inalhan, and J. P. How, "Project ORION: Carrier Phase Differential GPS Navigation For Formation Flying," *Proceedings of the Annual AAS Rocky Mountain Conference*, Breckenridge, CO, Feb. 2-6, 2000 (A00-41276 11-12), San Diego, CA, Univelt, Inc. (Advances in the Astronautical Sciences. Vol. 104), 2000, p.197-212.
- [37] F. Busse, J. P. How, J. Simpson, and J. Leitner, "PROJECT ORION-EMERALD: Carrier Differential GPS Techniques and Simulation for Low Earth Orbit Formation Flying," presented at the *IEEE Aerospace Conference*, Mar 10-17, 2001.

- [38] A. Richards, J. P. How, T. Schouwenaars and E. Feron, "Plume Avoidance Manuever Planning Using Mixed Integer Linear Programming," *Proceedings of the AIAA Guidance, Navigation, and Control Conference*, Montreal, Canada, Aug. 6-9, 2001. AIAA Paper 2001-4091.
- [39] C. Park, P. Ferguson, N. Pohlman, and J. P. How, "Decentralized Relative Navigation for Formation Flying Spacecraft using Augmented CDGPS," *Proceedings of Institute of Navigation GPS Conference*, Salt Lake City, Utah, Sept. 2001.
- [40] M. Tillerson and J. P. How, "Advance Guidance Algorithms for Spacecraft Formation Flying," accepted for *2002 American Control Conference*, Anchorage, AK, May 8-10, 2002, Piscataway, NJ, Institute of Electrical and Electronics Engineers, 2002.
- [41] J. P. Vinti. *Orbital and Celestial Mechanics*. AIAA, 1998, pp.196-197.
- [42] R. G. Melton, Time Explicit Representation of Relative Motion Between Elliptical Orbits, *JGCD* Vol. 23, No. 4, July - Aug. 2000, pp. 604-610.
- [43] M. Tillerson, L. S. Breger, and J. P. How, "Distributed Coordination and Control of Formation Flying Spacecraft," *Proceedings of American Control Conference*, June 2003.
- [44] D. T. Greenwood, *Advanced Dynamics*, Cambridge University Press, Cambridge, 2003.
- [45] K. T. Alfriend, H. Schaub, and D.-W. Gim, "Formation Flying: Accomodating Non-linearity and Eccentricity Perturbations," presented at the 12th *AAS/AIAA Space Flight Mechanics Meeting*, January 27-30, 2002.
- [46] J. Guzman and C. Schiff, "A Preliminary Study for a Tetrahedron Formation (Spacecraft Formation Flying)," *AIAA/AAS Astro. Specialists Conf.*, Aug 2002.
- [47] P. Robert, A. Roux, C. Harvey, M. Dunlop, P. Daly, and K. Glassmeier, "Tetrahedron Geometric Factors," *Analysis Methods for Multi-Spacecraft Data (G.*

- Paschmann and P. Daly, eds.), pp. 323348, Noordwijk, The Netherlands: ISSI Report SR-001, ESA Pub. Div., 1998.
- [48] F. D. Busse and J. P. How, "Real-Time Experimental Demonstration of Precise Decentralized Relative Navigation for Formation-Flying Spacecraft," *AIAA Guidance, Navigation, and Control Conference*, August 2002, AIAA Paper 2002-5003
- [49] A. Robertson, G. Inalhan, and J.P. How, "Spacecraft Formation Flying Control Design for the Orion Mission," in *Proceedings of AIAA/GNC*, August 1999.
- [50] A. G. Richards and J. P. How, "Model Predictive Control of Vehicles Maneuvers with Guaranteed Completion Time and Robust Feasibility," American Control Conference, Denver CO, ACC, 2003.
- [51] A. G. Richards and J. P. How, "Robust Constrained Model Predictive Control with Analytical Performance Prediction," *AIAA Guidance, Navigation, and Control Conference*, August 2004.
- [52] L. S. Breger, A. G. Richards, M. Mitchell, and J. P. How, "Model Predictive Control of Spacecraft Formations with Sensing Noise," *AIAA Guidance, Navigation, and Control Conference*, August 2004.
- [53] M. Tillerson, "Coordination and Control of Multiple Spacecraft using Convex Optimization Techniques," S.M. Thesis, Massachusetts Institute of Technology, Dept. Aeronautics and Astronautics, June 2002.
- [54] D. J. Zimpfer, P. S. Spehar, F. Clark, C. D' Souza, and M. Jackson, "Autonomous rendezvous and capture guidance, navigation and control," *Flight Mechanics Symposium*, (Goddard Space Flight Center, Greenbelt, Maryland), Session 3, Paper 7, October 18-20, 2005.
- [55] M. E. Polites, "Technology of Automated Rendezvous and Capture in Space," *AIAA Journal of Spacecraft and Rockets*, vol. 36, no. 2, March-April 1999, p. 280-291.

- [56] I. Kawano, M. Mokuno, T. Kasai, T. Suzuki, "Result and evaluation of autonomous rendezvous docking experiments of ETS-VII," Proceedings of the AIAA Guidance, Navigation and Control Conference, Aug 1999. AIAA-1999-4073.
- [57] T. E. Rumford, "Demonstration of Autonomous Rendezvous Technology (DART) Project Summary," *Proceedings of SPIE*, Volume 5088, pp.10–19, 2003.
- [58] K. Young, "Autonomous rendezvous in space becomes hit and run," *New Scientist Space*, online at <http://www.newscientistspace.com/article/dn7303>, last accessed Jan. 2006.
- [59] B. Berger, "Fender Bender: NASA's DART Spacecraft Bumped Into Target Satellite," *Space.com*, online at <http://www.space.com/missionlaunches/050422.dart.update.html>, last accessed Jan. 2006.
- [60] "Overview of the DART Mishap Investigation Results," *NASA.gov*, online at [http://www.nasa.gov/mission\\_pages/dart/main/index.html](http://www.nasa.gov/mission_pages/dart/main/index.html), last accessed May 2006.
- [61] A. G. Richards, T. Schouwenaars, J. P. How, and E. Feron, "Spacecraft Trajectory Planning With Collision and Plume Avoidance Using Mixed Integer Linear Programming," *AIAA Journal of Guidance, Control and Dynamics*, vol. 25, pp.755-764, Aug 2002.
- [62] I. Garcia and J. P. How, "Trajectory Optimization for Satellite Reconfiguration Maneuvers with Position and Attitude Constraints" *Proceedings of the IEEE American Control Conference*, June 2005, pp.889-895
- [63] P. K. C. Wang, M. Mokuno, and F. Y. Hadaegh, "Formation Flying of Multiple Spacecraft with Automatic Rendezvous and Docking Capability," AIAA Guidance, Navigation, and Control Conference, Austin, TX, Aug 11-14, 2003.

- [64] D. Scharf, S. Ploen, and F. Hadaegh, "A Survey of Spacecraft Formation Flying Guidance and Control (Part I): Guidance," *IEEE American Control Conference*, June 2003.
- [65] D. Scharf, F. Hadaegh, and S. Ploen, "A Survey of Spacecraft Formation Flying Guidance and Control (Part II): Control," *IEEE American Control Conference*, June 2004, 2976–2985.
- [66] X. Duan and P. M. Bainum, "Design of Spacecraft Formation Flying Orbits," American Astronautical Society, AAS 03-588, August 2003.
- [67] W. Fehse. *Automated Rendezvous and Docking of Spacecraft*. Cambridge University Press, 2003.
- [68] B. Naasz, "Safety Ellipse Motion with Coarse Sun Angle Optimization," *Flight Mechanics Symposium*, (Goddard Space Flight Center, Greenbelt, Maryland), 2005.
- [69] S. Jacobsen, C. Lee, C. Zhu, and S. Dubowsky "Planning of safe kinematic trajectories for free flying robots approaching an uncontrolled spinning satellite," DETC2002/MECH, Montreal, Canada, 2002.
- [70] S. Matsumoto, S. Dubowsky, S. Jacobsen, and Y. Ohkami, "Fly-by Approach and Guidance for Uncontrolled Rotating Satellite Capture," AIAA Guidance, Navigation, and Control Conference, Austin, TX, Aug 11-14, 2003.
- [71] T. Schouwenaars, J. P. How, and E. Feron, "Decentralized Cooperative Trajectory Planning of Multiple Aircraft with Hard Safety Guarantees," Proceedings of the AIAA Guidance, Navigation and Control Conference, Aug 2004. AIAA-2004-5141.
- [72] C. Tomlin, I. Mitchell, R. Ghosh, "Safety Verification of Conflict Resolution Maneuvers," *IEEE Transactions on Intelligent Transportation Systems*, vol 2., no 2., June 2001, p.110.

- [73] M. Tillerson and J. P. How, "Analysis of the Impact of Sensor Noise on Formation Flying Control," *Proceedings of the 2001 American Control Conference*, Arlington, VA, June 25-27, 2001.
- [74] L. S. Breger and J. P. How, " $J_2$ -Modified GVE-Based MPC for Formation Flying Space," *AIAA GNC Conf.*, August 2005.
- [75] G. W. Hill, "Researches in Lunar Theory," *American Journal of Mathematics*, Vol. 1, 1878, pp. 5–26, 129–147, 24–260.
- [76] W. H. Clohessy and P. S. Wiltshire, "Terminal Guidance System for Satellite Rendezvous," *Journal of Aerospace Sciences*, Sept. 1960, pp. 653–658, 674.
- [77] A. G. Richards, "Robust Constrained Model Predictive Control," PhD Thesis, Massachusetts Institute of Technology, November 2004.
- [78] S. Nolet, "Development of a guidance, navigation and control architecture for autonomous docking to a target under generalized motion," PhD Thesis, Massachusetts Institute of Technology, June 2006.
- [79] A. B. Roger and C. R. McInnes, "Safety constrained freeflyer path planning at the international space station," *Journal of Guidance, Control, and Dynamics*, 23(6):971979, NovemberDecember 2000.
- [80] D. T. Greenwood, *Advanced Dynamics*, Cambridge University Press, Cambridge, 2003.
- [81] J. P. How, R. Twigg, D. Weidow, K. Hartman, and F. Bauer, "Orion - A low-cost demonstration of formation flying in space using GPS," *Proceedings of AIAA/AAS Astrodynamics Specialist Conference and Exhibit*, Boston, MA, Aug. 10-12, 1998, Collection of Technical Papers (A98-37348 10-13), Reston, VA, American Institute of Aeronautics and Astronautics, 1998, p. 276-286.
- [82] Y. Kuwata, *Real-time Trajectory Design for Unmanned Aerial Vehicles using Receding Horizon Control*, S.M. Thesis, Dept. of Aeronautics and Astronautics, MIT, Jun. 2003.



- [83] G. Strang. *Introduction to Applied Mathematics*. Wellesley-Cambridge Press, 1986.
- [84] M. Tillerson, G. Inalhan, and J. P. How, "Coordination and Control of Distributed Spacecraft Systems Using Convex Optimization Techniques," *International Journal of Robust and Nonlinear Control*, vol 12, Issue 2-3, Feb.-Mar. 2002, p.207-242.
- [85] K. T. Alfriend, H. Schaub, and D.-W. Gim, "Formation Flying: Accomodating Non-linearity and Eccentricity Perturbations," presented at the 12th *AAS/AIAA Space Flight Mechanics Meeting*, January 27-30, 2002.
- [86] S. Curtis, "The Magnetospheric Multiscale Mission Resolving Fundamental Processes in Space Plasmas," NASA GSFC, Greenbelt, MD, Dec. 1999. NASA/TM2000-209883.
- [87] L. S. Breger, *Model Predictive Control for Formation Flying Spacecraft*, S.M. Thesis, Massachusetts Institute of Technology, Dept. Aeronautics and Astronautics, June 2004.
- [88] S. Gaulocher, J. P. Chrétien, C. Pittet, M. Delpech, and D. Alazard, "Closed-Loop Control of Formation Flying Satellites: Time and Parameter Varying Framework," "2nd International Symposium on Formation Flying Missions & Technologies, Washington, DC, September 14-16, 2004.
- [89] J. Junkins, M. Akella, K. T. Alfriend, "Non-Gaussian Error Propagation in Orbital Mechanics," in *The Journal of the Astronautical Sciences*, Vol. 44, No. 4, 1996.
- [90] M. R. Ilgen, "Low Thrust OTV Guidance using Lyapunov Optimal Feedback Control Techniques," *AAS/AIAA Astrodynamics Specialist Conference*, Victoria, B.C., Canada, Aug. 16-19 1993, Paper No. AAS 93-680.
- [91] B. Naasz, *Classical Element Feedback Control for Spacecraft Orbital Maneuvers*,

- S.M. Thesis, Dept. of Aerospace Engineering, Virginia Polytechnic Institute and State University, May 2002.
- [92] P. Gurfil, "Control-Theoretic Analysis of Low-Thrust Orbital Transfer Using Orbital Elements," *AIAA Journal of Guidance, Control, and Dynamics*, vol. 26, no. 6, November-December 2003, p. 979-983.
- [93] H. Schaub and K. T. Alfriend, "Impulsive Feedback Control to Establish Specific Mean Orbit Elements of Spacecraft Formations," *AIAA Journal of Guidance, Control, and Dynamics*, vol. 24, no. 4, July-Aug. 2001, p. 739-745.
- [94] D. Mishne "Formation Control of LEO Satellites Subject to Drag Variations and  $J_2$  Perturbations," *AAS/AIAA Astrodynamics Specialist Conference*, Monterey, California, August 2002.
- [95] J. M. Maciejowski, *Predictive Control with Constraints*, Prentice Hall, England, 2002.
- [96] L. S. Breger and J. P. How, "GVE-Based Dynamics and Control for Formation Flying Spacecraft," presented at the *2nd International Formation Flying Symposium*, Sept. 2004.
- [97] M. Tillerson, L. S. Breger, and J. P. How, "Distributed Coordination and Control of Formation Flying Spacecraft," *Proceedings of American Control Conference*, June 2003.
- [98] D. W. Gim and K. T. Alfriend, "State Transition Matrix of Relative Motion for the Perturbed Noncircular Reference Orbit," *AIAA Journal of Guidance, Control, and Dynamics*, vol. 26, no. 6, Nov.-Dec. 2003, p. 956-971.
- [99] R. H. Battin, An Introduction to the Mathematics and Methods of Astrodynamics, AIAA Education Series, New York, 1987.
- [100] H. Schaub and J. L. Junkins, Analytical Mechanics of Space Systems, AIAA Education Series, Reston, VA, 2003.

- [101] L. S. Breger, P. Ferguson, J. P. How, S. Thomas, T. McLoughlin, and M. Campbell, "Distributed Control of Form. Flying Spacecraft Built on OA," *AIAA GNC Conf.*, August 2003.
- [102] G. Franklin, J. Powell, and M. Workman, Digital Control of Dynamic Systems, Third Edition, Addison-Wesley, 1998.
- [103] J. R. Carpenter and K. T. Alfriend, "Navigation Accuracy Guidelines for Orbital Formation Flying," AIAA Guidance, Navigation, and Control Conference, Austin, TX, Aug 11-14, 2003.
- [104] W. Ren and R. Beard, "Virtual Structure Based Spacecraft Formation Control with Formation Feedback," presented at the *AIAA GN&C Conference*, Aug. 2002.
- [105] F. Busse, J. P. How, J. Simpson, and J. Leitner, "PROJECT ORION-EMERALD: Carrier Differential GPS Techniques and Simulation for Low Earth Orbit Formation Flying," presented at the *IEEE Aerospace Conference*, Mar 10-17, 2001.
- [106] M. Kaplan. Modern Spacecraft Dynamics and Control. Wiley, 1976.
- [107] T. E. Carter and S. A. Alvarez, "Quadratic-Based Computation of Four-Impulse Optimal Rendezvous near Circular Orbit," *AIAA Journal of Guidance, Control, and Dynamics*, vol. 23, no. 1, January-February 2000, p. 109-117.
- [108] L. Mailhe, C. Schiff, and S. Hughes, "Formation Flying in Highly Elliptical Orbits: Initializing the Formation," *Proceedings of the International Symposium on Space Dynamics*, Biarritz, France, CNES, June 26-30, 2000. Paper MS00/21.
- [109] G. Inalhan, M. Tillerson, and J. P. How, "Relative Dynamics & Control of Spacecraft Formations in Eccentric Orbits," *AIAA Journal of Guidance, Control, and Dynamics* (0731-5090), vol. 25, no. 1, Jan.-Feb. 2002, p. 48-59.

- [110] S. R. Vadali, K. T. Alfriend, and S. Vaddi, "Hills Equations, Mean Orbital Elements, and Formation Flying of Satellites," American Astronautical Society, AAS 00-258, March 2000.
- [111] D. Bertsimas and J. N. Tsitsiklas, *Introduction to Linear Optimization*, Athena Scientific, Belmont, 1997.
- [112] A. I. Solutions, "FreeFlyer User's Guide", Version 4.0, March 1999.
- [113] Mitsubishi Electric Corporation internal document. Spacecraft Parameters for "Research on GNC Architecture for Future Spacecraft Formation Flight," February 19, 2005.
- [114] D. K. Geller, "Linear Covariance Techniques for Orbital Rendezvous Analysis and Autonomous Onboard Mission Planning," *Journal of Guidance, Control, and Dynamics*, 29(6):1404-1414, November/December 2006.
- [115] L. S. Breger, G. Inalhan, M. Tillerson, and J. P. How, "Cooperative Spacecraft Formation Flying: Model Predictive Control With Open- And Closed-Loop Robustness," *Modern Astrodynamics*, edited by P. Gurfil, Elsevier, Oxford, 2006.
- [116] S. Schweighart, *Development and Analysis of a High Fidelity Linearized J2 Model for Satellite Formation Flying*, S.M. Thesis, Massachusetts Institute of Technology, Dept. Aeronautics and Astronautics, June 2001.
- [117] C. D. Karlgrad and F. H. Lutze, "Second Order Relative Motion Equations," *Advances in the Astronautical Sciences*, Vol. 109, Pt. 3, 202, p. 2429-2448.
- [118] J. W. Mitchell and D. L. Richardson., "A Third Order Analytic Solution for Relative Motion with a Circular Reference Orbit", *Journal of the Astronautical Sciences*, Vol. 51, No. 1, 2003, p. 1-12.
- [119] K. T. Alfriend and H. Yan, "Evaluation and Comparison of Relative Motion Theories," *Journal of Guidance, Control and Dynamics*, Vol. 28, No. 2, 2005, p.254-261.

- [120] L. S. Breger and J. P. How, "Gauss's Variational Equation-Based Dynamics and Control for Formation Flying Spacecraft," *AIAA Journal of Guidance, Control and Dynamics*, accepted for publication April 18, 2006.
- [121] A. G. Richards, L. S. Breger, and J. P. How, "Analytical Performance Prediction for Robust Constrained Model Predictive Control," *International Journal of Control*, Vol. 79, No. 6, August 2006, pp. 877-894.